

**The Search for Higgs Boson Production in Association  
with a Top-Quark Pair in  $pp$  Collisions at  $\sqrt{s} = 8$  TeV in  
the Lepton Plus Jets Final State**

John Garland Wood  
Charlottesville, VA

B.S., The University of California, Berkeley, 2008

A Dissertation presented to the Graduate Faculty  
of the University of Virginia in Candidacy for the Degree of  
Doctor of Philosophy

Department of Physics

University of Virginia  
May, 2015

## Abstract

The most important goal of the Large Hadron Collider (LHC) is to elucidate the mechanism of electroweak symmetry breaking. The Standard Model (SM) Higgs boson is thought to be a prime candidate for this. The newly discovered boson announced on July 4th, 2012, with a mass of  $\sim 125$  GeV/c $^2$ , has so far been shown to be consistent with a SM Higgs. However, the final confirmation of this new particle as the SM Higgs depends on subsequent measurements of all of its properties. The observation of this new particle in association with top-quark pairs would allow the couplings of this particle to top and bottom quarks to be directly measured.  $t\bar{t}H$ , with Higgs decaying to  $b\bar{b}$  is an excellent channel to explore due to the dominant branching ratio of Higgs to  $b\bar{b}$  and the kinematic handle the  $t\bar{t}$  system offers on the event. However, it presents a plethora of difficult challenges due to a low signal to background ratio and uncertainties on kinematically similar SM backgrounds. This work discusses the search for Higgs boson production in association with a top-quark pair in  $pp$  collisions at  $\sqrt{s} = 8$  TeV, collected by the Compact Muon Solenoid (CMS) experiment at the LHC. The search has been performed and published in two stages. The first analysis used the first 5.1 fb $^{-1}$ , and was followed up by the second analysis with the full 2012 dataset, using a total integrated luminosity of 19.5 fb $^{-1}$

We approve the dissertation of John Garland Wood.

Date of Signature

---

Supervisor: Dr. Christopher Neu

---

Committee Chair: Dr. Bradley Cox

---

Committee Member: Dr. Hank Thacker

---

PhD Committee Chair: Dr. Astronomy Person

# Contents

<b>Contents</b>	<b>iv</b>
<b>List of Figures</b>	<b>vi</b>
<b>List of Tables</b>	<b>x</b>
<b>1 Introduction</b>	<b>1</b>
<b>2 Theoretical Background</b>	<b>4</b>
2.1 An Overview of Quantum Field Theory . . . . .	4
2.2 Abelian Gauge Theories of Particle Interactions . . . . .	7
2.3 Non-Abelian Gauge Theories of Particle Interactions . . . . .	9
2.4 The Higgs Mechanism in an Abelian Theory . . . . .	12
2.5 The Higgs Mechanism in a non-Abelian Theory . . . . .	14
2.6 Glashow Weinberg Salam Theory . . . . .	16
2.7 The Standard Model of Particle Physics . . . . .	22
2.8 Higgs Production in $pp$ Collisions at the LHC . . . . .	24
2.9 $t\bar{t}H$ Production in $pp$ Collisions at the LHC . . . . .	26
2.10 Background Processes to $t\bar{t}H$ . . . . .	27
2.11 Potential BSM Effects on $t\bar{t}H$ production . . . . .	30
<b>3 The Large Hadron Collider</b>	<b>32</b>
3.1 The LHC Accelerator Complex . . . . .	34
3.2 LHC Magnets . . . . .	42
3.3 LHC RF Technology . . . . .	48
3.4 The LHC Cryogen System . . . . .	51
3.5 The LHC Vacuum System . . . . .	52
<b>4 The Compact Muon Solenoid</b>	<b>54</b>
4.1 The Tracker . . . . .	56

4.1.1	The Silicon Pixel Detector . . . . .	58
4.1.2	The Silicon Strip Detector . . . . .	60
4.2	The Electromagnetic Calorimeter . . . . .	63
4.2.1	Vacuum Photo-Triodes . . . . .	67
4.2.2	Test Rig at UVa . . . . .	68
4.2.3	Results of UVa Tests . . . . .	69
4.3	The Hadronic Calorimeter . . . . .	72
4.4	Muon Chambers . . . . .	77
4.5	Data Collection Overview . . . . .	81
<b>5</b>	<b>Particle Reconstruction at CMS</b>	<b>85</b>
5.1	Muon Reconstruction . . . . .	85
5.2	Electron Reconstruction . . . . .	85
5.3	Photon Reconstruction . . . . .	85
5.4	Jet Reconstruction . . . . .	85
5.5	Tau Reconstruction . . . . .	86
5.6	Missing Transverse Energy Reconstruction . . . . .	86
<b>Bibliography</b>		<b>87</b>
<b>List of Acronyms</b>		<b>93</b>

# List of Figures

1.1	The CMS experiment has observed a new boson at $m \sim 125 \text{ GeV}/c^2$ . . . . .	1
1.2	A Feynman diagram of the $t\bar{t}H$ process, with $\text{Higgs} \rightarrow b\bar{b}$ , and the $t\bar{t}$ -system decaying semi-leptonically . . . . .	3
2.1	Leading and Next to Leading Order Feynman diagrams for the coulomb scattering process . . . . .	6
2.2	The global average of $\alpha_s$ , the QCD coupling constant. . . . .	7
2.3	A visual representation of the Higgs potential . . . . .	12
2.4	Experimental milestones of the Standard Model . . . . .	23
2.5	Higgs production cross-sections at the LHC, for 7-14 TeV $pp$ collisions . . . . .	24
2.6	Feynman diagrams for the three largest Higgs production modes at the LHC . .	25
2.7	Feynman diagram for $t\bar{t}H$ production . . . . .	26
2.8	Feynman diagrams for the semileptonic $t\bar{t}H$ process and its irreducible background, $t\bar{t} + b\bar{b}$ . . . . .	27
2.9	Feynman diagrams for the $t\bar{t}W$ and $t\bar{t}Z$ background processes . . . . .	28
2.10	Feynman diagrams for the single $t$ , $s,t$ , and $tW$ background processes . . . . .	28
2.11	Feynman diagrams for the $W, Z$ plus jets, and diBoson ( $WW, WZ, ZZ$ ) production. .	29
2.12	Measurements of $t\bar{t}H$ backgrounds at CMS . . . . .	29
2.13	The cancellation of the divergent Higgs mass from a loop of top-quarks is cancelled by a loop of supersymmetric top-quarks, stop-quarks, . . . . .	31
3.1	Aerial view of the LHC complex, spanning the French-Swiss border [1] . . . . .	32
3.2	Integrated Luminosity delived to the CMS experiment from 2010-12 . . . . .	34
3.3	The LHC accelerator complex, taking protons from a bottle of Hydrogen at the Linac2, all the way to the LHC ring . . . . .	35
3.4	Features of the Linac2, the first stage of acceleration in the LHC injection chain .	36
3.5	Features of the PS booster, the second stage of the LHC injection chain . . . . .	37
3.6	Features of the PS, the third stage of the LHC injection chain . . . . .	40

3.7	Features of the SPS, the fourth and final stage of the LHC injection chain . . . . .	41
3.8	The LHC ring is divided into eight octants . . . . .	43
3.9	The single turn injection scheme. A septum magnet makes the initial alignment. The kicker magnet times the injection and makes the final alignment. Bumper magnets align the LHC beam with the injected beam. . . . .	44
3.10	Layout of Interaction Region 8, where one proton beam is injected into the LHC ring. A transfer line from the SPS bring a proton in from the right. In green, a septum magnet aligns the beam horizontally with the LHC. In blue, a kicker magnet makes the final vertical alignment into the LHC, and is timed to fill one of the 400 MHz buckets of the RF capture system . . . . .	44
3.11	The initial filling of 6 batches of protons from the PSB to the PS, leaves 12 empty buckets in the PS bunch structure. The rise time of the SPS magnet creates an additonal gap in the SPS bunch structure. Additional gaps emerge due to the rise time of the LHC injection and dumping kicker magnets . . . . .	45
3.12	Features of the dipole magnets used in the LHC . . . . .	46
3.13	Features of the dipole magnets used in the LHC . . . . .	47
3.14	Features of the 400 MHz superconducting RF system used in the LHC . . . . .	48
3.15	A klystron uses a weak RF signal coupled to a resonace cavity to bunch an electron beam, which in turn creates an amplified RF signal as it passes through a second resonance cavity tuned to the same frequency. . . . .	49
3.16	One of sixteen 300 kW, 400 MHz klystrons that power the superconducting RF cavities that accelerate the proton beam. . . . .	50
3.17	Layout of the five cryogenic islands, which are home to the eight facilities that provide liquid helium to the LHC . . . . .	51
3.18	Features of the 4.5 K refridgeration system . . . . .	51
3.19	Cross section schematic of the cryogenic distribution system in the LHC tunnel .	52
3.20	Beam screen for the LHC, with slits to allow for easy pumping of residual gas molecules in the beampipe. . . . .	53
4.1	A cutaway diagram of the CMS detector. Two humans are present at the bottom of the image to provide scale. . . . .	54
4.2	A slice of the CMS detector showing how various particles interact and deposit energy. The trajectory of charged particles is measured in the tracker; electrons and photons deposit most of their energy in the ECAL; charged and neutral hadrons deposit most of their energy in the HCAL; the muon chambers measures the trajectory of muons or long-lived charged particles . . . . .	55

4.3 A side view of the tracker. The pixel detector is the innermost sub-system, with three concentric rings of detectors in the barrel, and two in the endcap. The tracker inner barrel (TIB) is a silicon strip detector, with four concentrinc rings. The tracker inner disks (TID) are three layers deep. The tracker outer barrel (TOB) is six concentric rings and the tracker end caps (TEC) are nine layers deep.	57
4.4 A head-on view of the beamline and barrel components of the tracker. . . . .	57
4.5 The three barrel and two disk layers of the silicon pixel tracker provide coverage of $ \eta  < 2.5$ . . . . .	58
4.6 The readout electronics chain for the pixel detector . . . . .	59
4.7 In 2012 $pp$ collisions at $\sqrt{s} = 8 \text{ TeV}$ , the pixel detector performed wiht a resolution of $11.8 \mu\text{m}$ . The above is a plot of the residual difference between a pixel and the results of a fit to a particle track. . . . .	60
4.8 A silicon strip module, with two $500 \mu\text{m}$ thick sensors. . . . .	61
4.9 Schematic of the readout sequence of the silicon strip detector. . . . .	62
4.10 Measurements of the performance of the silicon strip track using $pp$ collisions from 2011 at $\sqrt{s} = 7 \text{ TeV}$ . . . . .	62
4.11 Layout of the ECAL sub-detector . . . . .	63
4.12 Typical Lead Tungstate crystal, with APD attached to the rear face in the left frame, and a VPT attached in the right frame. . . . .	63
4.13 A simulation of the evolution of a electromagnetic shower being initiated by an electron entering the center of the front face. . . . .	64
4.14 A module of 500 crystals (25 crtials wide by 20 crystal tall). . . . .	65
4.15 Schematic of the On-Detector Readout for the ECAL . . . . .	66
4.16 A section of the ECAL end-cap, a Dee. Two Dees form a disk with an inner bore for the beam-line to pass through. 5x5 modules, or supercrystals, are mounted in preparation for installation at CMS . . . . .	67
4.17 Vacuum Photo-Triode devices used in the ECAL end-caps (EE) . . . . .	67
4.18 Features of the UVa VPT test stand . . . . .	70
4.19 3 runs of 5 VPTs, exposed to blue LED light, and fit to a sum of two exponentials. . . . .	71
4.20 3 runs of 5 VPTs, exposed to orange LED light, and fit to a sum of two exponentials. . . . .	72
4.21 Longitudinal cross-section of the HCAL with the four sub-systems labeled . . . . .	73

4.22 Closeup of the HCAL barrel section. The center section of each of the 18 wedges are labeled, optical cables lay accross the joint of the center and staggered edge sections of each wedge. The blue lines show the apporximate azimuthal division of the wedge. . . . .	74
4.23 Over 1 million Russian shells of military artillery were re-processed in the construction of the HCAL . . . . .	75
4.24 Optical readout chain of the HCAL scintillator tiles . . . . .	75
4.25 HCAL endcap, 18 azimuthal divisions of alternating layers of brass and plastic scintillator. . . . .	76
4.26 Longitudinal cross-section of the HCAL forward calorimetry, the HF . . . . .	76
4.27 Longitudinal cross-section of one of the 5 wheels of the muon system. Drift tubes are placed in 4 concentric layers, with 2 being placed inside the return yoke of the magnet, and 12 azimuthal divisions. . . . .	78
4.28 A cross-section view of a drift cell. The anode wire is held at 3600 V, creating a potential difference with the walls. Electric field lines are shown in blue. . . . .	79
4.29 RPC layout for the barrel and endcaps . . . . .	79
4.30 Exploded diagram of an RPC . . . . .	80
4.31 Cross-section of one quarter of the muon endcap system, with the 4 disks of CSC systems shown in red . . . . .	80
4.32 A CSC station with 7 layers, making 6 gas chambers. Cathode strips are shown in yellow, perpendicular to the vertical anode wires in orange. . . . .	81
4.33 A block diagram of the L1 trigger . . . . .	82
4.34 A schematic of the $e/\gamma$ trigger algorithm . . . . .	82
4.35 Layout of the CMS DAQ . . . . .	83

# List of Tables

2.1	The quantum numbers Isospin and Hypercharge are assigned for each of the $SU(2)$ and $U(1)$ symmetries respectively . . . . .	20
4.1	Fit Results for VPT Conditioning Studies at U.Va. and Brunel, Blue Reference LED . . . . .	71
4.2	Fit Results for VPT Conditioning Studies at U.Va., Orange LED . . . . .	72

# <sup>1</sup> Chapter 1

## <sup>2</sup> Introduction

<sup>3</sup> On July 4th, 2012, the Compact Muon Solenoid (CMS) and A Toroidal LHC Apparatus (ATLAS)  
<sup>4</sup> experiments announced the discovery of a new boson of mass  $\sim 125 \text{ GeV}/c^2$  [2] [3]. The particle  
<sup>5</sup> has been shown to be increasingly consistent with the description of the boson predicted by the  
<sup>6</sup> Higgs mechanism of the SM, as measurements on its mass, width, and quantum numbers are  
<sup>7</sup> completed. However, there are several properties of this new boson, which remain to be tested.  
<sup>8</sup> Figure 1.1 shows a consistent mass peak between the  $H \rightarrow ZZ$  and  $H \rightarrow \gamma\gamma$  channels at the  
<sup>9</sup> CMS experiment.

<sup>10</sup> The Yukawa coupling of the Higgs boson to the top-quark in the SM is the largest coupling  
<sup>11</sup> among the fundamental particles and is well predicted - thus offering an excellent test of the  
<sup>12</sup> nature of the coupling of the Higgs to fermions, as well as a potential probe into physics Beyond  
<sup>13</sup> the Standard Model (BSM) that would alter this value from the SM prediction. The production  
<sup>14</sup> of the Higgs boson in association with top-quark pairs is the best production mode at the LHC  
<sup>15</sup> that offers direct access to the top-Higgs coupling. The dominant production mode of Higgs  
<sup>16</sup> at the LHC, gluon-gluon fusion, involves a triangle loop of strongly-coupled fermions, which

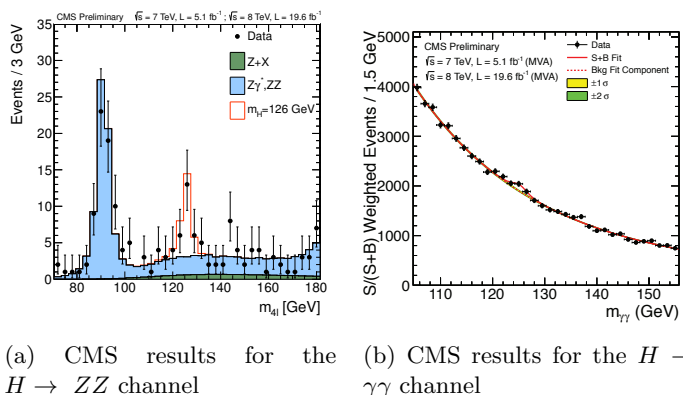


Figure 1.1: The CMS experiment has observed a new boson at  $m \sim 125 \text{ GeV}/c^2$

<sup>17</sup> includes all of the other quarks, as well as the potential for BSM particles.

<sup>18</sup>       $t\bar{t}H$  production also has the ability to constrain some extensions of the SM that would not  
<sup>19</sup> modify the Higgs branching fractions enough to be seen within current experimental precision.  
<sup>20</sup> Such models include Little Higgs models, models with extra dimensions, top-color models, and  
<sup>21</sup> composite Higgs models that introduce a vector-like top partner, a  $t'$ , that can decay to  $tH$ ,  
<sup>22</sup>  $bW$ , or  $tZ$  states. Both  $t't'$  and  $t't$  production would produce a  $t\bar{t}H$  final state, or one that is  
<sup>23</sup> indistinguishable from it ( $tHbW$ ). Upper limits on  $t\bar{t}H$  production would also provide limits on  
<sup>24</sup> the previously described models, which would be complementary to existing direct searches for  
<sup>25</sup>  $t'$  particles, which attempt to reconstruct the  $t'$  resonance.

<sup>26</sup>      The  $t\bar{t}H$  channel has a rich set of possible final states. Each top-quark will decay to a  $b$ -  
<sup>27</sup> quark and a  $W$  boson. The  $W$  boson will subsequently decay to two quarks, or a lepton and a  
<sup>28</sup> neutrino. These decays are classified as either hadronic, semi-leptonic, or di-leptonic for zero,  
<sup>29</sup> one, or both  $t$  quarks decaying leptonically respectively. The Higgs may decay to  $b$ -quark,  $W$ ,  
<sup>30</sup>  $Z$ ,  $\tau$ , or  $\gamma$  pairs. In fact, this is one of the only production modes at the LHC which has access  
<sup>31</sup> to every Higgs decay mode, as other production mechanisms are swamped by large backgrounds  
<sup>32</sup> preventing measurements of all Higgs decay types.

<sup>33</sup>      The search is performed with the CMS experiment, a modern, general purpose particle  
<sup>34</sup> detector capable of reconstructing and identifying hadronic jets, photons, electrons, muons,  
<sup>35</sup> and tau leptons. The hermetic design, and its high precision and efficiency in reconstructing  
<sup>36</sup> and tracking every particle in a  $pp$  collision, also makes it suitable for reconstructing missing  
<sup>37</sup> transverse energy from the calculated momentum imbalance of all of the measured particles in  
<sup>38</sup> the event. This missing transverse energy is often the signature of a neutrino, which is the  
<sup>39</sup> only SM particle capable of escaping detection. The detector uses a 3.8 T axial magnetic field,  
<sup>40</sup> produced by the solenoid it is named after, to bend charged particles as they travel through  
<sup>41</sup> the detector. The measured curvature of their tracks allows the momentum of the particles to  
<sup>42</sup> be calculated with to a high precision. Tracks are formed and particles are reconstructed by a  
<sup>43</sup> combination of sub-detector systems which work together to form the final reconstructed  
<sup>44</sup> image of each particle in the collision.

<sup>45</sup>      This thesis will focus on a semi-leptonic decay of the top-quarks, with the Higgs decaying to  
<sup>46</sup> a  $b$ -quark pair. Figure 1.2 is Feynman diagram of the  $t\bar{t}H$  process. The largest background to  
<sup>47</sup> this process is top-quark pair production with extra jets originating from Initial State Radiation  
<sup>48</sup> (ISR) or Final State Radiation (FSR) radiation,  $t\bar{t} + jets$ . The irreducible background is formed  
<sup>49</sup> by top-quark pairs, where a gluon is radiated and decays to  $b$ -quark pairs,  $t\bar{t} + b\bar{b}$ . In addition  
<sup>50</sup> to the large backgrounds, the high jet multiplicity in the  $t\bar{t}H$  final state gives rise to a combina-  
<sup>51</sup> torics problem in associating each jet with its role in the  $t\bar{t}H$  system. This inevitably leads to

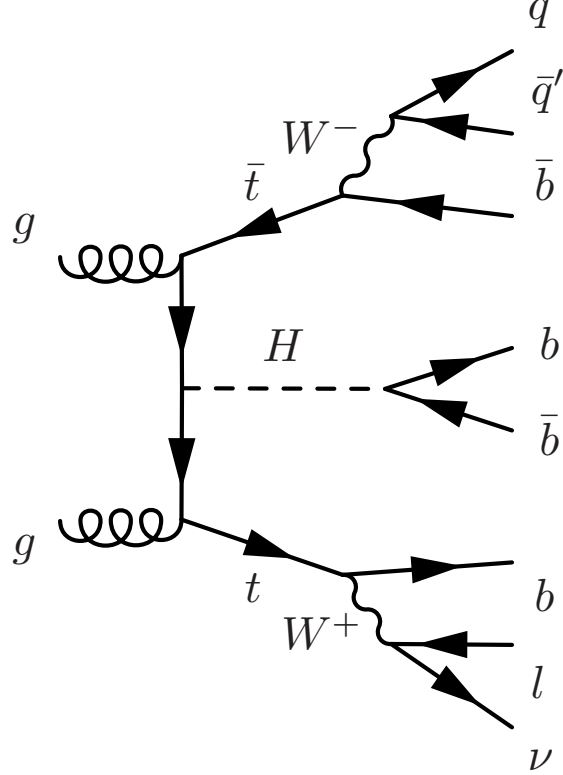


Figure 1.2: A Feynman diagram of the  $t\bar{t}H$  process, with  $H \rightarrow b\bar{b}$ , and the  $t\bar{t}$ -system decaying semi-leptonically

misidentifying which jets are the decay product of the Higgs, and thus additionally smears out the resolution on the mass of the Higgs. Due to the similarity of the  $t\bar{t} + b\bar{b}$  background and the combinatorics issue, no single variable is suitable for signal extraction. A Multi-Variate Analysis (MVA) technique is used in an attempt to isolate the  $t\bar{t}H$  signal from the  $t\bar{t} + jets$  background. The MVA provides a one-dimensional discriminant based on several input variables related to the kinematics of the event. This discriminant is then used to perform signal extraction and set upper-limits on  $t\bar{t}H$  production. The results of two searches will be presented. The first result used the first  $5.1 \text{ fb}^{-1}$  of the 2012 dataset, with center of mass energy of 8 TeV, and was published in the Journal of High Energy Physics (JHEP), May 2013. The second result was updated with the full  $19.4 \text{ fb}^{-1}$  8 TeV dataset, and was published in JHEP, September 2014.

## <sup>62</sup> Chapter 2

# <sup>63</sup> Theoretical Background

<sup>64</sup> The Standard Model (SM) of particle physics represents the sum of knowledge of the fundamen-  
<sup>65</sup> tal particles and their interactions with each other. It is a Quantum Field Theory (QFT) that  
<sup>66</sup> represents the interactions of each of the fundamental forces through the symmetry of a mathe-  
<sup>67</sup> matical object known as a Lie group. It is the theory that dictates the rate that the  $t\bar{t}H$  process  
<sup>68</sup> is produced, as well as the kinematics of every particle involved. As such, its predictions are  
<sup>69</sup> critical for modeling the characteristic signature of the  $t\bar{t}H$  signal in the CMS detector, as well as  
<sup>70</sup> the background processes, like  $t\bar{t} + b\bar{b}$  which leave a kinematically similar final state signature.

### <sup>71</sup> 2.1 An Overview of Quantum Field Theory

<sup>72</sup> Quantum Field Theory (QFT) was developed out of the need for a relativistic description of  
<sup>73</sup> quantum mechanics. Since the Einstein relation  $E = mc^2$  allows for the creation of particle-  
<sup>74</sup> antiparticle pairs, the single-particle description used in non-relativistic quantum mechanics,  
<sup>75</sup> fails describe this phenomenon [4]. This additionally fails when considering that Heisenberg's  
<sup>76</sup> uncertainty relation,  $\Delta E \cdot \Delta t = \hbar$ , allows for an arbitrary number of intermediate, virtual  
<sup>77</sup> particles to be created. By quantizing a field representing a certain type of particle, multiparticle  
<sup>78</sup> states are naturally described as discrete excitations of that field.

<sup>79</sup> Lorentz invariance, and the need to preserve causality, also define a fundamental relationship  
<sup>80</sup> between matter and antimatter. The propagation of a particle across a space-like interval is  
<sup>81</sup> treated equivalently to the an anti-particle propagating in the opposite direction [4]. This is  
<sup>82</sup> done so that the net probability amplitude for the particles to have an effect on a measurement  
<sup>83</sup> occurring across a space-like interval cancel each other, thus preserving causality. This cancel-  
<sup>84</sup> lation requirement additionally implies that the particle and anti-particle have the same mass,  
<sup>85</sup> with opposite quantum numbers such as spin or electric charge.

86 The Lorentz transformations for a scalar field are different than for a field with internal de-  
 87 grees of freedom, such as spin. A rotation on a vector field, will affect both its location, as well  
 88 as it's orientation [4]. This means the Lorentz invariant equation of motion describring a scalar  
 89 field will have a different form than equations of motion for a field with spin. The most relevant  
 90 equations describe the particles of SM, which contain spins of 0, 1/2, and 1. They are described  
 91 by the Klein-Gordan, Dirac, and Proca equations respectively.

92

Klein-Gordon equation, for scalar (spin 0) fields

$$(\partial^2 + m^2)\phi = 0 \quad (2.1)$$

Dirac equation, for spinor (spin 1/2) fields

$$(i\gamma^\mu \partial_\mu - m)\psi = 0 \quad (2.2)$$

Proca equation, for vector (spin 1) fields

$$\partial_\mu(\partial^\mu A^\nu - \partial^\nu A^\mu) + m^2 A^\nu = 0 \quad (2.3)$$

93 With these equations, one can build a theory of free particles. The Lagrangian formulation is  
 94 the most appropriate since all expressions are explicitly Lorentz invariant [4]. The Lagrangians  
 95 for the Klein-Gordon, Dirac, and Proca equations are given as:

96

Klein-Gordon Lagrangian, for real and complex scalar fields

$$\begin{aligned} \mathcal{L} &= \partial_\mu \partial^\mu \phi^2 - \frac{1}{2} m^2 \phi^2 \\ \mathcal{L} &= (\partial_\mu \phi)^*(\partial^\mu \phi) - m^2 (\phi)^*(\phi) \end{aligned} \quad (2.4)$$

Dirac Lagrangian, for spinor fields

$$\mathcal{L} = i\bar{\psi} \gamma^\mu \partial_\mu \psi - m\bar{\psi} \psi \quad (2.5)$$

Proca Lagrangian, for vector fields

$$\mathcal{L} = -\frac{1}{4} F_{\mu\nu} F^{\mu\nu} + m^2 A^\nu A_\nu \quad (2.6)$$

97 where  $F_{\mu\nu}$ , is the field strength tensor, defined as  $F_{\mu\nu} = \partial_\mu A_\nu - \partial_\nu A_\mu$

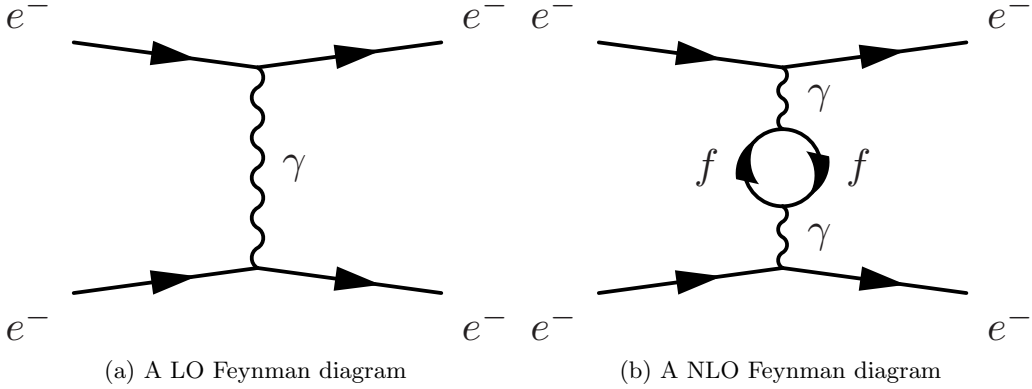


Figure 2.1: Leading and Next to Leading Order Feynman diagrams for the coulomb scattering process

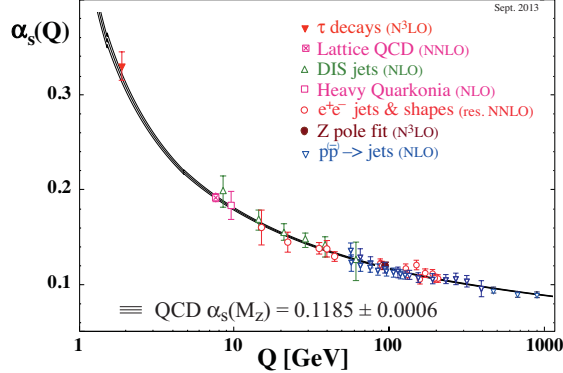
98        Interactions are generated by coupling multiple fields together in a single term, such as  
 99         $ieA_\mu\bar{\psi}\psi$  and treating it as a perturbation to the free field theory. This implies every interaction  
 100      between particles is carried out by a virtual mediating particle. When two electrons scatter off  
 101      one another, they are really exchanging a virtual photon, the mediator of the electromagnetic  
 102      force. The  $W^\pm$  and  $Z$  bosons mediate the weak force, while the *gluons* mediate the strong force.

$$\mathcal{L} = \mathcal{L}_{Free} + \mathcal{L}_{Interacting} \quad (2.7)$$

103       In order to calculate the probability and dynamics of two particles interacting with one  
 104      another, an integral, constrained by energy and momentum conservation, over the phase space  
 105      of outgoing particles and the scattering amplitude,  $\mathcal{M}$ , is evaluated. The scattering amplitude is  
 106      calculated by using the propagator (Green's function of the free particle theory) for the incoming,  
 107      mediating, and outgoing particles, with an appropriate weighting function, or vertex factor,  
 108      for each point the particles interact in the scattering process, and then integrating over the  
 109      momentum of the mediating particle. Richard Feynmann developed a set of rules for the writing  
 110      down the propagators and vertex factors directly from the Lagrangian, and easily computing the  
 111      scattering amplitude. He also introduced an elegant pictographic notation useful for visualizing  
 112      particle interactions, known as Feynmann diagrams.

113       With these tools, one can calculate the probability amplitudes of a given process occurring  
 114      to Leading Order (LO) without any difficulties. However, when calculations in Next to Leading  
 115      Order (NLO) are performed, and loop diagrams of virtual particles are considered, the probability  
 116      amplitudes associated with a given process diverge to infinity. This occurs when one integrates  
 117      over all of the possible momentum allowed by intermediate, loops of virtual particles, which due  
 118      to Heisenberg's uncertainty principle, are allowed to take on any value of momentum. Figure  
 119      2.1 shows an example of a LO and NLO process.

120       The systematic removal of divergences from a theory is called renormalization. The di-

Figure 2.2: The global average of  $\alpha_s$ , the QCD coupling constant.

vergences are absorbed into the definitions of the free parameters of the theory, making the parameters a function of the energy scale the process occurs at, instead of a constant. This allows for the calculations of fundamental processes to completed, as long as the energy scale of the interaction is known. A modern interpretation of renormalization was provided by Kenneth Wilson [5] [6]. Instead of seeing the effects of high momentum calculations after moving to NLO in perturbation theory, one uses an effective Lagrangian, computed by integrating out shells of momentum beginning at the energy cutoff of the theory, where the NLO effects begin the dominate. The dimensions of integration are then rescaled and the result of evaluating the integral over the momentum shell is absorbed into the definition of free parameters. The processes is iterated until the energy scale of the interaction is reached. The functional dependence of the parameters is then directly present in the resulting effective Lagrangian, instead of appearing suddenly when accounting for the one-loop contributions at NLO. Regardless of how strange this procedure seem, the running of the coupling constant as a function of interaction engergy has been validated experimentally time and time and again, as shown in Figure 2.2 [7].

## 2.2 Abelian Gauge Theories of Particle Interactions

In 1930, Herman Weyl introduced the idea that the interactions between fields can be generated by requiring them to be invariant under guage tansformations of a local symmetry [8]. For electromagnetism, the local symmetry is that of the Lie group,  $U(1)$ . It is an abelian group, which has the property that the generators of the group symmetry commutes with themselves. The  $U(1)$  symmetry is invariant under phase rotations. By requiring local guage invariance, the Lagrangian must be unchanged under the

$$\psi(x) \rightarrow e^{i\alpha(x)}\psi(x). \quad (2.8)$$

<sup>142</sup> Consider the Lagrangian for a free spin 1/2 particle:

$$\mathcal{L} = \bar{\psi}(i\gamma^\mu \partial_\mu - m)\psi \quad (2.9)$$

<sup>143</sup> The first term in the Lagrangian, involving the derivative, acts on  $\alpha(x)$ , creating a new term in  
<sup>144</sup> the Lagrangian, breaking its invariance under the local phase transformation.

$$\mathcal{L} \rightarrow \mathcal{L} - (\partial_\mu \alpha) \bar{\psi} \gamma^\mu \psi \quad (2.10)$$

<sup>145</sup> Thus, a new term must be added to the original Lagrangian to cancel out the term arising from  
<sup>146</sup> the local phase transformation. This is achieved by defining the covariant derivative:

$$D_\mu = \partial_\mu + ieA_\mu \quad (2.11)$$

<sup>147</sup> where  $A_\mu$  is a new vector field that transforms as follows:

$$A_\mu(x) \rightarrow A_\mu(x) - \frac{1}{e}\partial_\mu \alpha(x) \quad (2.12)$$

<sup>148</sup> The covariant derivative thus transforms like

$$\begin{aligned} D_\mu \psi(x) &\rightarrow [\partial_\mu + ie(A_\mu - \frac{1}{e}\partial_\mu \alpha)] e^{i\alpha(x)} D_\mu \psi(x) \\ &= e^{i\alpha(x)} [\partial_\mu + ie(A_\mu - \frac{1}{e}\partial_\mu \alpha + \frac{1}{e}\partial_\mu \alpha)] D_\mu \psi(x) \\ &= e^{i\alpha(x)} (\partial_\mu + ieA_\mu) \psi(x) \\ &= e^{i\alpha(x)} D_\mu \psi(x) \end{aligned} \quad (2.13)$$

<sup>149</sup> This covariant derivative transforms in the same way that  $\psi(x)$  does, and the new locally gauge  
<sup>150</sup> invariant Lagrangian becomes

$$\begin{aligned} \mathcal{L} &= \bar{\psi}(i\gamma^\mu D_\mu - m)\psi - \frac{1}{4}F^{\mu\nu}F_{\mu\nu} \\ &= i\bar{\psi}\gamma^\mu \partial_\mu \psi - \bar{\psi}\gamma^\mu \psi A_{\mu u} - m\bar{\psi}\psi - \frac{1}{4}F^{\mu\nu}F_{\mu\nu} \end{aligned} \quad (2.14)$$

<sup>151</sup> where

$$F^{\mu\nu} = (\partial^\mu A^\nu - \partial^\nu A^\mu) \quad (2.15)$$

<sup>152</sup> and  $\frac{1}{4}F^{\mu\nu}F_{\mu\nu}$  is the kinetic energy term of the Proca equation for the new vector field.

<sup>153</sup> This new Lagrangian is identical to the QED Lagrangian, except it was derived beginning  
<sup>154</sup> with a free Dirac theory and requiring the field to be locally gauge invariant under  $U(1)$  transfor-  
<sup>155</sup> mations. This necessitated the introduction of a new vector field,  $A_\mu$ , as well as an interaction

<sup>156</sup> term with it. This implies that the electromagnetic force can be represented by the requirement  
<sup>157</sup> of local  $U(1)$  symmetry on a free Dirac particle.

<sup>158</sup> It should be noted, that if the photon had mass, an additional term from the Proca equation  
<sup>159</sup> would have to be added to the Lagrangian,  $m^2 A_\mu A^\mu$ . This term complicates the picture since  
<sup>160</sup> it is not invariant under local phase transformations, and cannot be compensated for through a  
<sup>161</sup> different choice of  $A_\mu$ . This implies that the bosons of a gauge theory must be massless in order  
<sup>162</sup> to preserve local gauge invariance.

### <sup>163</sup> 2.3 Non-Abelian Gauge Theories of Particle Interactions

<sup>164</sup> In 1954, Yang and Mills worked to extend this idea to symmetries of different gauge groups [9].  
<sup>165</sup> Their most important accomplishment was developing this procedure for non-abelian groups.  
<sup>166</sup> These are groups, where the transformation does not involve a simple variable  $\alpha(x)$ , but rather an  
<sup>167</sup> entire matrix of dimension  $n > 2$ . These matrices do not commute with each other, and their work  
<sup>168</sup> developed the procedure for applying local gauge invariance described above to the more complex,  
<sup>169</sup> higher dimensional symmetries, such as  $SU(2)$  and  $SU(3)$ . Consider the case of  $SU(2)$  symmetry.  
<sup>170</sup> The theory is appropriate for describing the dynamics of two fermion fields, represented as a  
<sup>171</sup> doublet:

$$\psi = \begin{pmatrix} \psi_1(x) \\ \psi_2(x) \end{pmatrix} \quad (2.16)$$

<sup>172</sup> this will transform under the  $SU(2)$  transformation as a two-component spinor:

$$\psi \rightarrow \exp\left(i\alpha^i \frac{\sigma_i}{2}\right) \psi \quad (2.17)$$

<sup>173</sup> where  $\sigma^i$  are the Pauli matrices:

$$\sigma^1 = \begin{pmatrix} 0 & 1 \\ 1 & 0 \end{pmatrix}, \sigma^2 = \begin{pmatrix} 0 & -i \\ i & 0 \end{pmatrix}, \sigma^3 = \begin{pmatrix} 1 & 0 \\ 0 & -1 \end{pmatrix} \quad (2.18)$$

<sup>174</sup> and have the commutation relation defined by:

$$\left[ \frac{\sigma^i}{2}, \frac{\sigma^j}{2} \right] = i\epsilon^{ijk} \frac{\sigma^k}{2} \quad (2.19)$$

<sup>175</sup> Similar to the case of the  $U(1)$  Abelian symmetry, in order to form a lagrangian that is locally  
<sup>176</sup> gauge invariant, three vector fields,  $A_\mu^i$ ,  $i = 1, 2, 3$ , are introduced, and coupled to  $\psi$  through the  
<sup>177</sup> covariant derivative:

$$D_\mu = (\partial_\mu - igA_\mu^i \frac{\sigma^i}{2}) \quad (2.20)$$

<sup>178</sup> to ensure that the derivative covaries with the transformation, the fields,  $A_\mu^i$  will transform like:

$$A_\mu^i \frac{\sigma^i}{2} \rightarrow A_\mu^i \frac{\sigma^i}{2} + \frac{1}{g}(\partial_\mu \alpha^i) \frac{\sigma^i}{2} + i \left[ \frac{\alpha^i \sigma^i}{2}, A_\mu^i \frac{\sigma^i}{2} \right] \quad (2.21)$$

<sup>179</sup> The third term, which was absent from the abelian form of the transformation, is necessary to  
<sup>180</sup> account for the non-commutation of the pauli matrices. This non-communtation also changes  
<sup>181</sup> the form of the field strength tensor,  $F_{\mu\nu}^i$ :

$$F_{\mu\nu}^i = \partial_\mu A_\nu^i - \partial_\nu A_\mu^i + g\epsilon^{ijk} A_\mu^j A_\nu^k \quad (2.22)$$

<sup>182</sup> The entire  $SU(2)$  invariant Lagrangian can then be written as:

$$\begin{aligned} \mathcal{L}_{Yang-Mills} &= -\frac{1}{4}F_{\mu\nu}^i F^{i\mu\nu} + \bar{\psi}(i\gamma^\mu D_\mu)\psi \\ &= -\frac{1}{4}F_{\mu\nu}^i F^{i\mu\nu} + \bar{\psi}(i\gamma^\mu \partial_\mu - igA_\mu^i \frac{\sigma^i}{2})\psi \end{aligned} \quad (2.23)$$

<sup>183</sup> This procedure generalizes to any continuous group of symmetries. The basic steps involve  
<sup>184</sup> idenitifying the generators of the transformation:

$$\psi(x) \rightarrow e^{i\alpha^a t^a} \psi \quad (2.24)$$

<sup>185</sup> where  $t^a$  are a set of matrices with the commutation relationship:

$$[t^a, t^b] = if^{abc}t^c \quad (2.25)$$

<sup>186</sup> where  $f^{abc}$  is the structure constant for the goup. The covariant derivative is then defined as:

$$D_\mu = \partial_\mu - igA_\mu^a t^a \quad (2.26)$$

<sup>187</sup> where the fields,  $A_\mu^a$ , transform like:

$$A_\mu^a \rightarrow A_\mu^a + \frac{1}{g}\partial_\mu \alpha^a + f^{abc}A_\mu^b \alpha^c \quad (2.27)$$

<sup>188</sup> the field strength tensor is then formed as:

$$F_{\mu\nu}^a = \partial_\mu A_\nu^a - \partial_\nu A_\mu^a + f^{abc} A_\mu^b A_\nu^c \quad (2.28)$$

<sup>189</sup> and finally, the locally, gauge invariant Lagrangian will have the form:

$$\begin{aligned}\mathcal{L}_{\text{General, non-Abelian}} &= -\frac{1}{4}F_{\mu\nu}^a F^{a\mu\nu} + \bar{\psi}(i\gamma^\mu D_\mu)\psi \\ &= -\frac{1}{4}F_{\mu\nu}^a F^{a\mu\nu} + \bar{\psi}(i\gamma^\mu \partial_\mu - igA_\mu^a t^a)\psi\end{aligned}\quad (2.29)$$

190 In 1964, Murray Gell-Mann and Zweig independently developed a model of hadron interactions,  
 191 that described the spectrum of baryons and mesons in terms of combinations of fundamental  
 192 particles, which Gell-Mann named quarks [10] [11] [12]. In their model, three quarks:  $u, d, s$   
 193 formed an  $SU(3)$  flavor symmetry. However, this did not explain the appearance of only two and  
 194 three quark combinations, the mesons and baryons. It also could not explain the spin statistics  
 195 of the baryons. The  $\Delta^{++}$ ,  $\Delta^-$ , and  $\Omega^-$ , particles all have  $uuu$ ,  $ddd$ ,  $sss$  quark combinations,  
 196 respectively, with their spins aligned. That is to say, these baryons seem to violate the Pauli-  
 197 exclusion principle since all three quarks seem to occupy the same quantum state simultaneously.

198 In 1964, O.W. Greenberg solved this problem by proposing that quarks also have an additional  
 199 quantum number, *color*, that come in three types: red, green, blue [13]. The requirement that  
 200 all stable hadrons be color neutral: either possessing equal amounts of all three colors in  $qqq$   
 201 combinations, or a  $q\bar{q}$  pair sharing the same color, also explained the observation of only 2 and  
 202 3 quark combinations in experiments. These three colors form an  $SU(3)$  symmetry, and is the  
 203 gauge symmetry describing the interactions of quarks and leptons. This theory is known as  
 204 Quantum Chromodynamics (QCD). Its derivation follows from the procedure outlined above.  
 205 This group has eight generators, known as the Gell-Mann matrices, and are defined as:

$$\begin{aligned}t^1 &= \frac{1}{2} \begin{pmatrix} 0 & 1 & 0 \\ 1 & 0 & 0 \\ 0 & 0 & 0 \end{pmatrix}, \quad t^2 = \frac{1}{2} \begin{pmatrix} 0 & -i & 0 \\ i & 0 & 0 \\ 0 & 0 & 0 \end{pmatrix}, \quad t^3 = \frac{1}{2} \begin{pmatrix} 1 & 0 & 0 \\ 0 & -1 & 0 \\ 0 & 0 & 0 \end{pmatrix} \\ t^4 &= \frac{1}{2} \begin{pmatrix} 0 & 0 & 1 \\ 0 & 0 & 0 \\ 1 & 0 & 0 \end{pmatrix}, \quad t^5 = \frac{1}{2} \begin{pmatrix} 0 & 0 & -i \\ 0 & 0 & 0 \\ i & 0 & 0 \end{pmatrix} \\ , \quad t^6 &= \frac{1}{2} \begin{pmatrix} 0 & 0 & 0 \\ 0 & 0 & 1 \\ 0 & 1 & 0 \end{pmatrix}, \quad t^7 = \frac{1}{2} \begin{pmatrix} 0 & 0 & 0 \\ 0 & 0 & -i \\ 0 & -i & 0 \end{pmatrix}, \quad t^8 = \frac{1}{2\sqrt{3}} \begin{pmatrix} 1 & 0 & 0 \\ 0 & 1 & 0 \\ 0 & 0 & -2 \end{pmatrix}\end{aligned}\quad (2.30)$$

206 and a Lagrangian defined as:

$$\begin{aligned}\mathcal{L}_{QCD} &= -\frac{1}{4}G_{\mu\nu}^a G^{a\mu\nu} + \bar{\psi}(i\gamma^\mu D_\mu)\psi \\ &= -\frac{1}{4}G_{\mu\nu}^a G^{a\mu\nu} + \bar{\psi}(i\gamma^\mu \partial_\mu - igA_\mu^a t^a)\psi\end{aligned}\quad (2.31)$$

207 where  $t^a$  are the Gell-Mann matrices defined in equation 2.30 and the fields  $A_\mu^a$  are the eight  
 208 mediators of the QCD force, the *gluons*.

209 Like all non-abelian guage theories, it is asymptotically free. Thus, the strength of the cou-  
 210 pling constant,  $\alpha_s$ , decreases as the momentum-transfer,  $Q$  in interaction increases. This allows  
 211 the use of perturbation theory for high-momentum calculations, therefore allowing calculations  
 212 of hadronic-processes for experimental evaluation.

The idea of local gauge invariance was successful in describing the dynamics of QED and QCD, which only contain massless gauge bosons. Theorists had long postulated that the weak force was so weak because it was being facilitated by massive bosons, but adding a mass term for a boson breaks the local gauge invariance. So, a tool was needed to reconcile the concept of local gauge invariance, which works so well for the other forces, with the prospect of the weak force being facilitated by massive gauge bosons.

## 2.4 The Higgs Mechanism in an Abelian Theory

In 1964 Peter Higgs introduced the idea that the gauge bosons can acquire their mass through the breaking of an underlying symmetry [14]. In other words, the natural symmetry of the Lagrangian describing a particular interaction could be different than the symmetry we observe in nature. Consider an abelian example of complex scalar field theory, coupled to itself and to an electromagnetic field [4].

$$\mathcal{L} = -\frac{1}{4}(F_{\mu\nu})^2 + |D_\mu\phi|^2 - V(\phi) \quad (2.32)$$

where  $D_\mu = \partial_\mu + ieA_\mu$ , is the familiar covariant derivative, and the Lagrangian is invariant under the  $U(1)$  transformation as described earlier. The potential term,  $V(\phi)$  has the form

$$V(\phi) = -\mu^2\phi^*\phi + \frac{\lambda}{2}(\phi^*\phi)^2 \quad (2.33)$$

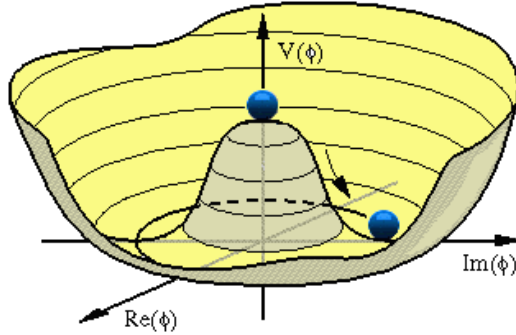


Figure 2.3: A visual representation of the Higgs potential

if  $\mu^2 > 0$  the shape of the potential no longer has a minimum at  $\langle\phi\rangle = 0$ . Figure 2.3 shows a plot of the potential energy of  $\phi$  in terms of each of its components. The new minimum potential energy occurs at:

$$\langle\phi\rangle = \phi_0 = \left(\frac{\mu^2}{\lambda}\right)^{1/2} \quad (2.34)$$

and while the field has a ground state at the zero potential point it is in an unstable equilibrium. Any quantum fluctuation about this point will take the field into the lower energy configuration with a ground state about the new minimum. When the Langrangian is expanded about 2.34, the field,  $\phi$  is rewritten as:

$$\phi(x) = \phi_0 + \frac{1}{\sqrt{2}}(\phi_1(x) + i\phi_2(x)) \quad (2.35)$$

the potential term,  $V(x)$ , then becomes:

$$V(x) = -\frac{1}{2\lambda}\mu^4 + \frac{1}{2} \cdot 2\mu^2\phi_1^2 + \mathcal{O}(\phi_i^3) \quad (2.36)$$

where we can notice that  $\phi_1$  has acquired a mass term with,  $m = \sqrt{2}\mu$ , while the scalar field  $\phi_2$  remains massless, and is known as the Goldstone boson. The covariant derivative is also transformed as:

$$|D_\mu\phi|^2 = \frac{1}{2}(\partial_\mu\phi_1)^2 + \frac{1}{2}(\partial_\mu\phi_2)^2 + \sqrt{2}e\phi_0 \cdot A_\mu\partial^\mu\phi_2 + e^2\phi_0^2A_\mu A^\mu + \dots \quad (2.37)$$

where cubic and quartic terms of  $A_\mu$ ,  $\phi_1$ , and  $\phi_2$  have been dropped. The important term is the last one, which can be interpreted as a mass term of the vector field,  $A_\mu$

$$\Delta\mathcal{L}_M = \frac{1}{2}m_A A_\mu A^\mu = e^2\phi_0^2 A_\mu A^\mu \quad (2.38)$$

where  $m_A = 2e^2\phi_0^2$ , has arisen from consequences of a non-zero vacuum expectation value of the  $\phi$  field. The remaining, massless Godlstone boson,  $\phi_2$  is not a physical particle, but rather a consequence of the choice of guage. This is illustrated when we can use the  $U(1)$  guage symmetry to rotate the field  $\phi(x)$  such that the field disappears.

$$\begin{aligned} \phi &\rightarrow \phi' = e^{i\alpha}(\phi_1 + \phi_2) \\ &= (\cos\alpha + i\sin\alpha)(\phi_1 + \phi_2) \\ &= (\phi_1 \cos\alpha - \phi_2 \sin\alpha) + i(\phi_1 \sin\alpha + \phi_2 \cos\alpha) \\ &= (\phi_1 - \phi_2 \tan\alpha) + i(\phi_1 \tan\alpha + \phi_2) \end{aligned} \quad (2.39)$$

Choosing  $\alpha = -\tan\phi_2/\phi_1$  will make  $\phi'$  a real quantity and elminate it's imaginary component,  $\phi'_2$ . The lagrangian can then be rewritten in terms of the rotated field  $\phi'$  and see that massless boson is indeed removed from the theory.

$$\begin{aligned}\mathcal{L} = & \frac{1}{2}(\partial_\mu\phi'_1)(\partial^\mu\phi'_1) - \frac{1}{2} \cdot 2\mu^2\phi'_1\phi'_1 \\ & - \frac{1}{4}(F^{\mu\nu}F_{\mu\nu}) + \frac{1}{2} \cdot e^2\phi_0^2A_\mu A^\nu \\ & + \phi_0e^2\phi'_1A_\mu A^\mu + \frac{1}{2}e^2\phi'^2A_\mu A^\mu + \mathcal{O}(\phi'^3)\dots\end{aligned}\quad (2.40)$$

247 The degree of freedom that  $\phi_2$  represents, is absorbed as a longitudinal polarization of the  
248  $A_{mu}$  field, a forbidden for massless gauge bosons, but necessary for massive bosons.

249 For this case of an abelian symmetry  $U(1)$ , it was shown that if a complex scalar field, which  
250 interacts with itself and another vector field, can gain a non-zero vacuum expectation value.  
251 The Lagrangian can be expanded about this new minimum, generating a mass term for the  
252 vector field. One of the degrees of freedom of the original complex scalar field is then absorbed  
253 as a longitudinal polarization state of the massive vector field.

## 254 2.5 The Higgs Mechanism in a non-Abelian Theory

255 Before describing the electroweak gauge theory of  $SU(2) \otimes U(1)$ , it will be helpful to see the effects  
256 of the Higgs mechanism for the non-Abelian group,  $SU(2)$  by itself. Consider an example  
257 of an  $SU(2)$  gauge field coupled to a scalar field that transforms like a real-valued vector under  
258  $SU(2)$  transformations [4]. The field  $\phi$  will have the form:

$$\phi = \begin{pmatrix} \phi_1 \\ \phi_2 \\ \phi_3 \end{pmatrix} \quad (2.41)$$

259 where the components,  $\phi_i$  are real-valued fields. The  $SU(2)$  transformation for this scalar field  
260 will also look like:

$$\phi \rightarrow e^{i\alpha^i T^i} \phi \quad (2.42)$$

261 where the matrices,  $T^i$  are defined as:

$$iT^1 = \begin{pmatrix} 0 & 0 & 0 \\ 0 & 0 & 1 \\ 0 & -1 & 0 \end{pmatrix}, \quad T^2 = \begin{pmatrix} 0 & 0 & -1 \\ 0 & 0 & 0 \\ 1 & 0 & 0 \end{pmatrix}, \quad T^3 = \begin{pmatrix} 0 & 1 & 0 \\ -1 & 0 & 0 \\ 0 & 0 & 0 \end{pmatrix} \quad (2.43)$$

262 The Lagrangian for this field will feature a Higgs potential term along with the previously  
263 mentioned  $SU(2)$  gauge fields,  $A_\mu^a$  coupled to the scalar field,  $\phi$ , and is given by:

$$\mathcal{L} = -\frac{1}{4}F_{\mu\nu}^a F^{a\mu\nu} + |D_\mu\phi|^2 + \mu^2\phi^*\phi - \frac{\lambda}{4}(\phi^*\phi)^2 \quad (2.44)$$

264 where  $F_{\mu\nu}^a$ , the field strength tensor is defined as:

$$F_{\mu\nu}^a = (\partial_\mu A_\nu^a - \partial_\nu A_\mu^a) + g\epsilon^{abc} A_\mu^b A_\nu^c \quad (2.45)$$

265 and the covariant derivative is defined as:

$$D_\mu = (\partial_\mu + igA_\mu^a T^a)\phi \quad (2.46)$$

266 Similarly to the Abelian case, the Higgs potential will induce a spontaneous symmetry breaking,  
267 and one of the components of the field  $\phi$  will gain a vacuum expectation value. After this  
268 breaking and expanding around the ground state potential, the field  $\phi$  will have the form:

$$\phi = \frac{1}{\sqrt{2}} \begin{pmatrix} 0 \\ 0 \\ v+h \end{pmatrix} \quad (2.47)$$

269 There has been no loss in generality in assuming this form since, similarly to the abelian case,  
270 we can use the gauge symmetry of  $SU(2)$  to rotate the field into this configuration. Goldstone's  
271 theorem tells us that we should expect two massive gague bosons corresponding to the  $T^1$ , and  
272  $T^2$  generators, while the  $T^3$  generator will correspond to a massless gauge boson, since  $\phi$  is still  
273 invariant under  $T^3$  transformations.

274 As in the Abelian case, the mass terms for the gauge bosons are generated from the covariant  
275 derivative term,  $|D_\mu\phi|^2$

$$\begin{aligned} D_\mu\phi &= \frac{1}{\sqrt{2}} \left( \partial_\mu + gA_\mu^1 \begin{pmatrix} 0 & 0 & 0 \\ 0 & 0 & 1 \\ 0 & -1 & 0 \end{pmatrix} + gA_\mu^2 \begin{pmatrix} 0 & 0 & -1 \\ 0 & 0 & 0 \\ 1 & 0 & 0 \end{pmatrix} + gA_\mu^3 \begin{pmatrix} 0 & 1 & 0 \\ -1 & 0 & 0 \\ 0 & 0 & 0 \end{pmatrix} \right) \begin{pmatrix} 0 \\ 0 \\ v+h \end{pmatrix} \\ &= \frac{1}{\sqrt{2}} \begin{pmatrix} 0 \\ 0 \\ \partial_\mu \end{pmatrix} + \frac{gA_\mu^1}{\sqrt{2}} \begin{pmatrix} 0 \\ v+h \\ 0 \end{pmatrix} - \frac{gA_\mu^2}{\sqrt{2}} \begin{pmatrix} v+h \\ 0 \\ 0 \end{pmatrix} \\ &= \frac{1}{\sqrt{2}} \begin{pmatrix} g(v+h)A_\mu^1 \\ g(v+h)A_\mu^2 \\ \partial_\mu h \end{pmatrix} \end{aligned} \quad (2.48)$$

276 Therefore

$$|D_\mu \phi|^2 = \frac{1}{2} \partial_\mu h \partial^\mu h + \frac{g^2 v^2}{2} ((A_\mu^1)^2 + (A_\mu^2)^2) + \frac{g^2}{2} (h^2 + 2hv) ((A_\mu^1)^2 + (A_\mu^2)^2) \quad (2.49)$$

This theory produces two massive bosons,  $A_\mu^1$  and  $A_\mu^2$ , both with mass,  $m_A = gv$ . These fields have  $h$ , and  $h^2$  couplings to the Higgs boson. The third gauge field,  $A_\mu^3$ , remains massless and is not coupled to the Higgs field. This model is beginning to resemble a description of electroweak physics, however, a third massive boson is necessary, as is a new gauge symmetry in order to generate it. That is the subject of the next section.

## 2.6 Glashow Weinberg Salam Theory

Glashow, Weinberg, and Salam published their theory unifying electromagnetic and weak forces in the 1960s [15] [16] [17]. It begins with the requirement of a  $SU(2)_L \otimes U(1)$  symmetry and incorporates the Higgs mechanism to give mass to the gauge bosons of the weak force. As described earlier, the  $U(1)$  symmetry requires introducing a vector field, which will be labeled  $B_\mu$ , and an interaction term, which is absorbed into the covariant derivative,  $D_\mu$ . The transformation will also be parameterized with a with a quantum number,  $Y$ , known as hypercharge. The  $SU(2)$  symmetry requires the introduction of three new vector fields, which will be labeled  $W_\mu^i, i = 1, 2, 3$ . The quantum number associated with this gauge group is known as isospin, and is determined by the  $T^3$  operator, acting on an  $SU(2)$  doublet on the third generator of the group. The  $SU(2) \otimes U(1)$  transformation,  $U(x)$ , will then be given by:

$$U(x) = e^{i\alpha^a(x)\tau^a} e^{iY\alpha(x)} \quad (2.50)$$

where  $\tau^a = \sigma^a/2$ , the Pauli matrices, 2.18. These gauge fields will be coupled, via the covariant derivative, to a doublet of complex scalar fields  $\phi$ , with hypercharge  $Y = +1/2$ . A Higgs potential will be added to generate the spontaneous symmetry breaking that will give mass to three of the gauge fields, and leave one massless. In order to preserve the  $SU(2)_L \otimes U(1)$  symmetry, the new covariant derivative will take the form:

$$D_\mu = (\partial_\mu - igW_\mu^a \tau^a - \frac{i}{2}g'B_\mu) \quad (2.51)$$

The subscript L on  $SU(2)_L$  refers to the experimental results that the weak force violates parity maximally, by only interacting with the left-handed chiral component of a field. Right versus left chirality is determined by whether the spin of a particle is aligned or anti-aligned with its direction of motion, and in general a particle is represented by a linear combination

of its right and left handed components. This idea was first proposed by Chen Ning Yang and Tsung-Dao Lee, in the 1950s. Their ideas were validated by the experimental discovery of parity violation in 1957, through the beta decays of Cobalt 60 atoms by C.S Wu. That same year, Yang and Lee were awarded the nobel prize for their insight [18]. In this model, then, the left-handed components of the particles participate in the weak interaction and are formed into doublets, while the right handed components are singlets, and will only interact with the electromagnetic field,  $B_\mu$ . The quantum numbers of the doublet will be given by +1/2 for the upper component of the  $SU(2)$  doublet, and -1/2 for the lower component. The fermion content of this theory is then given by:

$$\begin{pmatrix} \nu_L \\ e_L \end{pmatrix}, e_R \quad \begin{pmatrix} u_L \\ d_L \end{pmatrix}, u_R, d_R \quad (2.52)$$

where the right handed neutrino,  $\nu_R$  has been omitted, since it has zero charge, and isospin, and therefore does not participate in any of the interactions of this theory. The complete Lagrangian is given by a sum of free particle terms for massless bosons, fermions, and Higgs scalar fields; the Higgs potential; and a Yukawa coupling term between the fermions and the Higgs, which generates their masses.

$$\mathcal{L}_{GWS} = \mathcal{L}_{BosonKE} + \mathcal{L}_{Higgs} + \mathcal{L}_{FermionKE} + \mathcal{L}_{Yukawa} \quad (2.53)$$

The Higgs potential will have the form:

$$\mathcal{L}_{Higgs} = (D_\mu \phi)^\dagger (D^\mu \phi) + \mu^2 \phi^\dagger \phi - \lambda (\phi^\dagger \phi)^2 \quad (2.54)$$

The Higgs potential will break the symmetry of the Lagrangian when one of the four degrees of freedom in the complex scalar doublet,  $\phi$ , spontaneously acquires a vacuum expectation value. In this case, it will generate three massive gauge bosons, one massless gauge boson, and a massive scalar field. After gaining a vacuum expectation value, and expanding about this value, the scalar fields will have the form:

$$\langle \phi \rangle = \frac{1}{\sqrt{2}} \begin{pmatrix} 0 \\ v + h \end{pmatrix} \quad (2.55)$$

where no loss of generality has occurred since we are always able to rotate into this form through the appropriate gauge transformations, similar to what was described in the Abelian case. It should also be noted that this form is not invariant to any of the individual generators  $t^a$ , however  $\phi$  will be invariant to a combination of  $T^3 + Y$  generators. Per Goldstone's theorem, we

should expect this linear combination of fields to be the massless vector boson after symmetry breaking. The massless eigenstate will be the electromagnetic field,  $A_\mu \sim A_\mu^3 + B_\mu$ . The electric charge quantum number,  $Q$ , is then defined as

$$Q = T^3 + Y \quad (2.56)$$

<sup>321</sup> As before, the generation of the masses for the gauge bosons are generated by the interaction  
<sup>322</sup> of their fields with the Higgs field via the covariant derivative.

$$\begin{aligned} D_\mu \phi &= \frac{1}{\sqrt{2}} \left( \partial_\mu - \frac{ig}{2} A_\mu^1 \begin{pmatrix} 0 & 1 \\ 1 & 0 \end{pmatrix} - \frac{ig}{2} A_\mu^2 \begin{pmatrix} 0 & -i \\ i & 0 \end{pmatrix} - \frac{ig}{2} A_\mu^3 \begin{pmatrix} 1 & 0 \\ 0 & -1 \end{pmatrix} \right) \begin{pmatrix} 0 \\ v+h \end{pmatrix} \\ &= \frac{1}{\sqrt{2}} \left( \partial_\mu + i(\frac{1}{2}(v+h)(gA_\mu^3 - g'B_\mu)) \right) \end{aligned} \quad (2.57)$$

<sup>323</sup> Taking the dot product of this with its hermitian conjugate gives the  $|D_\mu \phi|^2$  term:

$$\begin{aligned} |D_\mu \phi|^2 &= \frac{1}{2} \partial_\mu h \partial^\mu h + \frac{1}{2} \frac{g^2 v^2}{4} ((A_\mu^1)^2 + (A_\mu^2)^2) + \frac{v^2}{4} (gA_\mu^3 - g'B_\mu)^2 \\ &\quad + \frac{1}{2} g^2 4(h^2 + 2vh)((A_\mu^1)^2 + (A_\mu^2)^2) + \frac{1}{2} \frac{1}{4}(h^2 + 2vh)(gA_\mu^3 - g'B_\mu) \end{aligned} \quad (2.58)$$

<sup>324</sup> From equation 2.58 we can identify three massive and one massless gauge bosons, corresponding  
<sup>325</sup> to the charged and neutral weak currents, and the electromagnetic current.

$$\begin{aligned} W_\mu^\pm &= \frac{1}{\sqrt{2}} (A_\mu^1 \mp iA_\mu^2) && \text{with mass } m_W = g \frac{v}{2}; \\ Z_\mu^0 &= \frac{1}{\sqrt{g^2 + g'^2}} (gW_\mu^3 - g'B_\mu) && \text{with mass } m_Z = \frac{v}{2} \sqrt{g^2 + g'^2}; \\ A_\mu &= \frac{1}{\sqrt{g^2 + g'^2}} (gW_\mu^3 + g'B_\mu) && \text{with mass } m_A = 0; \end{aligned} \quad (2.59)$$

<sup>326</sup> where the last field,  $A_\mu$  is absent from the covariant derivative term, but already identified as  
<sup>327</sup> the massless gauge boson of the theory due to its gauge invariance under a  $T^3 + Y$  rotation.  
<sup>328</sup> Using these definitions the covariant derivative has the following form:

$$\begin{aligned} D_\mu &= \partial_\mu - \frac{ig}{\sqrt{2}} (W^+ T^+ + W^- T^-) \\ &\quad - \frac{i}{\sqrt{g^2 + g'^2}} Z_\mu^0 (gT^3 - g'Y) - \frac{gg'}{\sqrt{g^2 + g'^2}} A_\mu (T^3 + Y) \end{aligned} \quad (2.60)$$

<sup>329</sup> where  $T^\pm = \frac{1}{2}(\sigma^1 \pm \sigma^2)$ . From this form, we can identify the fundamental electric charge,  $e$ , as

$$e = \frac{gg'}{\sqrt{g^2 + g'^2}} \quad (2.61)$$

<sup>330</sup> The similarity in the forms between  $Z_\mu^0$  and  $A_\mu$  suggest that their relationship can be ex-  
<sup>331</sup> pressed in a simpler form, as the rotation of underlying guage fields  $A_\mu^3$  and  $B_\mu$  through the  
<sup>332</sup> weak mixing angle,  $\theta_W$

$$\begin{pmatrix} Z_\mu^0 \\ A_\mu \end{pmatrix} = \begin{pmatrix} \cos \theta_W & -\sin \theta_W \\ \sin \theta_W & \cos \theta_W \end{pmatrix} \begin{pmatrix} A_\mu^3 \\ B_\mu \end{pmatrix} \quad (2.62)$$

<sup>333</sup> where  $\tan \theta_W = \frac{g'}{g}$ . Expanding 2.62, we have the definitions of the  $Z_\mu^0$  and  $A_\mu$  fields in terms of  
<sup>334</sup>  $\theta_W$

$$\begin{aligned} Z_\mu^0 &= A_\mu^3 \cos \theta_W - B_\mu \sin \theta_W \\ A_\mu &= A_\mu^3 \sin \theta_W + B_\mu \cos \theta_W \end{aligned} \quad (2.63)$$

<sup>335</sup> The weak mixing angle,  $\theta_W$ , also provides a simple relationship between the  $W_\mu^\pm$  and  $Z_\mu^0$  fields:

$$m_W = m_Z \cos \theta_W \quad (2.64)$$

<sup>336</sup> The covariant derivative,  $D_\mu$  is also rewritten in terms of the mass eingenstates of the gauge  
<sup>337</sup> fields

$$D_\mu = (\partial_\mu - \frac{ig}{\sqrt{2}}(W_\mu^+ + W_\mu^- T^-) - \frac{ig}{\cos \theta_W} Z_\mu^0(T_3 - \sin^2 \theta_W Q) - ieA_\mu Q) \quad (2.65)$$

<sup>338</sup> where  $g = e/\cos \theta_W$ . The square of the covariant derivative is then written as

$$\begin{aligned} |D_\mu|^2 &= \frac{1}{2}\partial_\mu h \partial^\mu h + \frac{1}{2}m_W^2 W_\mu^+ W^{\mu+} + \frac{1}{2}m_W^2 W_\mu^- W^{\mu-} + \frac{1}{2}m_Z^2 Z_\mu^0 Z^{\mu 0} \\ &\quad + \left(\frac{h^2}{v^2} + \frac{h}{v}\right)\left[\frac{1}{2}m_W^2(W_\mu^+ W^{\mu+} + W_\mu^- W^{\mu-}) + \frac{1}{2}m_Z^2 Z_\mu^0 Z^{\mu 0}\right] \end{aligned} \quad (2.66)$$

<sup>339</sup>

<sup>340</sup>

<sup>341</sup> With the form of the covariant derivative in place, the fermionic kinematic term of the  
<sup>342</sup> Lagrangian can be described. As mentioned earlier, the masses of the fermions in the model  
<sup>343</sup> will be generated by the Yukawa interaction term with the Higgs, so this term only involves the  
<sup>344</sup> covariant derivatives acting on the left-handed doublet and right-handed singlet states of this  
<sup>345</sup> model.

<sup>346</sup> The quantum number assignments for the leptons, which are chosen in order to reproduce the  
<sup>347</sup> known values of their electric charges, are shown in table 2.1. The values of these quantum

	$\nu_L$	$e_L$	$e_R$	$u_L$	$d_L$	$u_R$	$d_R$
Isospin	+1/2	-1/2	0	+1/2	-1/2	0	0
Hypercharge	-1/2	-1/2	-1	+1/6	1/3	2/3	-1/3
Electric Charge	0	-1	-1	2/3	-1/3	2/3	-1/3

Table 2.1: The quantum numbers Isospin and Hypercharge are assigned for each of the  $SU(2)$  and  $U(1)$  symmetries respectively

numbers enter into the covariant derivative via the  $Z_\mu^0$  term of equation 2.65. The fermionic kinetic energy term of the Lagrangian is given by:

$$\begin{aligned} \mathcal{L}_{Fermion} = & \bar{E}_L(i\gamma^\mu D_\mu)E_L + \bar{e}_R(i\gamma^\mu D_\mu)e_R \\ & \bar{Q}_L(i\gamma^\mu D_\mu)Q_L + \bar{u}_R(i\gamma^\mu D_\mu)u_R + \bar{d}_R(i\gamma^\mu D_\mu)d_R \end{aligned} \quad (2.67)$$

Expanding the covariant term for the left-handed electron shows its explicit coupling to the gauge boson fields.

$$\begin{aligned} \mathcal{L}_{E_L} = & \begin{pmatrix} \bar{\nu}_L & \bar{e}_L \end{pmatrix} \left( (i\gamma^\mu(\partial_\mu - \frac{ig}{\sqrt{2}}(W_\mu^+T^+ + W_\mu^-T^-) - \frac{ig}{\cos\theta_W}Z_\mu^0(T^3 - \sin^2\theta_W Q) - ieA_\mu Q)) \right) \begin{pmatrix} \nu_L \\ e_L \end{pmatrix} \\ = & \bar{\nu}_L i\gamma^\mu \partial_\mu \nu_L + \bar{e}_L i\gamma^\mu \partial_\mu e_L + \frac{ig}{\sqrt{2}} W_\mu^+ \bar{\nu}_L \gamma^\mu e + \frac{ig}{\sqrt{2}} W_\mu^- \bar{e}_L \gamma^\mu \nu_L \\ & + \frac{ig}{\cos\theta_W} \bar{\nu}_L (1/2) \gamma^\mu \nu_L + \frac{ig}{\cos\theta_W} \bar{e}_L \gamma^\mu (-1/2 + \sin^2\theta_W (+1)) e_L + (ie) \bar{e}_L \gamma^\mu A_\mu (-1) \end{aligned} \quad (2.68)$$

All of the terms will be combined with the final, spontaneously broken GWS Lagranian at the end of this section.

The final term to discuss in the theory, before combing all of the results, is the Yukawa interaction term between the fermion fields and the Higgs. For the electron, this term takes the form:

$$\begin{aligned} \mathcal{L}_{Yukawa} = & -\lambda_e \bar{E}_L \cdot \phi e_R - \lambda_e E_L \cdot \phi \bar{e}_R \\ = & -\frac{\lambda_e}{\sqrt{2}} (v+h)(\bar{e}_L e_R + e_L \bar{e}_R) \\ = & -\frac{\lambda_e v}{\sqrt{2}} (\bar{e}_L e_R + e_L \bar{e}_R) - \frac{\lambda_e}{\sqrt{2}} (\bar{e}_L e_R + e_L \bar{e}_R) h \end{aligned} \quad (2.69)$$

where the mass of the electron is identified as  $m_e = \frac{\lambda_e v}{\sqrt{2}}$ . In order to generate the masses of the particles, each fermion has its own unique  $\lambda$  value. So while the Higgs mechanism is able to generate the masses in a way that preserves the underlying  $SU(2) \otimes U(1)$  symmetry, it does not explain the heirarchy of masses since each  $\lambda$  value is unique to each lepton. The second term in last equation of 2.69 is the coupling of the Higgs particle,  $h$ , to the fermions. The coupling is proportional to the mass of the particle. The largest of these is to the top quark,

<sup>363</sup> with  $m_t = 73.21 \pm 0.51 \pm 0.71 \text{GeV}$ .

<sup>364</sup> The Yukawa coupling for the quarks is necessarily modified when additional quarks besides  
<sup>365</sup> the  $u$  and  $d$  are added to the theory. This is because there can be additional coupling terms  
<sup>366</sup> that mix generations. This occurs when the mass eigenstate of the quarks is not the same as the  
<sup>367</sup> interaction eigenstate. The modification requires the expansion of the  $u_L$  and  $d_L$  components  
<sup>368</sup> into a vector of left handed quarks. If we let

$$u_L^i = (u_L, c_L, t_L), \quad d_L^i = (d_L, s_L, b_L) \quad (2.70)$$

<sup>369</sup> represent the up and down-type quarks in the original weak interaction basis, then the vectors,  
<sup>370</sup>  $u_L^i$  and  $d_L^i$ , can be defined as the diagonalized basis for the Higgs coupling. They are related  
<sup>371</sup> through a unitary transformation.

$$u_L^i = U_u^{ij} u_L^{j'}, \quad d_L^i = U_d^{ij} d_L^{j'} \quad (2.71)$$

<sup>372</sup> The interaction terms with the charged gauge boson currents must then be rewritten as

$$J_W^{\mu+} = \frac{1}{\sqrt{2}} \bar{u}_L^i \gamma^\mu d_L^i = \frac{1}{\sqrt{2}} \bar{u}_L^{i'} \gamma^\mu (U_u^\dagger U_d) d_L^{i'} = \frac{1}{\sqrt{2}} \bar{u}_L^{i'} \gamma^\mu V_{ij} d_L^{j'} \quad (2.72)$$

<sup>373</sup> where  $V_{ij}$  is the 3x3 Cabibbo-Kobayashi-Maskawa (CKM) matrix describing the mixing among  
<sup>374</sup> six quarks [19] [20]. It is an extension of the Glashow-Iliopoulos-Maiani mechanism, which  
<sup>375</sup> was a 2x2 matrix that predicted the existence of a fourth quark, the charm quark. The GIM  
<sup>376</sup> mechanism was an attempt to suppress flavor-changing-neutral currents, which occur at LO in  
<sup>377</sup> a three-quark model, but not in a four-quark model. The CKM matrix, however, was motivated  
<sup>378</sup> by an attempt to explain  $CP$  violation in the weak interaction. At the time of its publication,  
<sup>379</sup> the bottom and top quarks were not predicted. After these were discovered, they were awarded  
<sup>380</sup> the nobel prize in physics in 2008.

<sup>381</sup> At this point, all the pieces are ready to write down the GWS Lagrangian, after the  
<sup>382</sup> Higgs mechanism has spontaneously broken the  $SU(2) \otimes U(1)$  symmetry.

$$\begin{aligned} \mathcal{L}_{Unbroken} = & -\frac{1}{4} A_{\mu\nu}^a A^{\mu\nu a} - \frac{1}{4} F_{\mu\nu} F^{\mu\nu} \\ & + |D_\mu \phi|^2 + \mu^2 (\phi^\dagger \phi) - \lambda (\phi^\dagger \phi)^2 \\ & + \bar{E}_L (i\gamma^\mu D_\mu) E_L + \text{similar terms for } e_R, U_L, u_R, d_R \\ & - \lambda_e \bar{E}_L \cdot \phi e_R + h.c. + \text{similar terms for } e_R, U_L, u_R, d_R \end{aligned} \quad (2.73)$$

$$\begin{aligned}
\mathcal{L}_{GWS} = & -\frac{1}{4}(Z_{\mu\nu}^0)^2 - \frac{1}{2}(W_{\mu\nu}^+ W_{\mu\nu}^-) - \frac{1}{4}(F_{\mu\nu})^2 \\
& + ig \cos \theta_W ((W_\mu^- W_\nu^+ - W_\nu^- W_\mu^+) \partial^\mu Z^{0\nu} + W_{\mu\nu}^+ W^{-\mu} Z^{0\nu} + W_{\mu\nu}^- W^{+\mu} Z^{0\nu}) \\
& + ie ((W_\mu^- W_\nu^+ - W_\nu^- W_\mu^+) \partial^\mu A^\nu + W_{\mu\nu}^+ W^{-\mu} A^\nu - W_{\mu\nu}^- W^{+\mu} A^\nu) \\
& + g^2 \cos^2 \theta_W (W_\mu^+ W_\nu^- Z^{0\mu} Z^{0\nu} - W_\mu^+ W^{-\mu} Z_\nu^0 Z^{0\nu}) \\
& + g^2 (W_\mu^+ W_\mu^- A^\mu A^\nu - W_\mu^+ W^{-\mu} A_\nu A^\nu) \\
& + ge \cos \theta_W (W_\mu^+ W_\nu^- (Z^{0\mu} A_\nu + Z^{0\nu} A^\mu) - 2W_\mu^+ W^{-\mu} A^\nu) \\
& + \frac{1}{2}g^2 (W_\mu^+ W_\nu^-) (W^{+\mu} W^{-\nu} - W^{+\nu} W^{-\mu}) \\
& + \frac{1}{2}\partial_\mu h \partial^\nu h - v^2 \lambda h^2 + \frac{1}{2}m_W^2 W_\mu^+ W^{+\mu} + \frac{1}{2}m_W^2 W_\mu^- W^{-\mu} + \frac{1}{2}m_Z^2 Z_\mu^0 Z^{0\mu} \\
& + \left(\frac{h^2}{v^2} + \frac{h}{v}\right) \left(\frac{1}{2}m_W^2 (W_\mu^+ W^{+\mu} + W_\mu^- W^{-\mu}) + \frac{1}{2}m_Z^2 Z_\mu^0 Z^{0\mu}\right) - \lambda v h^3 - \frac{1}{4}\lambda h^4 \\
& + \bar{E}_L (i\gamma^\mu \partial_\mu) E_L + e_R^- (i\gamma^\mu \partial_\mu) e_R + \bar{Q}_L (i\gamma^\mu \partial_\mu) Q_L + u_R^- (i\gamma^\mu \partial_\mu) u_R + \bar{d}_R (i\gamma^\mu \partial_\mu) d_R \\
& + g (W_\mu^+ J_W^{\mu+} + W_\mu^- J_W^{\mu-} + Z_\mu^0 J_Z^\mu) + e A_\mu J_{EM}^\mu \\
& - \frac{\lambda_e v}{\sqrt{2}} (\bar{e}_L e_R + \bar{e}_R e_L) - \frac{\lambda_e h}{\sqrt{2}} (\bar{e}_L e_R + \bar{e}_R e_L) \\
& - \frac{\lambda_u v}{\sqrt{2}} (\bar{u}_L u_R + \bar{u}_R u_L) - \frac{\lambda_u h}{\sqrt{2}} (\bar{u}_L u_R + \bar{u}_R u_L) \\
& - \frac{\lambda_d v}{\sqrt{2}} (\bar{d}_L d_R + \bar{d}_R d_L) - \frac{\lambda_d h}{\sqrt{2}} (\bar{d}_L d_R + \bar{d}_R d_L)
\end{aligned} \tag{2.74}$$

where the currents of the electroweak interaction,  $J_W^{\mu+}$ ,  $J_W^{\mu-}$ ,  $J_Z^\mu$ ,  $J_A^\mu$  are defined as:

$$\begin{aligned}
J_W^{\mu+} &= \frac{1}{\sqrt{2}} (\bar{\nu}_L \gamma^\mu e_L + \bar{u}_L^i \gamma^\mu V_{ij} d_L^j) \\
J_W^{\mu-} &= \frac{1}{\sqrt{2}} (\bar{e}_L \gamma^\mu \nu_L + \bar{d}_L^i \gamma^\mu V_{ij} u_L^j) \\
J_Z^\mu &= \frac{1}{\cos \theta_W} (\bar{\nu}_L \gamma^\mu (+1/2) \nu_L + \bar{e}_L \gamma^\mu (-1/2 + \sin^2 \theta_W) e_L + \bar{e}_R \gamma^\mu \sin^2 \theta_W e_R \\
&\quad + \bar{u}_L \gamma^\mu (1/2 - 2/3 \sin^2 \theta_W) u_L + \bar{u}_R \gamma^\mu (-2/3 \sin^2 \theta_W) u_R \\
&\quad + \bar{d}_L \gamma^{mu} (-1/2 + 1/3 \sin^2 \theta_W) d_L + \bar{d}_R \gamma^\mu (1/3 \sin^2 \theta_W) d_R) \\
J_{EM}^\mu &= e_{L,R}^- \gamma^\mu (-1) e_{L,R} + u_{L,R}^- \gamma^\mu (2/3) u_{L,R} + d_{L,R}^- \gamma^\mu (-2/3) d_{L,R}
\end{aligned} \tag{2.75}$$

## 383 2.7 The Standard Model of Particle Physics

The Standard Model of particle physics, extends the GWS model by incorporating the QCD interaction between the quarks and gluons. The symmetry of this theory is that of:

$$SU(3)_C \otimes SU(2)_L \otimes U(1)_Y \tag{2.76}$$

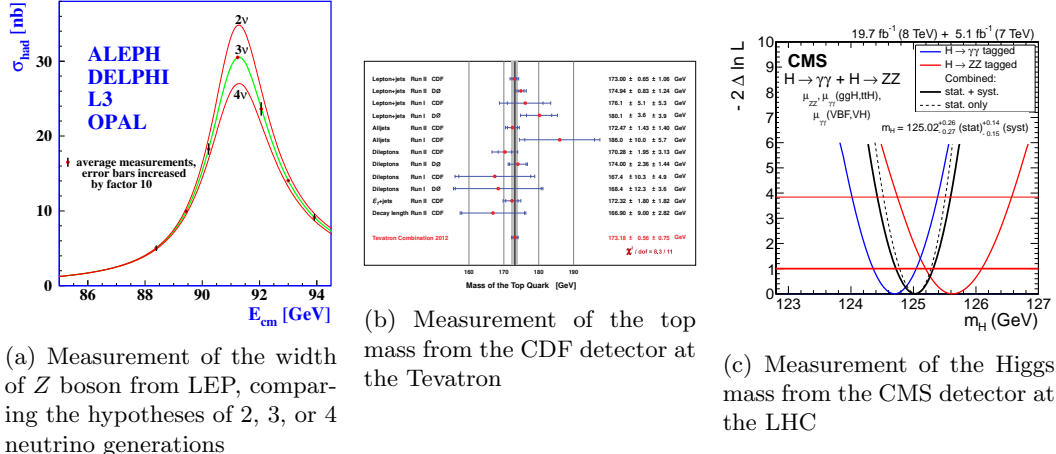


Figure 2.4: Experimental milestones of the Standard Model

<sup>384</sup> The Lagrangian of the model is given by

$$\mathcal{L}_{SM} = \mathcal{L}_{GWS} - \frac{1}{4} G_{\mu\nu}^a G^{a\mu\nu} + g_S C_\mu^a J_{QCD}^{a\mu} \quad (2.77)$$

<sup>385</sup> where the current for the QCD interaction,  $J_{QCD}^{a\mu}$  is defined as:

$$J_{QCD}^a = \bar{u}^i \gamma^\mu t^a u^i + \bar{d}^i \gamma^\mu t^a d^i \quad (2.78)$$

<sup>386</sup> where  $t^a$  are the Gell-Mann matrices defined in equation 2.30. The field strength tensor for the  
<sup>387</sup> eight gluon fields,  $G_{\mu\nu}^a$ , is defined as

$$G_{\mu\nu}^a = (\partial_\mu C_\nu^a - \partial_\nu C_\mu^a) - g_S f^{abc} C_\mu^b C_\nu^c \quad (2.79)$$

<sup>388</sup> The experimental evidence in favor of the SM is compelling. It has not only been able  
<sup>389</sup> to describe existing phenomenon to great precision, but has also predicted the existence of  
<sup>390</sup> new forms of matter and interactions among fundamental particles. The UA1 [21] [22] and  
<sup>391</sup> UA2 [23] [24] experiments at CERN, under the leadership of Carlo Rubbia, discovered the  
<sup>392</sup>  $W$  and  $Z$  bosons in 1983. The experiments observed a handful of events, in  $p\bar{b}$  collisions, at  
<sup>393</sup>  $\sqrt{s} = 540$  GeV, and were able to measure the masses to be  $M_W \sim 80$  GeV and  $M_Z \sim 95$  GeV.

<sup>394</sup> In the following years, from 1989-2000, the Large electron-positron (LEP) collider at CERN  
<sup>395</sup> conducted precision measurements of the Standard Model [25] [26]. Along with high-precision  
<sup>396</sup> measurements on the  $W, Z$  masses:

$$m_Z = 91.1875 \pm 0.0021 \text{ GeV} \quad (2.80)$$

$$m_W = 80.376 \pm 0.0033 \text{ GeV}$$

<sup>397</sup> the experiment was also able to put stringent limits on the existence of more than three families of

leptons and quarks by measuring the width of the  $Z$  boson. Figure 2.4(a) shows the comparison of two, three, and four family hypotheses to data.

Another milestone for the Standard Model occurred in 1995 when the CDF [27] and D0 experiments [28] at the Tevatron announced the observation of the top quark, with  $m_t \sim 176$  GeV, in  $p\bar{p}$  collisions at  $\sqrt{s} = 1.8$  TeV. Figure 2.4(c) shows a plot from 2012, the latest top quark mass measurements from CDF, which reports a  $m_t = 173.18 \pm 0.56 \pm 0.75$  GeV. It was the last quark predicted by the CKM matrix to be observed, and earned Makoto Kobayashi and Toshihide Maskawa the nobel prize in 2008 for their work extending the quark sector to three families and parameterizing their electroweak mixing.

Yet another milestone was reached in 2012, when the CMS and ATLAS detectors at CERN announced the observation of a new boson, with characteristics strikingly similar to the elusive Higgs boson of the SM. Figure 2.4(c) shows the latest measurement results on the mass from the  $H \rightarrow \gamma\gamma$  and  $H \rightarrow ZZ$  channels, with a  $m_H = 125.02 \pm 0.27 \pm 0.15$ . One of the most important remaining goals is to measure the couplings of this new boson to all of the other particles in the Standard Model. Of particular interest is the coupling to the top-quark, since it offers the largest value of the Higgs Yukawa coupling to measure. This offers a test of the nature of the coupling, as well as a probe into deviations from its value.

## 2.8 Higgs Production in $pp$ Collisions at the LHC

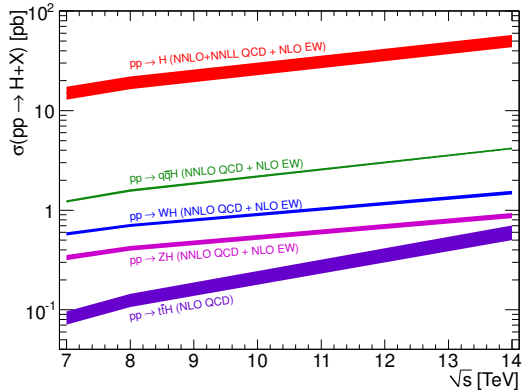


Figure 2.5: Higgs production cross-sections at the LHC, for 7–14 TeV  $pp$  collisions

The rest of the thesis will describe the search for Higgs boson production in proton-proton collisions at the LHC, so it will be useful to understand the production mechanisms for the Higgs in this scenario. At the LHC collision energies 7 – 14 TeV, there are four dominant production mechanisms that produce Higgs events: gluon-gluon fusion (ggf), vector-boson fusion (vbf), associated production with vector bosons (VH), and associated production with top-quark pairs (tth). Figure 2.5 shows the relative cross sections for each of these mechanisms.

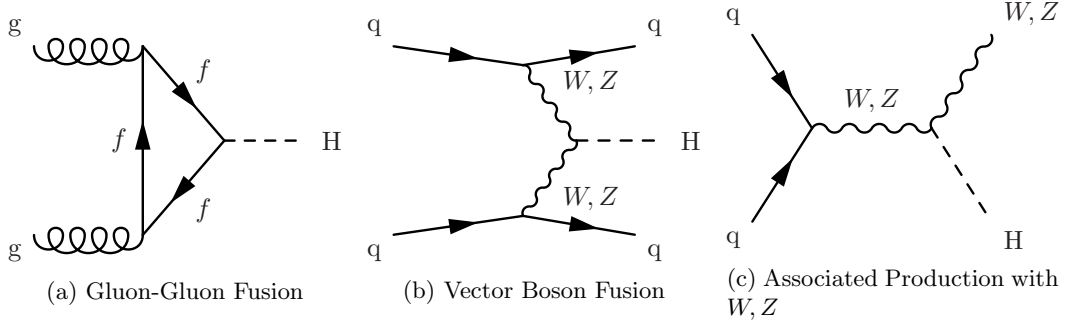


Figure 2.6: Feynman diagrams for the three largest Higgs production modes at the LHC

Gluon-gluon fusion, which proceeds via a heavy quark loop [29], is the dominant production mechanism at the LHC. The QCD radiative corrections to the total cross section have been computed at the next-to-leading order (NLO) and at the next-to-next-to-leading order (NNLO accuracy). The cross section for Higgs production at  $m_H = 125$  GeV and  $\sqrt{s} = 8$  TeV, the cross section is given as:

$$\sigma_{ggF} = 19.27 \pm \text{QCD Scale Unc.}^{+7.2\%}_{-7.8\%} \pm \text{PDF} + \alpha_S \text{ Unc.}^{+7.4\%}_{-6.9\%} \text{ pb}^{-1} \quad (2.81)$$

422 Figure 2.6(a) shows a Feynman diagram for this process. The triangle loop contains all strongly  
423 coupled fermions, which is dominated by the top-quark since the Yukawa coupling to the Higgs  
424 is the largest.

Vector boson fusion proceeds through the fusion of  $W^+W^-$  or  $Z^0Z^0$  gauge bosons [29]. The characteristic signature of the production mode is the associated production of two quarks, typically at a low angle relative to the proton beam. This process has been calculated to NNLO for QCD and NLO for Electroweak corrections [29]. The cross section at  $m_H = 125$  GeV and  $\sqrt{s} = 8$  TeV is given as:

$$\sigma_{VBF} = 1.653 \pm \text{EW Unc.}^{+4.5\%}_{-4.5\%} \pm \text{QCD Scale Unc.}^{+0.2\%}_{-0.2\%} \pm \text{PDF} + \alpha_S \text{ Unc.}^{+2.6\%}_{-2.8\%} \text{ pb}^{-1} \quad (2.82)$$

425 Figure 2.6(b) shows a Feynman diagram for VBF production. The large coupling to the  $W, Z$   
426 bosons helps to make this the sub-dominant production mechanism at the LHC. However, the  
427 gluon content of the proton at TeV energies is much larger than that of the valence quarks, thus  
428 the relative suppression.

The third largest production mechanism for Higgs bosons at the LHC is through associated production with a  $W$  or  $Z$  boson [29]. It has been calculated to NNLO for QCD and NLO for Electroweak corrections. This process is also sometimes referred to as, Higgstrahlung, since it resembles the bremsstrahlung process of an electron radiating a photon. The higher order

electroweak corrections are similar to that of the Drell-Yan, so much of the technology to compute the cross-section can be borrowed from existing EW calculations. The cross section for  $m_H = 125 \text{ GeV}$  and  $\sqrt{s} = 8 \text{ TeV}$  is:

$$\begin{aligned}\sigma_{WH} &= 0.7046 \pm \text{QCD Scale Unc.}^{+1.0\%}_{-1.0\%} \pm \text{PDF} + \alpha_S \text{ Unc.}^{+2.3\%}_{-2.3\%} \text{ pb}^{-1} \\ \sigma_{ZH} &= 0.4153 \pm \text{QCD Scale Unc.}^{+3.1\%}_{-3.1\%} \pm \text{PDF} + \alpha_S \text{ Unc.}^{+2.5\%}_{-2.5\%} \text{ pb}^{-1}\end{aligned}\quad (2.83)$$

<sup>429</sup> Figure 2.6(c) shows the Feynman diagram for VH production. This channel is most useful for  
<sup>430</sup> identifying hadronic decays of the Higgs, since the associated gauge boson can decay to leptons,  
<sup>431</sup> giving a strong kinematic handle over backgrounds that would normally overwhelm a similar  
<sup>432</sup> search in the ggF channel.

## <sup>433</sup> 2.9 $t\bar{t}H$ Production in $pp$ Collisions at the LHC

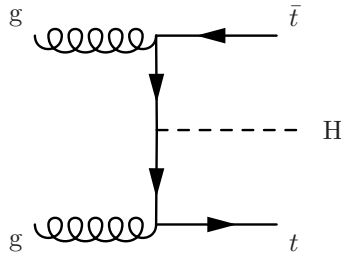


Figure 2.7: Feynman diagram for  $t\bar{t}H$  production

<sup>434</sup> The  $t\bar{t}H$  production mode is the fourth largest production mode at the LHC [29]. This produc-  
<sup>435</sup> tion mode has been calculated to NLO in QCD [30] [31] and has been studied recently with the  
<sup>436</sup> state of the art NLO tools using the aMC@NLO [32] and POWHEG (PYTHIA+HERWIG) [33]  
<sup>437</sup> frameworks. Studies have also been performed interfacing NLO QCD studies [34] with the  
<sup>438</sup> Sherpa parton shower framework [35]. Additional studies on the effects of spin correlations with  
<sup>439</sup> the aMC@NLO and Madspin framework have also been performed [36].

It has been found that the addition of NLO effects increases the cross-section relative to LO by  $\sim 20\%$ . The largest theoretical uncertainty comes from the variation of the renormalization and factorization scale, the QCD coupling  $\alpha_S$ , and the PDF uncertainty. The renormalization and factorization scales are set to  $\mu_R = \mu_F = (1/2)(m_T + m_T + m_H)$  and are varied by a factor of 2 to determine the cross-section's dependence on these parameters. Three different PDF sets, MSTW2008, CTEQ6.6, and NNPDF2.0 were used with the appropriate corresponding values of  $\alpha_S$  to determine the combined effect of varying PDF +  $\alpha_S$ . The cross section for  $m_H = 125 \text{ GeV}$

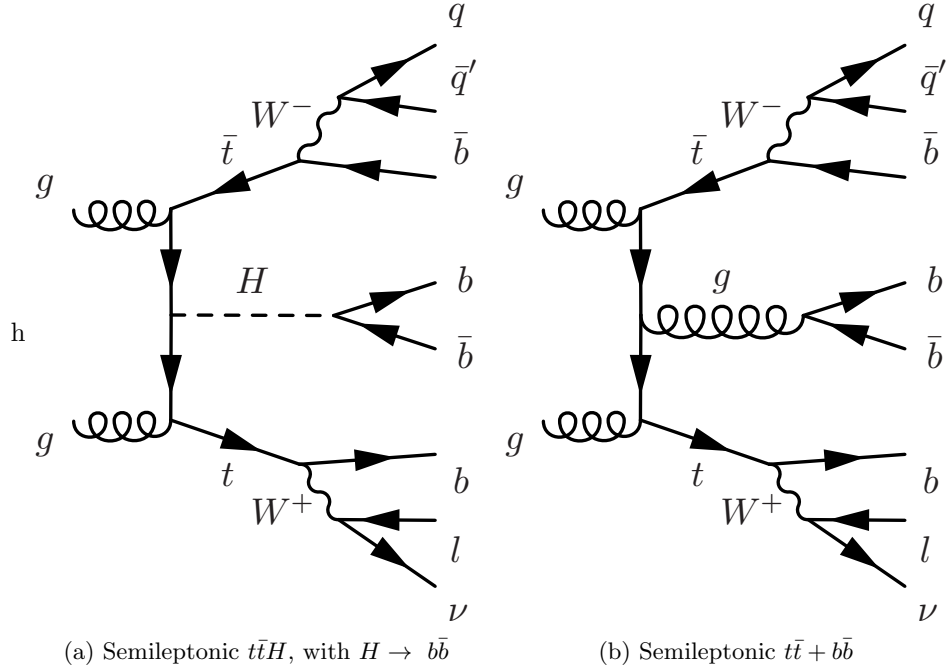


Figure 2.8: Feynman diagrams for the semileptonic  $t\bar{t}H$  process and its irreducible background,  $t\bar{t} + b\bar{b}$

and  $\sqrt{s} = 8$  TeV is given by:

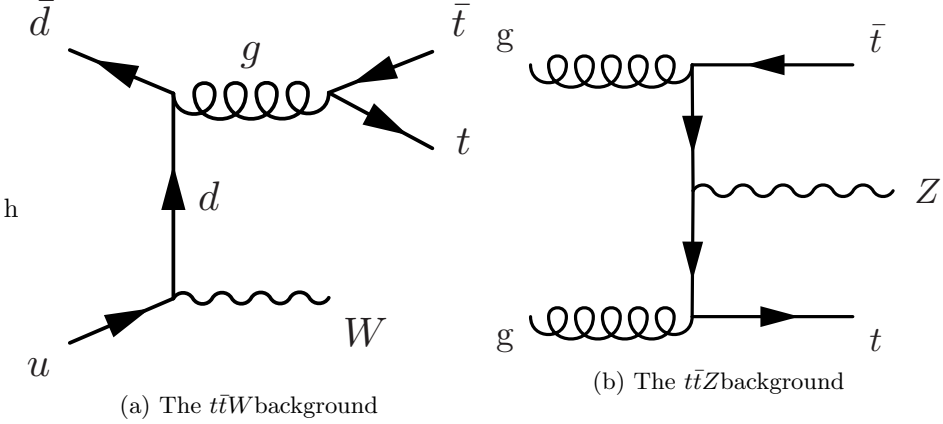
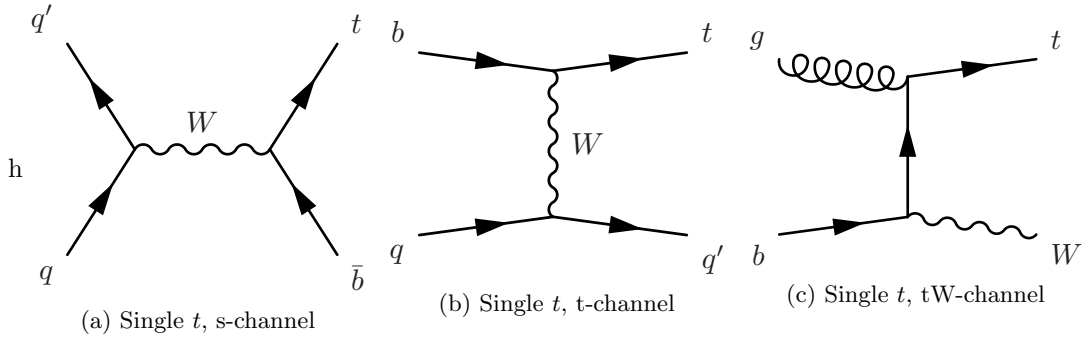
$$\sigma_{ttH} = 0.1293 \pm \text{QCD Scale Unc.}^{+3.8\%}_{-9.3\%} \pm \text{PDF} + \alpha_S \text{ Unc.}^{+8.1\%}_{-8.1\%} \text{ pb}^{-1} \quad (2.84)$$

440 A search for the Higgs in this production mode is additionally challenging due to this large  
441  $\sim 10\%$  error on the theoretical cross-section. Figure 2.7 shows a Feynman diagram for this  
442 process before the branching of the top-quarks or Higgs to final states.

443 When asking for the Higgs to decay to b-quark pairs, yet another complication arises when  
444 trying to identify which b-quarks came from a top decay or from a Higgs decay. For example, in  
445 the semileptonic decay of top quarks, there will be four b-quarks, and two light-flavor quarks in  
446 the final state. This means there are 15 (six choose four) possibilities to associate quarks to the  
447 top system. Although this is potentially constrained by b-tagging, and kinematic requirements  
448 (such as forming the top or  $W$  masses), the number of remaining possibilites smears out the  
449 resolution on peaking variables such as the invariant mass of b-quark pairs.

## 450 2.10 Background Processes to $t\bar{t}H$

451 The dominant background for  $t\bar{t}H$  production of top-quark pairs with additional ISR/FSR jets,  
452  $t\bar{t} + jets$ . The irreducible component of this background is comes when the extra radiation  
453 produces a final state with two additional b-quarks,  $t\bar{t} + b\bar{b}$ . Figure 2.8 compares the Feynman

Figure 2.9: Feynman diagrams for the  $t\bar{t}W$  and  $t\bar{t}Z$  background processesFigure 2.10: Feynman diagrams for the single  $t$  s,t, and  $tW$  background processes

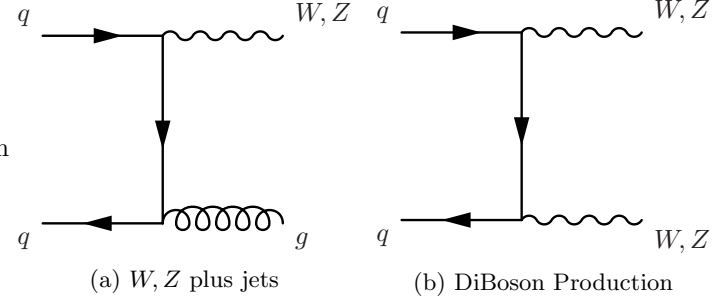
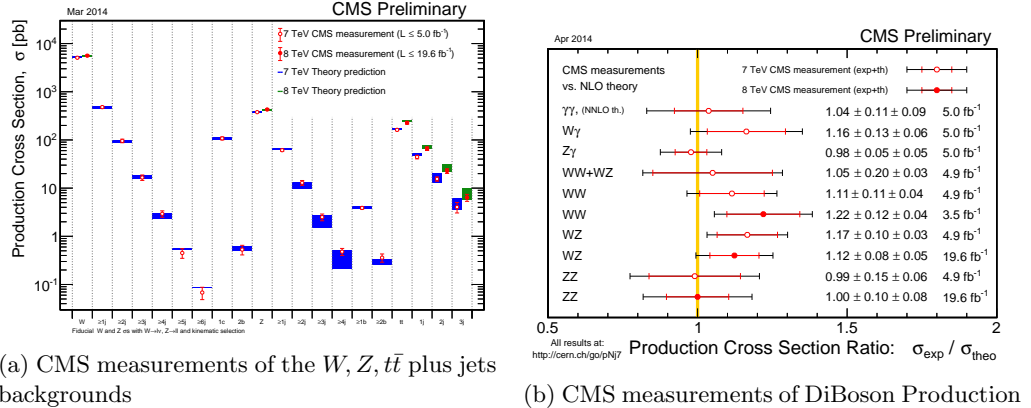
454 diagrams for the semileptonic decays of  $t\bar{t}H$  and  $t\bar{t} + b\bar{b}$ .

455 Additional difficulties come from the theoretical uncertainty on the  $t\bar{t} + b\bar{b}$ background [29].

456 The process has been calculated to NLO QCD in Sherpa [35] and OpenLoops [37] [38] [39]. It  
457 has been found that depending on selection cuts, and use of NLO PDF inputs, the difference  
458 between LO and NLO calculations on the cross section can be anywhere from 0.99% to 1.96%.

459 The light flavor component of the  $t\bar{t} + jets$  background also enters in the selection when any  
460 of the jets from the  $t\bar{t}$  system or extra radiation are misidentified as  $b$ -jets. The cross-section  
461 for the  $t\bar{t} + jets$  process is  $\sim 245 \text{ pb}^{-1}$ . This is a factor of 1800, so even if a  $b$ -tagging algorithm  
462 performs with a 1% mis-identification rate of light-jets, there will still be a large contribution  
463 from this process that will leave a very similar signature in the detector as  $t\bar{t}H$ .

464 The next largest background is the production of vector bosons in association with top-  
465 quark pairs,  $t\bar{t}W$  and  $t\bar{t}Z$ . Figure 2.9 shows Feynman diagrams from these two processes. They  
466 have cross-sections of  $\sigma_{ttW} = 0.249 \text{ pb}^{-1}$  and  $\sigma_{ttZ} = 0.208 \text{ pb}^{-1}$ , which are only a factor of  
467  $\sim 2$  greater than the  $t\bar{t}H$  process. These processes can enter the semileptonic  $t\bar{t}H$  selection by a  
468 semileptonic  $t\bar{t}$  decay, while the vector bosons decay to quarks, or through a hadronic  $t\bar{t}$  decay,  
469 while the vector bosons decay to quarks, and in the case of  $t\bar{t}Z$ , if the leptons is not identified  
470 in the reconstruction.

Figure 2.11: Feynman diagrams for the  $W, Z$  plus jets, and diBoson ( $WW, WZ, ZZ$ ) production.Figure 2.12: Measurements of  $t\bar{t}H$  backgrounds at CMS

Single top production is also an important background to consider in a search for  $t\bar{t}H$  production.

Figure 2.10 shows Feynman diagrams for this process. It does not have as large of a contribution as the other backgrounds, since it requires additional radiation in order to have a similar final state jet multiplicity as  $t\bar{t}H$ . However, since a top-quark is still involved in the process, the final state kinematics of its decay products will be very similar. Single  $t$  production has a cross section of  $\sigma_t = 71.3 \text{ pb}^{-1}$ , while Single  $\bar{t}$  production has a cross section of  $\sigma_{\bar{t}} = 43.6 \text{ pb}^{-1}$ , due to charge asymmetry of the valence quarks of the proton

The last backgrounds to consider are the electroweak production of  $W$  and  $Z$  bosons in association with jets, as well as  $WW$ ,  $WZ$ , and  $ZZ$  pairs in association with jets. Figure ?? shows the Feynman diagrams for these processes, where the  $V$ , stands in for either  $W$  or  $Z$  bosons. For a semileptonic selection of  $t\bar{t}H$  events,  $Z$  plus jets events enter from a misidentification of one of the leptons from the  $Z$  boson decay. Extra FSR/ISR radiation is also to leave a similar signature in the signal region of a  $t\bar{t}H$  search, so it mainly contributes to control regions of the data.

All of these backgrounds have been measured at CMS. With the exception of a small degree of tension in the  $WW$  cross-section measurement, all backgrounds are in good agreement with Standard Model predictions. Figure 2.12(a) shows the results of CMS measurements on  $V+jets$  and  $t\bar{t} + jets$  backgrounds. Figure 2.12(b) shows the same, but for diBoson production.

## 489 2.11 Potential BSM Effects on $t\bar{t}H$ production

490 The phenomenological motivation for the existence of physics beyond the Standard Model come  
 491 from the observation of phenomenon or states of matter not described by the theory. Observations  
 492 of the cosmic microwave background from the Plank telescope have estimated that only  
 493  $\sim 5\%$  of the observable universe is composed of ordinary matter [40]. The remaining composition  
 494 is divided between Dark Matter ( $\sim 27\%$ , and  $\sim 68\%$  respectively). Evidence for Dark Matter  
 495 also comes from discrepancies between the observed rotational velocities of galaxies, and the  
 496 observed mass distributions, suggesting the presence of additional form of matter which does  
 497 not interact electromagnetically [41].

498 Additionally, in 1998, the Super-Kamiokande experiment proved that neutrinos oscillated  
 499 between flavors, implying indirectly that they also have mass [42]. This is something not de-  
 500 scribed in the Standard Model of physics. Due to their neutral charge, these particles are  
 501 extremely difficult to detect, so experiments have only been able to measure differences in the  
 502 mass squared between the three mass eigenstates. In 2005, the KamLAND experiment reported  
 503  $|\Delta m_{12}^2 = 0.000079 eV^2|$  [43]. In 2006, the MINOS experiment reported  $|\Delta m_{23} = 0.0027 eV^2|$  [44].

504 One of the largest theoretical problems with the Standard Model, comes the mechanism which  
 505 made it all possible- the Higgs. In equation 2.73 there are terms that couple the Higgs boson  
 506 to itself,  $-\lambda vh^3$ , and  $-\frac{1}{4}\lambda h^4$ . When computing NLO effects, these terms lead to a divergence  
 507 in the Higgs mass, when considering the effect of a loop of fermions on the Higgs propagator.  
 508 The corrections are of the form  $\Delta m_H = -\frac{\lambda_f^2}{8\pi^2} \Lambda_{UV}$ . Where  $\Lambda_{UV}$  is the high energy cut off for the  
 509 theory, which in the limit of a perfect theory, should extend to infinity. This is known as the  
 510 hierarchy problem.

511 Beyond the Standard Model physics is a term that describes extensions of the Standard  
 512 Model in order to describe the observed phenomenon. For the neutrino oscillations, a solution  
 513 similar to CKM matrix has been proposed, the PontecorvoMakiNakagawaSakata (PMNS) ma-  
 514 trix. This proposes that the mass eigenstates of the neutrino are linear combinations of the weak  
 515 eigenstates, allowing for the mixing of flavors. Current experiments now seek to measure the  
 516 free parameters of this matrix.

517 Both the dark matter and hierarchy problems suffer in the fact that there is no clear model,  
 518 such as the PMNS matrix, to provide a theoretical solution. Out of the plethora of theories that  
 519 attempt to solve these problems, supersymmetry (SUSY) is the most popular in the theoretical  
 520 and experimental community. It suggests that there is a broken symmetry between fermions  
 521 and bosons, and introduces a partner to each Standard Model particle with a spin quantum  
 522 number less 1/2 [45]. For the hierarchy problem, this provides a set of particles to cancel out the

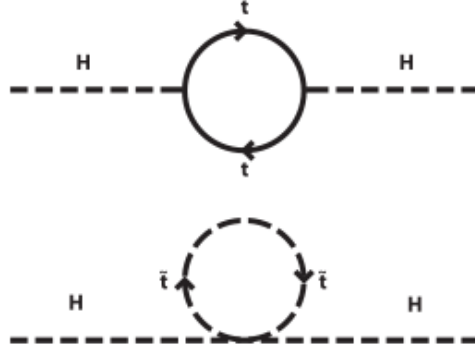


Figure 2.13: The cancellation of the divergent Higgs mass from a loop of top-quarks is cancelled by a loop of supersymmetric top-quarks, stop-quarks,

523 divergences in the NLO corrections to the Higgs mass. Figure 2.13 shows the Feynmann diagrams  
 524 for a supersymmetric top-quark, or stop quark, that would cancel the divergent contribution from  
 525 the Standard Model top quark. Depending on the specific form of the SUSY model, the stop  
 526 quarks can potentially couple directly or indirectly to the top-quark, producing them at a higer  
 527 rate during  $pp$  collisions. This would effect the number of observed events making it into the  
 528  $t\bar{t}H$  selection.

529 A number of extensions to the SM also involve introducing new top-like particles into the  
 530 theory. Vector-like quarks would be spin 1/2 particles that transform as triplets under the  $SU(3)$   
 531 color group and whose left and right-handed components have the same color and electroweak  
 532 quantum numbers [46]. These objects are common to several different types of models. Little  
 533 Higgs models [47] [48] [49], models with extra dimensions [50] [51], top-color models [52], and  
 534 composite Higgs models [53], include a vector-like top partner,  $t'$  that decays to a top-quark and  
 535 either a Higgs,  $W$ , or  $Z$  particle. Both  $t't'$  pair production and  $t't$  production would yield the  $t\bar{t}H$   
 536 final state, or at least one indistinguishable detector signature.  $t\bar{t}H$  search can provide indirect  
 537 limits on these models, by observing an excess or lack thereof of  $t\bar{t}H$  events, without having to  
 538 directly construct a  $t'$  resonance.

539 **Chapter 3**

540 **The Large Hadron Collider**



Figure 3.1: Aerial view of the LHC complex, spanning the French-Swiss border [1]

541 The Large Hadron Collider (LHC), is a superconducting, proton-proton, accelerator and  
542 collider operated by the European Center for Nuclear Research (CERN) laboratory in Geneva,  
543 Switzerland [54]. Figure 3.1 shows an aerial view of the LHC complex, with the main laboratory  
544 campus being labeled as CERN, with four of the detector experiments being labeled as ALICE,  
545 ATLAS, CMS, and LHCb. Three smaller experiments, not pictured, also use the LHC ring, and  
546 are TOTEM, LHCf, and MOeDAL. It was designed to elucidate the mechanism of electroweak  
547 symmetry breaking and explore TeV scale of particle physics. As such, it is required to produce  
548 a large number of high center-of-mass energy events. The high center-of-mass energy allows the  
549 creation of heavy particles, while a large luminosity allows for the creation of rare processes.  
550 The number of events produced at a collider is a product of the luminosity of the collider and

551 the total cross-section for the objects being collided.

$$N_{events} = L\sigma_{event} \quad (3.1)$$

552 The cross-section,  $\sigma_{event}$ , can be estimated from the theory of the Standard Model as described  
 553 in section 2.1 and validated by measurement at detectors, such as CMS, as shown in section 2.10.  
 554 The luminosity is a control of the experiment, and for Gaussian distributed beams, is given by  
 555 the equation:

$$L = \frac{N_b^2 n_b f_{rev} \gamma_r}{4\pi \epsilon_n \beta^*} F \quad (3.2)$$

556 The parameters of this equation and their value for the LHC is as follows:

- 557 •  $N_b$  - Number of particles per bunch, squared since there are two beams. The mechanism  
 558 of achieving such high energies is based in Radio-Frequency (RF) cavity technology, which  
 559 clusters the protons together into packets, which are all accelerated and collided together.  
 560 For the LHC,  $N_b = 1.15 \times 10^{11}$ .
  - 561 •  $n_b$  - Number of bunches per beam. The maximum design for the LHC allows for  $n_b = 2808$   
 562 bunches, however in practice, lower number of bunches have been run with in order to  
 563 create more time between bunch crossings.
  - 564 •  $f_{rev}$  - Revolution frequency of the protons in the LHC ring. This is determined by ring  
 565 circumference, and for the LHC,  $f_{rev} = 11.2$  kHz.
  - 566 •  $\gamma_r$  - This is the relativistic gamma-factor, determined by the speed, and thus the center of  
 567 mass energy of the collisions.
  - 568 •  $\epsilon_n$  - This is the normalized transverse emittance of the beam, which describes the RMS  
 569 spread of the beam in its transverse plane. For the LHC  $\epsilon_n = 3.75 \mu\text{m}$ .
  - 570 •  $\beta^*$  - Is the minimum of the  $\beta$  function, which is defined as the square of the transverse  
 571 beamsize divided by  $\epsilon_n$ . It is minimized at interaction regions, where the beams are being  
 572 squeezed into the smallest region possible, to maximize the probability of protons colliding  
 573 during each bunch crossing. For the LHC,  $\beta^* = 0.55$
  - 574 •  $F$  - This is the efficiency for having the two beams head-on, and is determined by the  
 575 crossing angle at which the two counter-rotating beams meet each other.
- 576 The LHC is designed to deliver a maximum luminosity of  $L = 10^{34} \text{ cm}^{-2}\text{s}^{-1}$  to the CMS and ATLAS  
 577 experiments, with a maximum center-of-mass energy of  $\sqrt{s} = 14$  TeV.

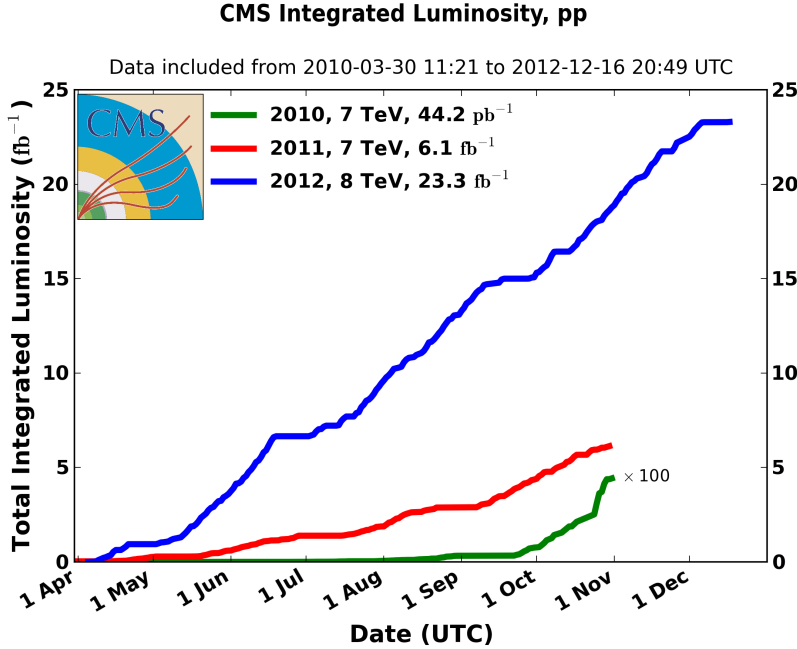


Figure 3.2: Integrated Luminosity delivered to the CMS experiment from 2010-12

578 In 2010-11, the LHC ran at center-of-mass energy,  $\sqrt{s} = 7 \text{ TeV}$  and delivered  $\sim 6 \text{ fb}^{-1}$  of  
 579 data to the CMS experiment. In 2012, it ran at  $\sqrt{s} = 8 \text{ TeV}$  and collected  $\sim 23 \text{ fb}^{-1}$ . Figure 3.2  
 580 shows a diagram of the luminosity collected as a function of time for each year running.

581 The next sections will describe the LHC accelerator complex, the chain of events leading  
 582 up to collisions of protons at the LHC, and the associated technologies that allow for the con-  
 583 trol and operation of the high-energy, high-luminosity beams that allow the CMS and ATLAS  
 584 experiments to search for heavy particles and rare-processes.

### 585 3.1 The LHC Accelerator Complex

586 The main LHC ring is a 26.7 km tunnel, that is 45 m to 170 m underneath the surface of the  
 587 earth, with 1.4% slope towards Lake Leman. It extends accross the French-Swiss border, into  
 588 the French coutnryside. The tunnel was originally constructed between 1984 and 1989 for the  
 589 Large Electron Positron (LEP) experiment that is famous for it's precision mesaurements of  
 590 several Standard Model parameters [54]. The choice to build the ring underground was driven  
 591 by real estate costs, but the underground setting also provides natural radiation shielding from  
 592 the beamline and greatly reduces the impact of cosmic radiation on the detectors.

593 The LHC also utilizes the existing accelerator complex from the LEP experiment, which is  
 594 shown in figure 3.3. The complex is composed a series of increasingly powerful accelerators that  
 595 gradually increase the energy of the protons.

596 Protons are initially accelerated by the Linac2 linear accelerator up to 50 MeV [55] [56]. A

## The LHC injection complex

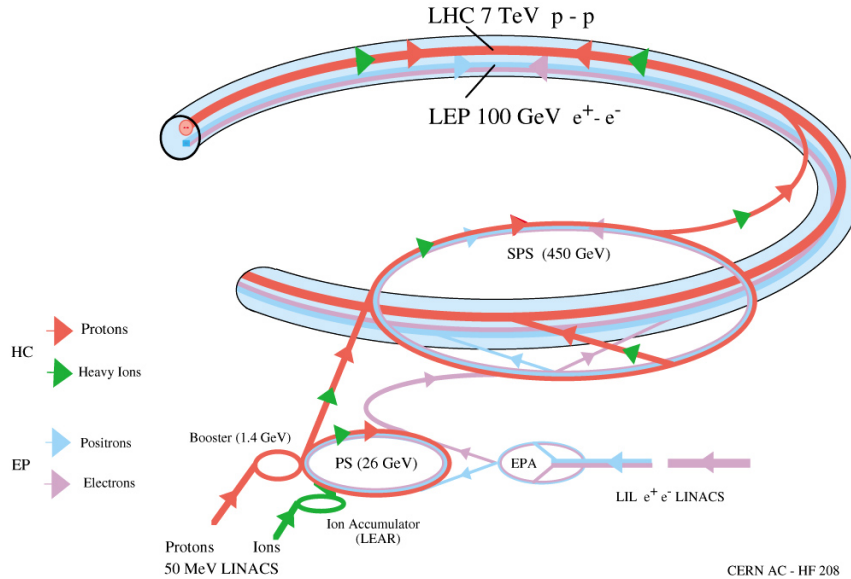


Figure 3.3: The LHC accelerator complex, taking protons from a bottle of Hydrogen at the Linac2, all the way to the LHC ring

bottle of Hydrogen is attached to a duoplasmatron source. This device ionizes the Hydrogen, and creates a 300 mA beam of protons, through a high-voltage anode, and a geometry designed to focus and collimate the beam as it leaves the device. Figure 3.4(a) shows a schematic for this device, showing the gas input on the left, and proton beam leaving to the right. Figure 3.4(b) shows the actual device used in the Linac2 at CERN. The proton beam then enters the Radio-Frequency Quadropole (RFQ) system, which accelerates and bunches the protons up to 750 keV. The RFQ is a waveguide with four flanges, which have been machined with a sinusoidal modulation in the longitudinal direction, which creates an standing electric wave in this direction, accelerating the protons. Figure 3.4(c) shows a schematic of this modulation, and figure 3.4(d) is a close-up image of this modulation in an actual RFQ. The last stage of acceleration is provided by three Alvarez tanks. Each Alvarez tank holds a series of elctrically isolated cylinders, known as drift tubes, coaxial with the main tank, with gaps in between them. An alternating electric field is present in the gaps, and space between each drift tube and the walls of the tank. Protons passing through the center of the drift tubes feel no electric field, but the gaps are located such that, a proton will always see an accelerating field in the gap, and are thus receive a boost of energy from each gap as it traverses the length of the three tanks. Figure 3.4(e) shows an image of the inside of an Alvaez tank, and figure 3.4(f) shows the tanks at the Linac2 at CERN. The final product is a 180 mA, 50 MeV proton beam, which is steered to the Proton Synchotron Booster for the next stage of acceleration.

The Proton Synchotron Booster (PS booster) complex accelerates the protons up to 1.4

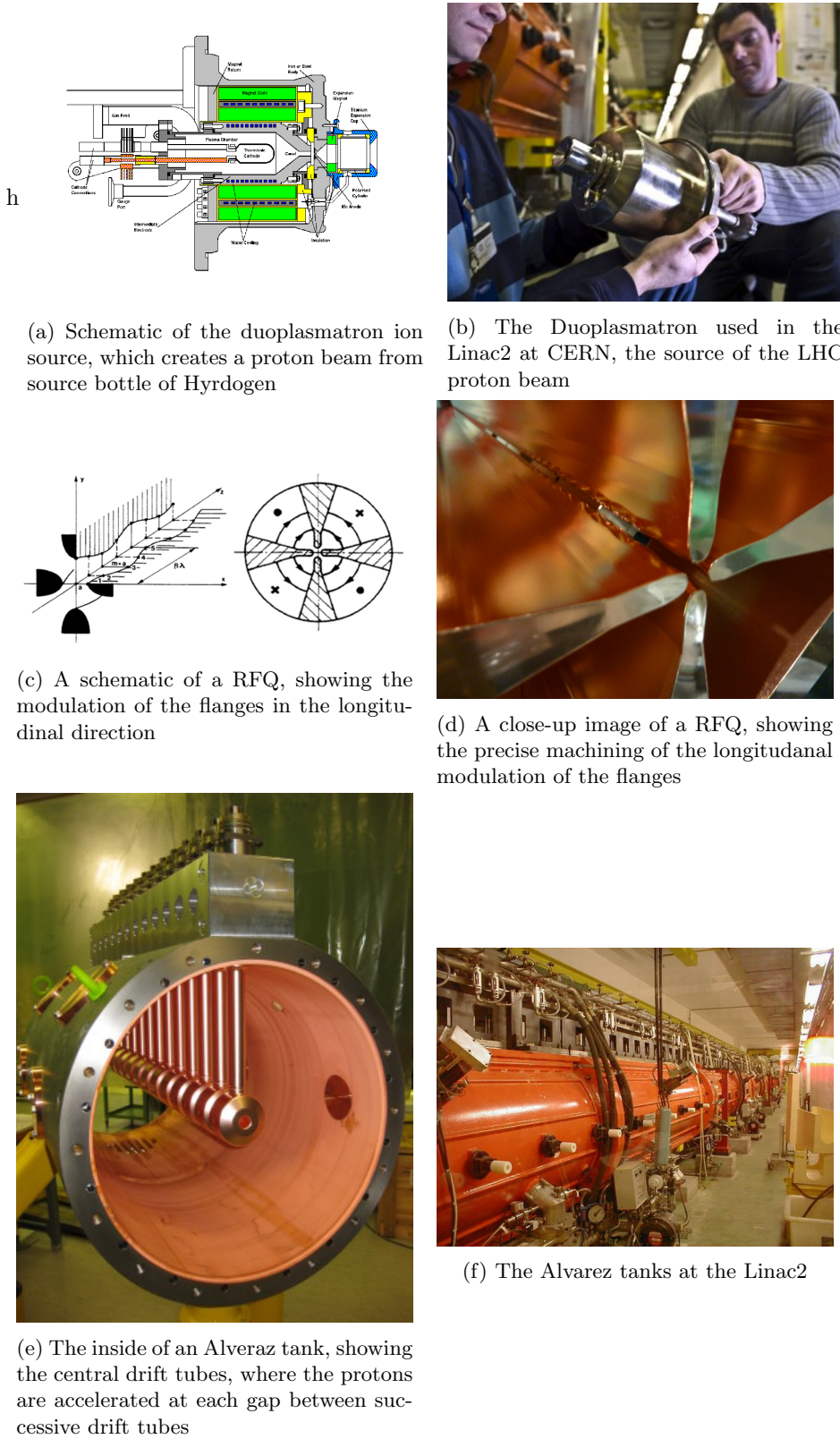


Figure 3.4: Features of the Linac2, the first stage of acceleration in the LHC injection chain

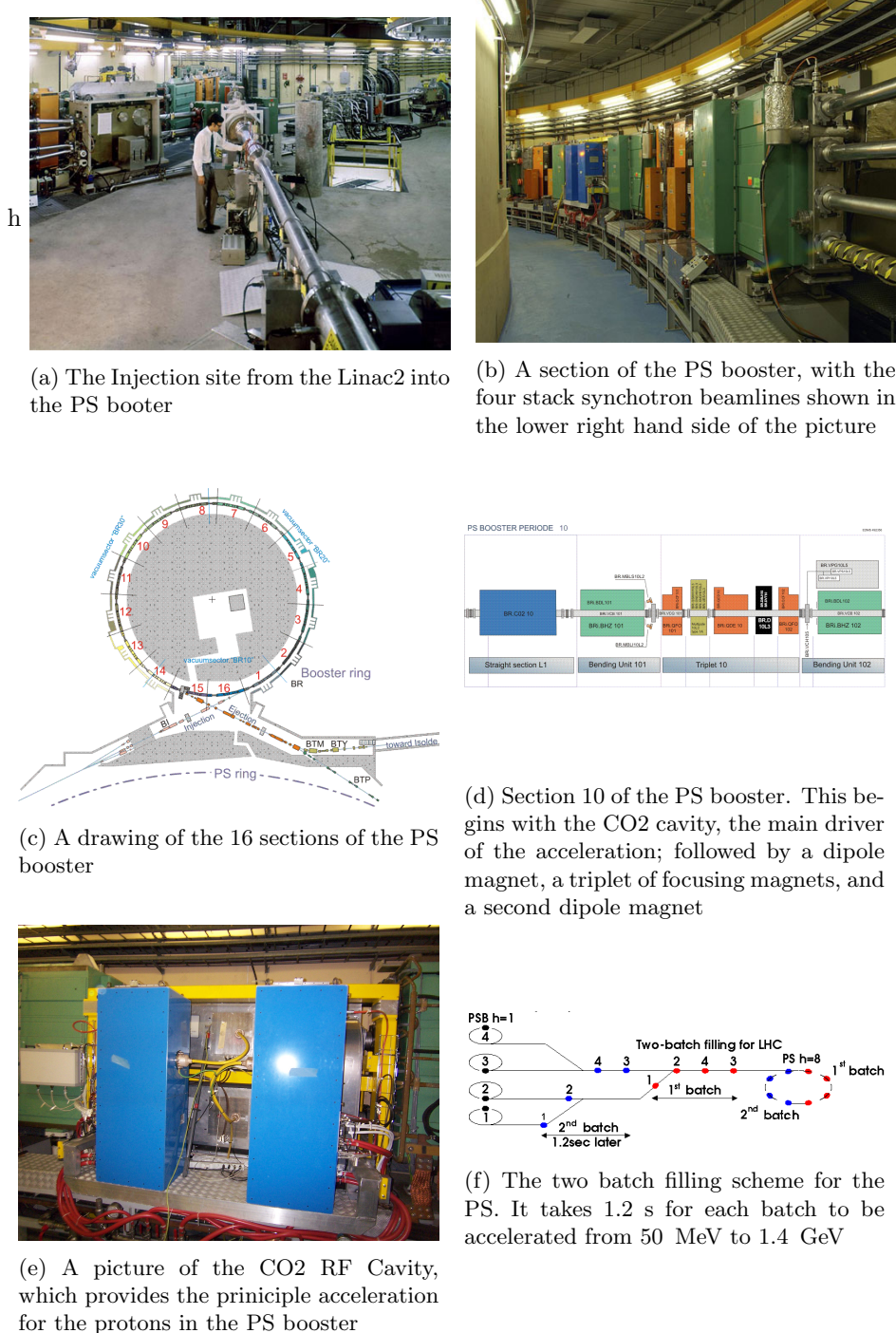


Figure 3.5: Features of the PS booster, the second stage of the LHC injection chain

617 GeV [55]. The complex takes the proton beam from the Linac2 and splits the beam into four  
 618 separate, synchrotrons, stacked on top of one another. Figure 3.5(a) shows the injection site of  
 619 the proton beam from the Linac2 into the PS booster. The right side of figure 3.5(b) shows the  
 620 four synchotron beam pipes stacked vertically on top one another. The splitting of the beam is  
 621 done in order to reduce the effect of the space charge of the proton beam, which would increase  
 622 the transverse emmitance beyond a tolerable degree. The PS booster uses thirty-two 0.87 T  
 623 dipole magnets to bend the beams, and fourty-eight quadrupoles to focus the beam as it makes  
 624 its way around each of the 50 m diameter rings. Each magnet is composed of a vertical stack  
 625 of four magnets, one for each of the synchotrons, and share a common yoke, allowing one power  
 626 supply to provide the current to all of them in series [57]. The booster is divided into 16 arcs, as  
 627 shown in figure 3.5(c). Each arc contains a bending dipole, 3 focusing quadrupoles, and a second  
 628 bending dipole, followed by a straight section containing beam diagnostic, injection and ejection  
 629 systems, and in three sections, the Radio-Frequency (RF) cavities, which is the mechanism of  
 630 accelerating the beam [58]. Figure 3.5(d) shows the layout of the tenth arc, which also contains  
 631 one of the RF cavities in the first section.

632 An RF cavity is a specially shaped, hollow conductor, that the beam passes through [59].  
 633 The shape of the cavity determines the resonant frequency and harmonics (integer multiples of  
 634 the fundamental frequency), of the standing electromagnetic fields that result when the cavity  
 635 is driven by an alternating voltage source. The idea is to choose a resonant frequency such  
 636 that the proton will always experience a positive electric field, and thus an acceleration, each  
 637 time it passes through the RF cavity. This means that the revolution frequency of the proton  
 638 must be equal to the fundamental frequency or harmonic of the RF cavity,  $f_{RF} = n \times f_{rev}$ , with  
 639  $n = 1, 2, 3, \dots$ . Eventually, the proton is accelerated up to an equilibrium speed and will enter the  
 640 cavity just as the standing electric field is alternating through it's zero point. If arrives too early  
 641 for this (moving too fast), then it will experience a negative electric force, a deceleration, which  
 642 will eventually bring it back to the equilibrium revolution frequency, where it experiences zero  
 643 net force. A diffuse beam of protons will be bunched into groups of protons through this effect  
 644 as well, as the faster protons in the beams are decelerated, and the slower ones accelerated,  
 645 until they all reach the same equilibrium revolution frequency. Driving the RF cavity with a  
 646 harmonic,  $n$ , of the proton's revolution speed will thus create  $n$  bunches of protons. Each one of  
 647 the potential  $n$  bunch positions is referred to as a bucket. In the case where a proton has to be  
 648 accelerated through a wide range of energies, the frequency of the cavity must also increase to  
 649 maintain synchronization with the proton revolution frequency.

650 Three types of RF cavities are used to accelerate the beam during each revolution. The first  
 651 of the three types of RF cavities is the CO<sub>2</sub>, with frequency range of 0.6 to 2.0 MHz and is used

652 to drive the  $h = 1$  harmonic of the synchrotron, and is pictured in figure 3.5(e). The second  
 653 type of cavity is the CO4 chamber, with a frequency range of 1.2 to 3.9 MHz, and drives the  
 654  $h = 2$  mode of the synchrotron. This second mode is capable of splitting the beam and creating  
 655 two separate bunch structures. However, for LHC running, only one bunch is used, and is driven  
 656 primarily by the  $h = 1$  mode. The  $h = 2$  mode is supplemental and is used to shape the beam.  
 657 A third type of RF cavity, CO16, has a frequency range of 5 to 16 MHz, and is used to control  
 658 the longitudinal shape of a bunch during acceleration. The beam leaves the PS booster and enters  
 659 the PS in a two-batch filling scheme, taking only 1.2 s to accelerate a second batch of protons  
 660 from 50 MeV to 1.4 GeV. This second batch enters just as the first batch has traveled to the  
 661 opposite side of the PS ring. A schematic of this process is shown in figure 3.5(f). To achieve  
 662 the 25 ns bunch spacing design of the LHC, only 6 bunches of proton beam need to be delivered  
 663 to PS. This is achieved by either using a 4+2 or 3+3 filling scheme, in terms of the number of  
 664 proton bunches derived from the four possible synchotrons.

665 The next stage is the Proton Synchrotron (PS), which will boost the protons up to 25  
 666 GeV [55]. The layout is shown in figure 3.6(a). The ring has a circumference of 628 m, and  
 667 uses 100 dipole magnets and 177 higher-order focusing magnets, to steer the beam around the  
 668 ring. Figure 3.6(b) shows a picture of one of the dipole magnets used at the PS. In addition  
 669 to providing acceleration up to 25 GeV, the PS forms the basis of the bunch structure that is  
 670 eventually used in the LHC. The  $h = 7$  harmonic is used to capture the 6 bunches of protons  
 671 delivered from the PS booster, leaving a gap in the place of a seventh bunch. The beam is then  
 672 split into three, by using three different RF cavities tuned to the  $h = 7, 14, 21$  modes of the PS.  
 673 Figure 3.6(c) shows a simulation of a proton bunch being divided into three over the course of  
 674 25 ms. The  $h = 21$  mode is then used to accelerate the protons to from 1.4 to 25 GeV using the  
 675 20 MHz RF cavity. Each bunch is then split twice, using the  $h = 21, 42, 84$  synchroton modes,  
 676 to create 72 bunches, spaced 25 ns apart, with a 320 ns gap for the 12 unused buckets of the  
 677  $h = 84$  harmonic. This process is simulated in figure 3.6(d), over the course of 125 ms. The 320  
 678 ns gap is created to account for the rise time of the kicker magnet, which ejects the beam out of  
 679 the PS into the SPS. The entire splitting process is summarized in figure 3.6(e). For the case of  
 680 50 ns bunch spacing, the final stage of splitting is not performed, and the  $h = 21, 42$  modes are  
 681 used to split the beam. Finally, in order to fit the bunches into the 200 MHz RF acceleration  
 682 scheme of the SPS, the bunch length must be compressed from 11 ns to 4 ns. This is achieved  
 683 by rotating the beam in the energy vs time phase space by sequential increases in voltage to  
 684 the 40 MHz  $h = 84$  mode, followed by an increase to the 80 MHz  $h = 168$  mode. Figure 3.6(f)  
 685 shows the result of this rotation - a distortion free ellipse with a smaller 4 ns spread, but a larger  
 686 spread in the energy spectrum of the proton beam.

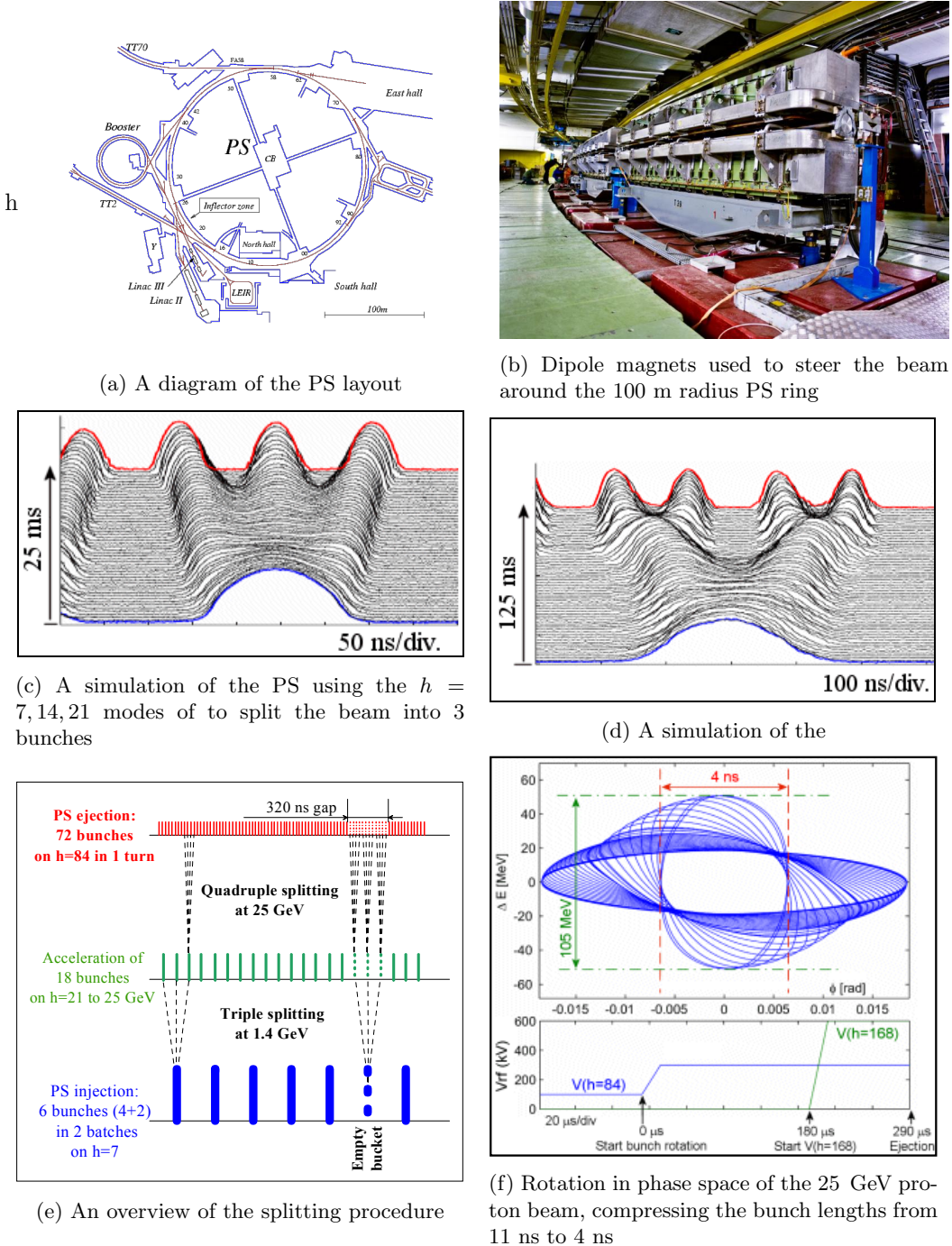


Figure 3.6: Features of the PS, the third stage of the LHC injection chain

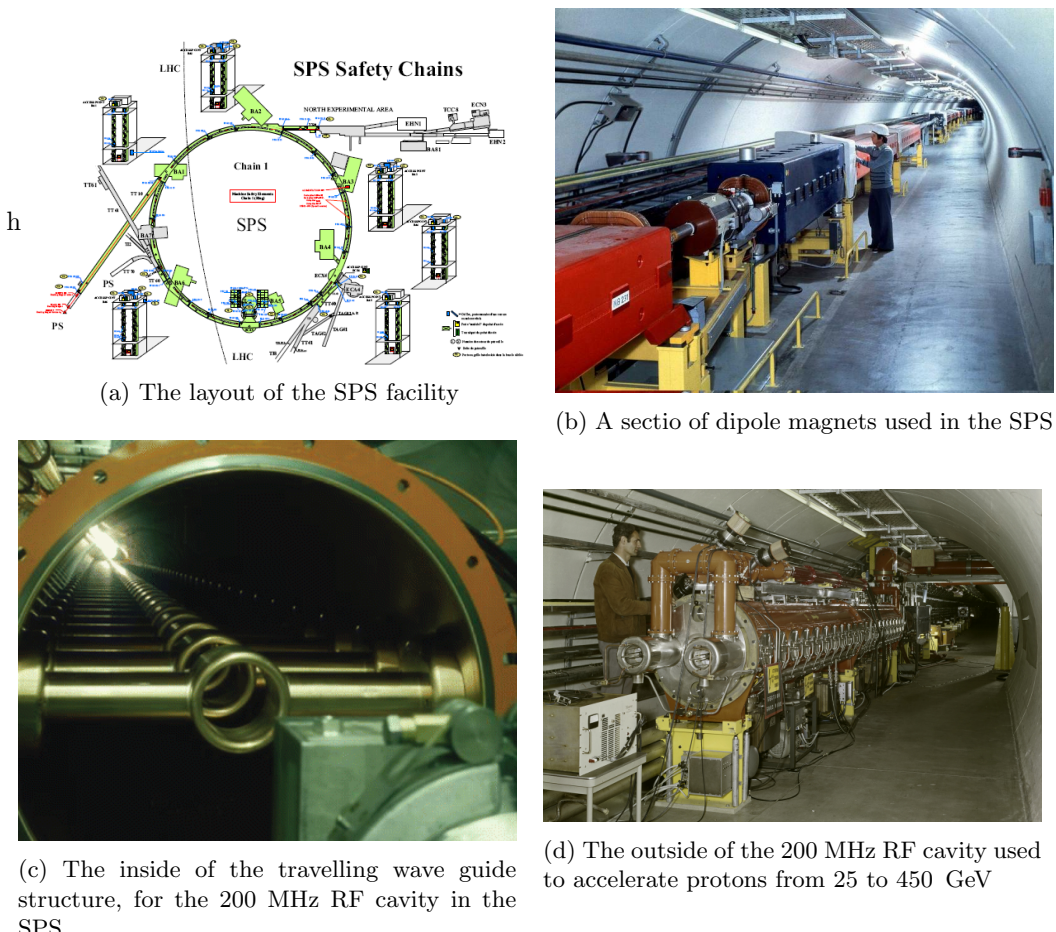


Figure 3.7: Features of the SPS, the fourth and final stage of the LHC injection chain

687 Next, the protons arrive at the Super Proton Synchotron (SPS), where they will be acceler-  
 688 erated to 450 GeV. The SPS is the last stage of acceleration before the protons are injected  
 689 into the LHC. The layout is show in figure 3.7(a). It has a circumference of 7 km, and steers  
 690 the proton beam with 744 dipole magnets, with 573 higher-order focusing magnets [60]. Figure  
 691 3.7(b) shows one of the dipole mangets in the SPS tunnel. Like all the other synchrotrons in  
 692 the injection chain, the acceleration is provided by RF cavities. A 200 MHz system of RF cavi-  
 693 ties capture and fill the SPS by using 2-4 batches of 72 bunch proton beams from the PS [55].  
 694 Although the relative change in frequency is small, the large degree of acceleration necessitates  
 695 the use of a tunable RF cavity. The 200 MHz system has 2 sections of 4 travelling wave cavities  
 696 in series, and another 2 sections of 5 cavities in series. Figure 3.7(c) shows the insde of this  
 697 structure, which uses drift tubes to accelerate protons in the gaps between tubes, with horzion-  
 698 tally mounted bars, spaced 374 mm [61] apart, determining the periodicity of the resonant RF  
 699 field that builds up inside. The outside of the structure is shown in figure 3.7(d). An additional  
 700 800 MHz system is used to control the transverse emmitance. It is also used to stabalize the  
 701 beam-line and prevent coupled-bunch instabilities [55].

702 Finally, protons are injected into the LHC ring in one clockwise, and another counter-  
 703 clockwise rotating beams. In order to work in the limited space of the existing LEP tunnel,  
 704 the two beams are contained within a single meachanical and cryostate structure, with a dual-  
 705 bore design for each of the beams. Here, each proton beam is accelerated to their final energy of  
 706 7 TeV, moving at 99.999991% the speed of light, before they meet head on, producing 14 TeV  
 707 center-of-mass collisions.

708 The LHC ring itslef is divided into eight octants, with eight straight sections that are located  
 709 in front and behind each of the eight collision points, where the beams are made to cross and  
 710 collide, as shown in figure 3.8. These crossings are known as interaction regions (IRs). Four  
 711 of these points are currently being used by experiments. TOTEM has detectors on either side  
 712 of the CMS experiment at one interaction region, known as point 5 (P5). LHCf has detectors  
 713 on either side of ATLAS at point 1 (P1). MOeDAL has detectors near LHCb at point 8 (P8)  
 714 and the ALICE detector is located at point 2 (P2). The following sections will cover the RF,  
 715 magnet, cryogen, and vaccuum technologies used in the LHC ring.

## 716 3.2 LHC Magnets

717 Several types of magnets are used in order to properly circulate and focus the proton beam as  
 718 it makes its way around the 26.7 km long tunnel. A complete list of all types, can be found in  
 719 the technical design report [62], as well as through CERN's outreach web resources [63]. This

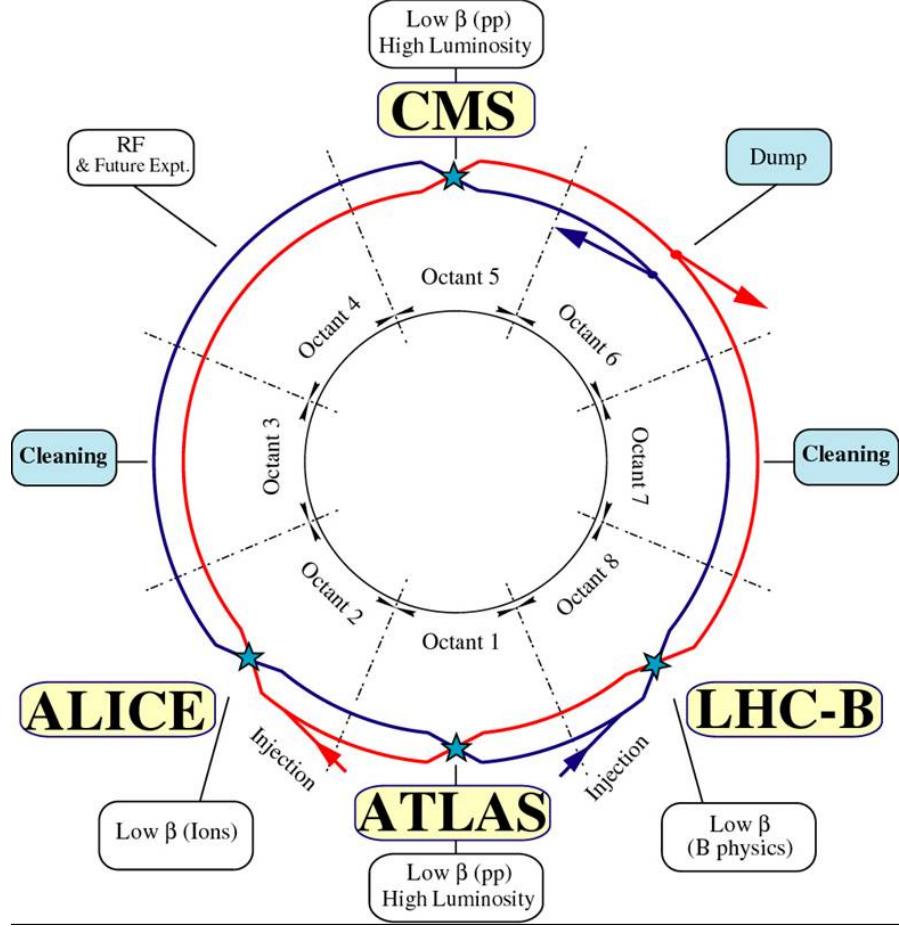


Figure 3.8: The LHC ring is divided into eight octants

section will give an overview of the a few of the critical subsystems: the septum and kicker magnets used for injection from the SPS, the dipole magnets used for bending the beam around the circumference of the ring, and the higher-order-pole magnets that are used for focusing the beam.

The injection and extraction of proton beams from one synchrotron to another involves three types of magnets, septums, kickers, and bumpers. Septum magnets contain a partition, or a septum, that provides a boundary between a high magnetic field region and a near-zero magnetic field region and are operated in DC or a slow-pulsed mode [64]. In case of injecting a beam of protons into a synchrotron, the target beampipe of the synchrotron passes through the low-field region, so the trajectory is unaffected by the high-field region, which bends the injection beam towards the synchrotron aligning it horizontally, with the target beam. The kicker magnet, is a fast-pulsed magnet and provides the timing selection in order to make a final bend vertical bend into the synchrotron orbit, and into the correct basket of the synchrotron bunch train [65]. Finally, bumper magnets make small bends to the beam and align it with the injection site. Figure 3.9 shows a schematic for this process, where a transfer line brings protons to a septum, which bends the beam to a kicker, which makes the final corrections to match the synchrotron

## Single-turn injection

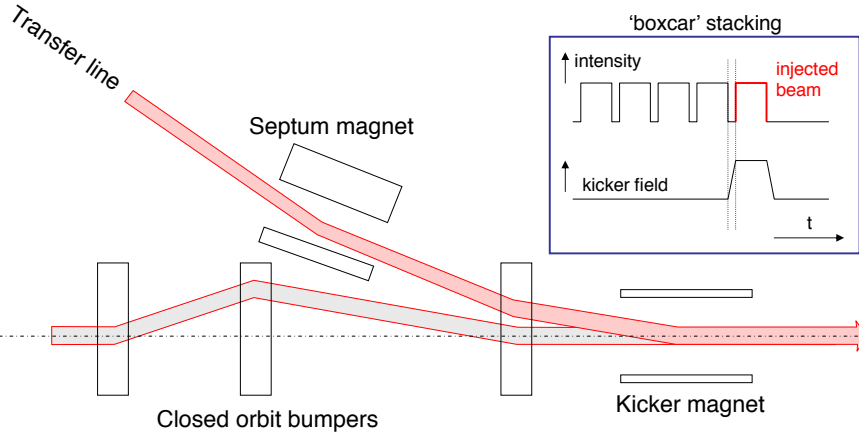


Figure 3.9: The single turn injection scheme. A septum magnet makes the initial alignment. The kicker magnet times the injection and makes the final alignment. Bumper magnets align the LHC beam with the injected beam.

736 orbit. For extraction, the kicker magnet quickly displaces a portion of the beam, which is steered  
 737 away by the septum, while the original beam passes through its low-field region unaffected.

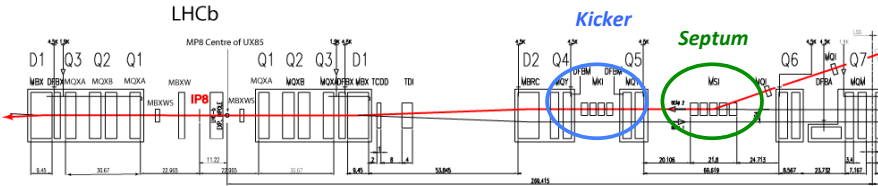


Figure 3.10: Layout of Interaction Region 8, where one proton beam is injected into the LHC ring. A transfer line from the SPS brings a proton in from the right. In green, a septum magnet aligns the beam horizontally with the LHC. In blue, a kicker magnet makes the final vertical alignment into the LHC, and is timed to fill one of the 400 MHz buckets of the RF capture system

738 At the LHC, beam is injected at Interaction Regions (IR) 2 and 8 [54]. Two transfer lines  
 739 bring the beam extracted from the SPS to  $\sim 150$  m of the LHC ring. Five Labertson-type septum  
 740 magnets, of field strength  $\sim 1$  T, are used to deflect each of the transfer line beams 12 mrad  
 741 to align the transfer beam horizontally with the LHC orbit. Then, four  $\sim 0.12$  T MKI kicker  
 742 magnets quickly deflect the beam 0.85 mrad to close the orbit with the LHC ring. Figure 3.10  
 743 shows the layout of the injection point at IR 8. The green circle encloses the septum structure,  
 744 which provides the horizontal alignment, and the blue encloses the kicker structure, which makes  
 745 the final vertical alignment and synchronizes the injection of the beam into the LHC. The rise  
 746 time for the field provided by the kicker magnets in the LHC and SPS determine the final bunch  
 747 structure of the LHC. Figure 3.11 extends figure 3.6(e) showing how the rise times of the kickers  
 748 that inject, or eject beam create gaps in the bunch structure of the LHC. The initial filling of the  
 749 PS with 6 batches of protons from the PSB, leaves one initial bucket unused in the PS. After

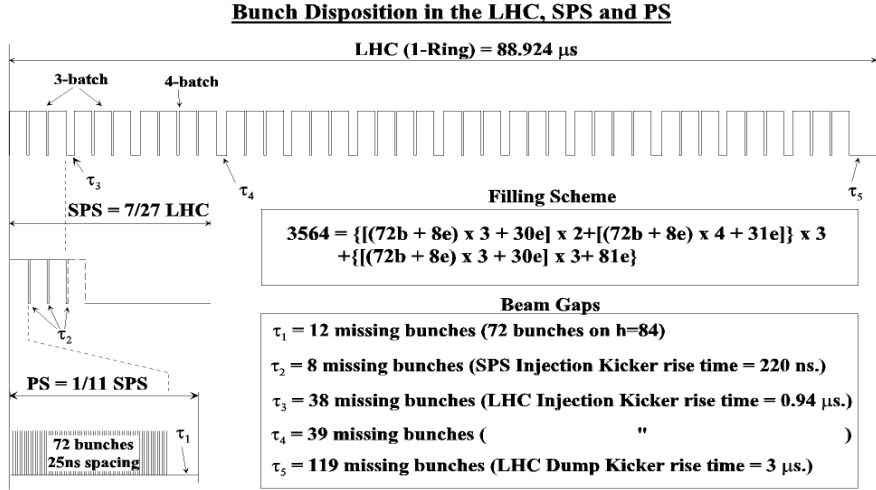


Figure 3.11: The initial filling of 6 batches of protons from the PSB to the PS, leaves 12 empty buckets in the PS bunch structure. The rise time of the SPS magnet creates an additional gap in the SPS bunch structure. Additional gaps emerge due to the rise time of the LHC injection and dumping kicker magnets

750 the splitting of the beam into the 25 ns bunches, there 12 empty buckets at the of the PS bunch  
 751 train. The SPS is filled with three to four of these trains, leaving an additional 8 25 ns buckets  
 752 unfilled due to the 220 ns rise time of the SPS kicker magnet. These three to four trains are  
 753 then injected into the LHC, where there are 38 or 39 bunch gaps due to the LHC injector 0.94  
 754  $\mu$ s rise time. At the end of a full LHC orbit, 119 buckets are left empty to allow for the rise time  
 755 of the beam dumping kicker magnet, used to remove beam from the LHC.

756 Once the beam is injected, the curved path around the circumference of the LHC is main-  
 757 tained via 1232 superconducting dipole magnets. The superconducting material niobium-titanium,  
 758 NbTi, is cooled to 1.9 K in order to produce the 8.33 T field. Figure 3.12(a) shows a cross-section  
 759 view of one of the LHC dipoles. The dual-bore design of the beam-pipe is enclosed by an iron  
 760 yoke, that serves as the cold mass to maintain the superconducting temperature, and provides  
 761 a 195 mm gap between each beam. A close up picture of the non-magnetic collar and supercon-  
 762 ducting coils are shown in figure 3.12(b). A simulation of the magnet in figure 3.12(c) shows the  
 763 homogenous, vertical magnetic field produced in the center of the coil. Diagram 3.12(d) shows  
 764 an exaggerated view of the 2812 m radius curvature of each dipole. However, since each dipole  
 765 is only  $\sim 14$  m in length, this curvature is hardly noticeable, as shown in a photo of an actual  
 766 dipole magnet in a staging area at CERN, awaiting installation in figure ??(e).

767 Quadrupole, septupole, octupole, and other multipole magnets are used to focus a single  
 768 beam, as well as squeeze the two beams together. There are 392 quadrupole magnets on the  
 769 LHC ring, each controlling the height and width of the beam. Figure 3.13(a) shows a schematic  
 770 of a dual-bore quadrupole magnet, and figure 3.13(b) shows an actual quadrupole in a staging  
 771 area before installation. Quadrupole magnets use four sets of coils to create a magnetic field that

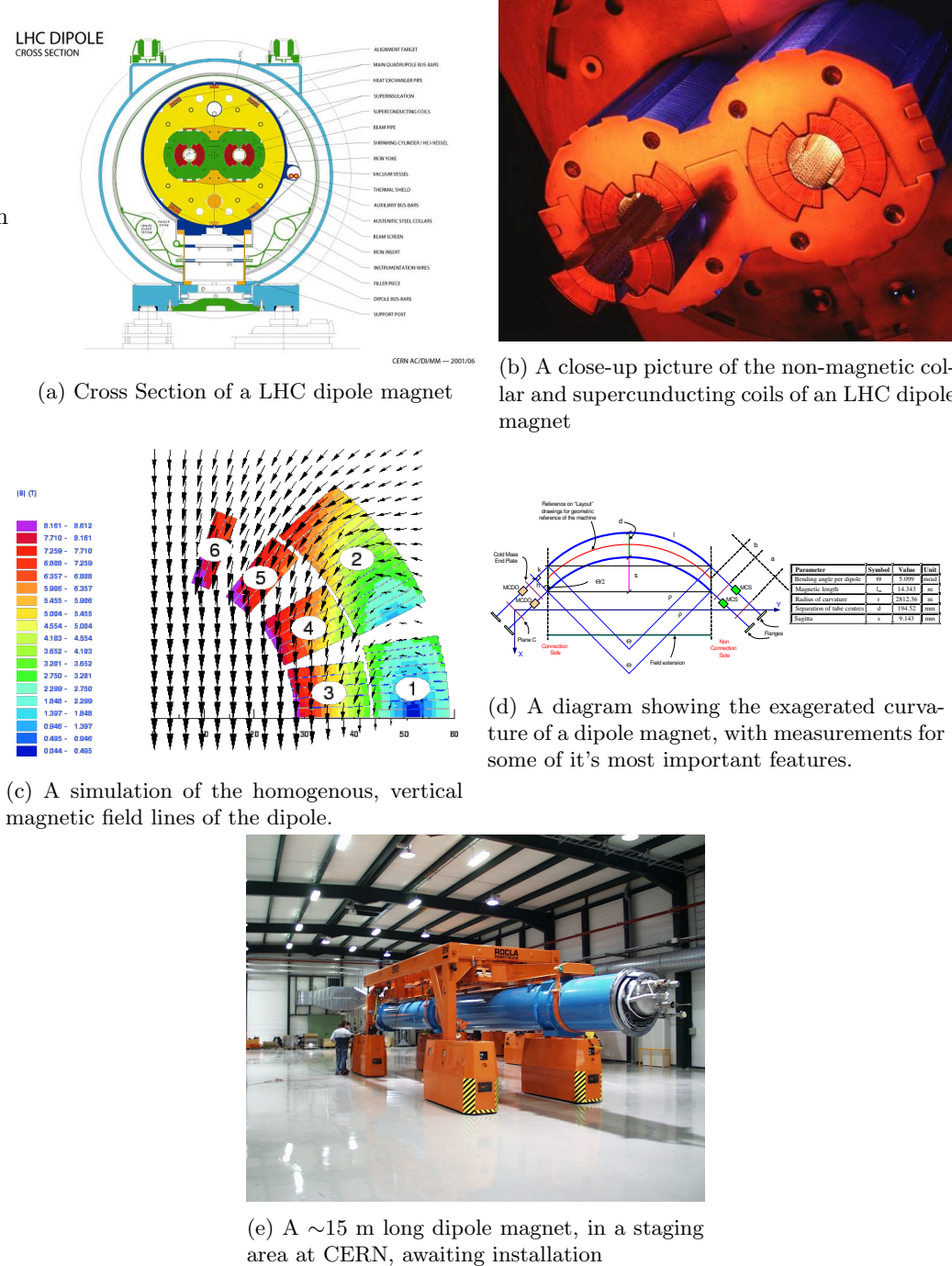
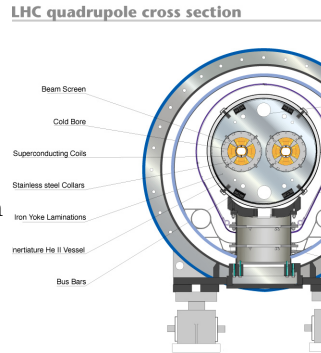


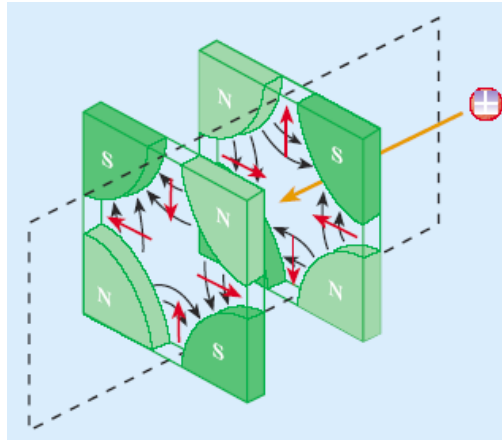
Figure 3.12: Features of the dipole magnets used in the LHC



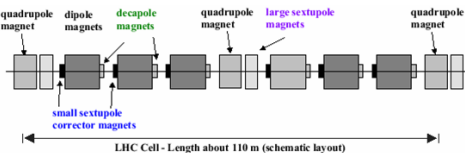
(a) Cross Section of a LHC quadrupole magnet



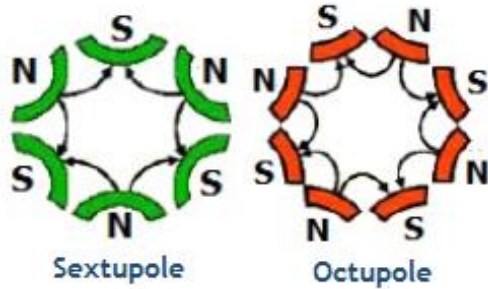
(b) A dual-bore quadrupole magnet, in a staging aread prior to installation



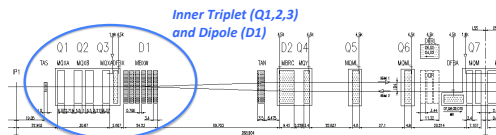
(c) A quadrupole magnet can provide focusing either in the horizontal or vertical direction



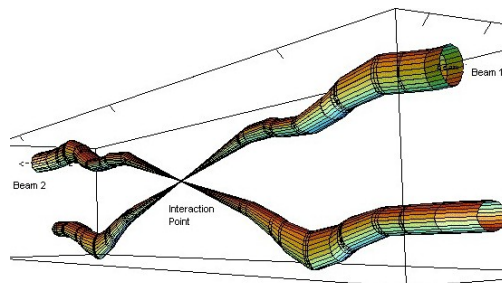
(e) A typical 110m long magnetic cell at the LHC featuring several types of multipole magnets



(d) Multipole fields from a sextupole and an octupole magnet



(f) Schematic of the Inner triplet structure that brings the two separate beams together in the interaction region



(g) A simulation of two beams being squeezed together by the inner triplet.

Figure 3.13: Features of the dipole magnets used in the LHC

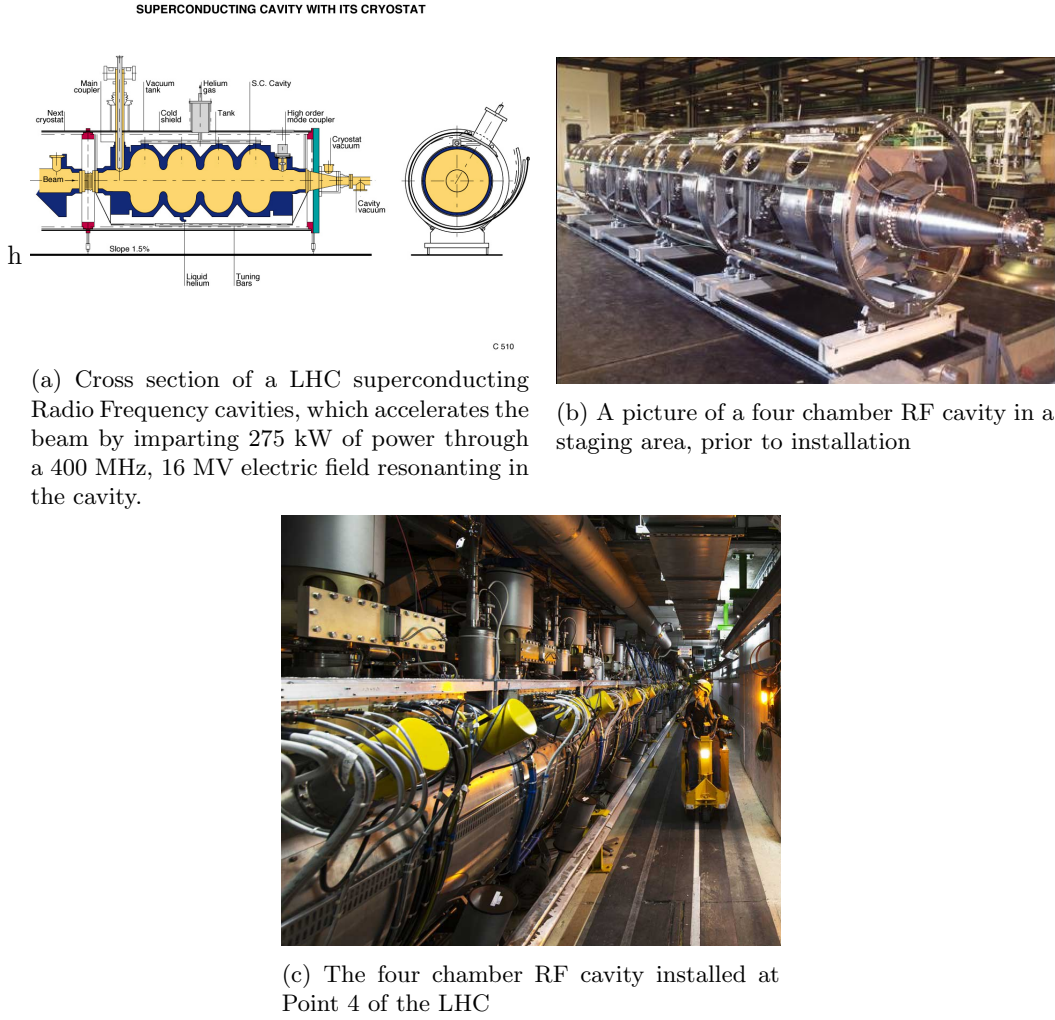


Figure 3.14: Features of the 400 MHz superconducting RF system used in the LHC

either squeezes the beam horizontally or vertically, as shown in figure 3.13(c). Finer corrections to the beam shape are made with the multipole magnets, since they are able to compress the beam from more than two axes. Figure 3.13(d) shows the fields lines of a sextupole and octupole magnet. A typical cell of magnets, 110 m long, in the LHC beamline is shown in a diagram in figure 3.13(e), where the dipole, quadrupole and higher order magnet work in series to confine the protons to the LHC ring. Finally, a set of single bore magnets, known as an inner triplet, bring the two beams together into an interaction region. Figure 3.13(f) shows the arrangement of magnets that squeeze the beam together, while figure 3.13(g) shows a simulation of the beams being brought together to collide in the interaction region.

### 3.3 LHC RF Technology

The LHC uses a 400 MHz superconducting RF cavity system to capture and accelerate the beam from 450 GeV to 7 TeV [54]. Two independent system are used to provide 8 MV of RF voltage

at injection at 16 MV during equilibrium at 7 TeV and deliver 275 kW of power to each beam. This is provided by 16 niobium sputtered cavities, housed in 4.5 K refrigeration units, known as cryomodules, at Point 4 of the LHC octant. The superconducting material covering the inside of the cavity has near-zero resistivity, which dissipates much less power and has a much narrower resonance width, or Q-factor, than a cavity made from normally conducting material. Figure 3.14(a) shows a schematic of a four cavity cryomodule. The beam pipe passes through the center of each chamber and longitudinal (left to right in the diagram) electric fields accelerate the protons each time they circulate the LHC ring. Figure 3.14(b) shows an actual four cavity module in a staging area prior to installation. In this picture, the resonance cavities are concealed underneath the cylindrical housing of the vacuum tank and cryostat. Figure 3.14(??) is a picture of the module installed at Point 4. The thin cylindrical structures extending off the top is the LHe intake valve and quench system. The thicker cylindrical structures are the waveguides that couple the cavities to the source of the electric field, the klystrons.

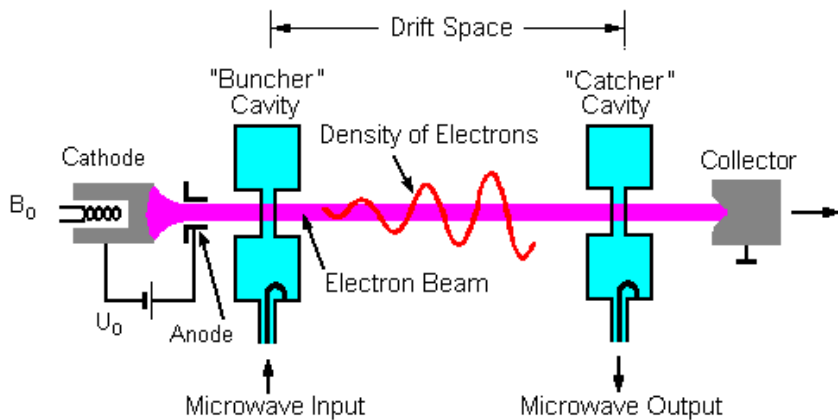


Figure 3.15: A klystron uses a weak RF signal coupled to a resonance cavity to bunch an electron beam, which in turn creates an amplified RF signal as it passes through a second resonance cavity tuned to the same frequency.

A Klystron is the source of RF power that builds up as a resonance in the cavities that accelerate the protons. Figure 3.15 shows a diagram of the basic operating principle. The device uses an anode to accelerate the thermionic emission of electrons off of a cathode material into one or more bunching cavities tuned to the frequency the device is designed to produce. This cavity is driven with a weak RF source, that groups electrons into bunches. Just as discussed for protons earlier, when electrons arrive at the entrance of the cavity at just the right time, it will experience the zero-point of the oscillation of the resonating electric field. If it arrives early or late, it is accelerated or decelerated and thus bringing it closer to its neighbors, and increasing the density of the beam. After passing through multiple chambers, the tightly bunched electrons enter a catcher cavity tuned to the same resonance frequency. As the electrons pass through at

807 this resonance frequency, standing electric waves are excited and quickly build up in the catcher  
 808 cavity. The electron beam is thus used to amplify the original RF signal in the catcher cavity,  
 809 which is then transported via waveguide to power the RF cavity used to accelerate the proton  
 810 beamline.

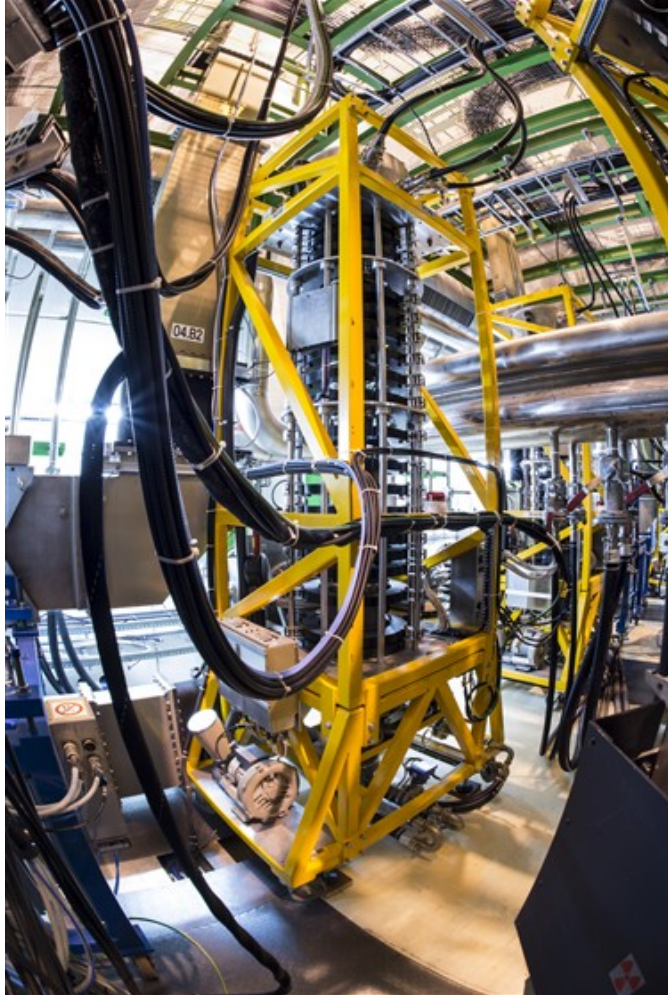


Figure 3.16: One of sixteen 300 kW, 400 MHz klystrons that power the superconducting RF cavities that accelerate the proton beam.

811 At the LHC, 16 400 MHz, 300 kW kylstrons, work together to provide 4800 kW of power  
 812 to the superconducting RF cavities [54]. They are also located at Point 4, in the UX45 service  
 813 cavern adjacent to the RF cavities, about 6 m below the beamline. An average of 22 m of  
 814 waveguide is used to transport the power generated by the kylstrons to the RF cavities. Figure  
 815 3.16 shows a kylstron installed at the LHC, and like most modern kylstrons, it also utilizes a  
 816 multi-bunching chamber design.

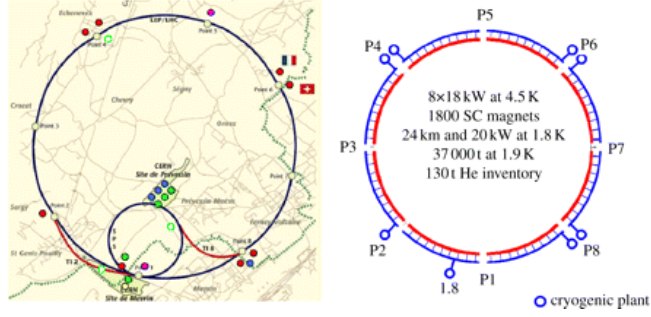


Figure 3.17: Layout of the five cryogenic islands, which are home to the eight facilities that provide liquid helium to the LHC



(a) The compressor station for the 4.5 K refrigeration system

(b) The 4.5 K refrigeration system cold box, containing heat exchanging fins and turbines to cool the He

Figure 3.18: Features of the 4.5 K refrigeration system

## 3.4 The LHC Cryogen System

The LHC is the largest cryogenic system in the world [66], as its operating temperature is 1.8 K, in order to produce the high-magnetic fields needed by the dipole magnets. Additionally, the acceleration mechanism, the RF cavities, are also superconducting, and must be cooled to 4.5 K. Over 120 tons of Helium are used as the cryogenic medium, since once it is cooled below 2.17 K, it becomes a superfluid, a phase of matter with a high thermal conductivity, making it ideal for refrigeration. Cryogenic and auxiliary equipment are concentrated into 5 cryogenic islands at Points 1, 2, 4, 6, and 8 [54]. As shown in figure 3.17, Point 4, 6, and 8 house two facilities each, making a total of eight, one for each octant of the LHC arc.

At each cryogenic plant, He is cooled to 80 K by circulating it through refrigeration equipment with liquid nitrogen in the heat exchangers [66]. Next, the He is brought to 4.5 K with refrigerators recovered from the LEP experiment [67]. The He gas is first compressed and allowed to expand, where it is cooled by losing energy through mechanical turbo-expanders that run at up to 140,000 rpm on helium-gas bearings. Figure 3.18(a). The He is then liquified after passing through a vacuum sealed box containing heat exchangers and more turbo-expanders [68].

832 The compressor for this system is pictured in figure 3.18(b). Finally, the liquified He is brought  
 833 to 1.8 K with a refrigeration unit that uses a cold compression train to decrease the saturation  
 834 pressure, and thus temperature as well.

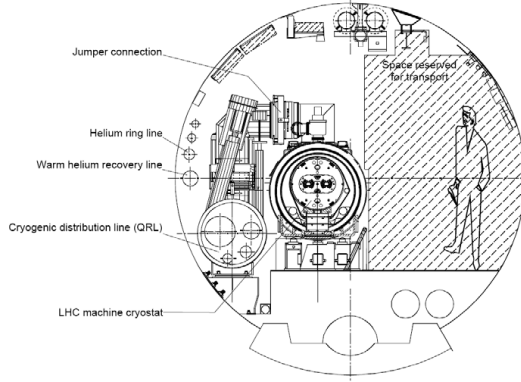


Figure 3.19: Cross section schematic of the cryogenic distribution system in the LHC tunnel

835 In the LHC tunnel, a cryogenic distribution line runs parallel to the machine [67]. It consists  
 836 of eight 3.2 km long cryostats, that contain the equipment to supply and recover helium with  
 837 temperatures ranging from 4 K to 75 K. A total of 310 service modules, are used to control the  
 838 system and provide safety mechanisms against pressure buildup and magnet quenching. Figure  
 839 shows a cross section of the cryogen distribution system in the tunnel.

### 840 3.5 The LHC Vacuum System

841 The LHC is also the largest operational vacuum system in the world and is capable of achieving  
 842 pressures lower than outer space [69]. Three different types of vacuum systems are used: one for  
 843 insulating the helium distribution lines, another for insulating the dipole magnets, and a final  
 844 ultra-high vacuum system for the beam pipe [54].

845 The vacuum systems for insulating the helium distribution and dipoles involves some 104 km  
 846 of piping an over 250,000 welding joints [69]. Pressure here is required to be kept at  $10^{-1}$  mbar,  
 847 but at cryogenic temperatures, pressures tend to equalize at a much lower level, to  $10^{-6}$  mbar  
 848 ( $\sim 10^{-9}$  atm) [54].

849 The most stringent requirements come on the vacuum of the beam-pipe. The beam must  
 850 minimize the number of interactions it has with any particles outside of the interaction region.  
 851 A pressure of  $10^{-10}$  to  $10^{-11}$  mbar are maintained in the 54 km of beampipe [69]. Weeks of  
 852 cryogenic pumping, eventually condenses gas trapped in the beampipe into a liquid that can be  
 853 absorbed by the walls of the beampipe. The inside beampipe is also coated with a thin layer



Figure 3.20: Beam screen for the LHC, with slits to allow for easy pumping of residual gas molecules in the beampipe.

of a special substance developed at CERN, a titanium-zirconium-vanadium alloy, which absorbs residual particles when heated. 780 ion pumps are used to remove the noble gases and methane, which do not interact with the substance, which acts as its own distributed pumping system. Room-temperature sections of the beampipe are also heated to  $300^{\text{deg}}$  to be baked-out from the outside. This is done to periodically remove any material which may have settled and become trapped. Additionally, the beam-pipe is designed with a racetrack shape, which optimises the available aperture while leaving space for the cooling tubes, as shown in figure 3.20. Slits also allow for gas molecules to be easily pumped out from inside its volume.

862 **Chapter 4**

863 **The Compact Muon Solenoid**

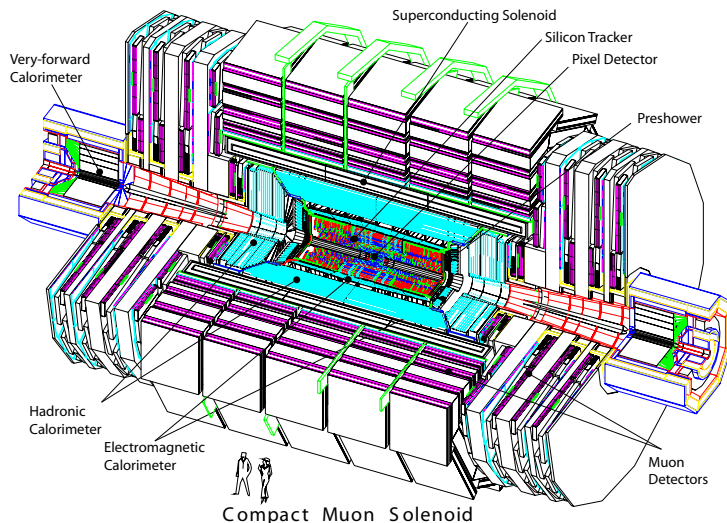


Figure 4.1: A cutaway diagram of the CMS detector. Two humans are present at the bottom of the image to provide scale.

864 The Compact Muon Solenoid (CMS) experiment is a general-purpose particle detector ca-  
865 pable of performing a wide range of physics measurements at the TeV energy scale. It provides  
866 hermetic,  $4\pi$ , coverage surrounding the interaction region on Point 5 of the LHC octant, and  
867 is capable of identifying and reconstructing charged and neutral hadrons, photons, electrons,  
868 and muons directly. Tau leptons, are measured indirectly through a careful reconstruction of  
869 its decay products. The hermetic coverage allows the detection of neutrinos by measuring a  
870 momentum imbalance in a given collision. The detector is assembled in five sections and weights  
871 over 14,000 tons. The "Compact" part of the experiment's name comes from its relativley small  
872 volume for a modern particle detector, with length of 28.7 m and a diameter of 15.0 m. Ironi-  
873 cally, this is as tall as most 4-5 story buildings and weights as much as  $\sim$ 7000 cars. Figure 4.1  
874 shows a cutaway drawing of the CMS detector.

A right-handed coordinate system is used to measure particle positions within the detector. The origin is centered at the nominal interaction point with the  $\hat{x}$  direction pointed towards the center of the LHC ring, the  $\hat{y}$  direction towards the sky, and the  $\hat{z}$  direction pointed counter-clockwise along the LHC ring towards Point 2 and the ALICE experiment. In the much more natural polar coordinates,  $\hat{r}$ , points radially outward from the interaction point, the azimuthal angle  $\hat{\phi}$  is measured as the angle relative to the  $\hat{x}$  axis, and the polar angle,  $\hat{\theta}$ , is measured as the angle relative to the  $\hat{z}$  axis. An important lorentz invariant position variable is the rapidity,  $y$ , and its approximation in terms of the polar angle, the pseudorapidity,  $\eta$ :

$$\begin{aligned} y &= \frac{1}{2} \ln \left( \frac{E + p_z c}{E - p_z c} \right) \\ \eta &= -\ln \left( \tan \frac{\theta}{2} \right) \end{aligned} \quad (4.1)$$

The psuedorapidity is useful since it is an approximately lorentz invariant version of polar angle, which allows for a more intuitive understanding of the distribution of particles when boosting into different measurement reference frames. The component of the momentum transverse to the beamline,  $p_T$  is the most common form of measuring the momentum, and is defined as  $p_T = |p| \cos \phi$ .

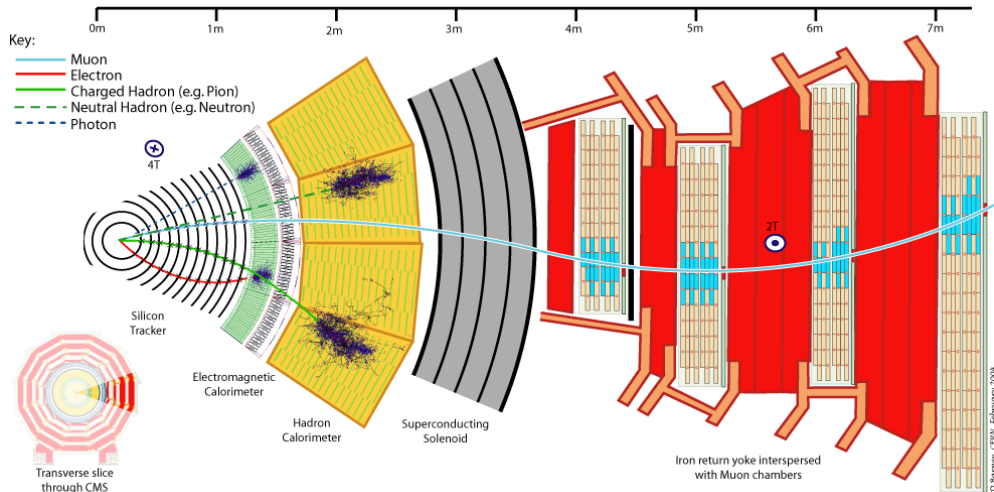


Figure 4.2: A slice of the CMS detector showing how various particles interact and deposit energy. The trajectory of charged particles is measured in the tracker; electrons and photons deposit most of their energy in the ECAL; charged and neutral hadrons deposit most of their energy in the HCAL; the muon chambers measures the trajectory of muons or long-lived charged particles

CMS is composed of a system of sub-detectors, each specialized in measuring a certain type or characteristic of a particle. They are arranged approximately as concentric cylinders of increasing radius, wrapped around the interaction region of the  $pp$  collisions and an analogy is often made between the layers of subdetectors being similar to the layers of an onion. The closest sub-

detector to the interaction region is the tracker system. It is an all silicon pixel and strip detector, with a high precision position resolution, which is used to identify the trajectory of charged particles close to the primary vertex of a collision. The Electromagnetic Calorimeter (ECAL) is the next layer, and is used to absorb energy of electromagnetically interacting particles. It uses lead-tungstate ( $\text{PbWO}_4$ ) crystals which act as both the absorbing and scintilating medium for energy deposited by charged particles and photons as they pass through this sub-detector. The Hadronic Calorimeter (HCAL) uses brass and steel tiles to absorb energy and induce hadronic interactions, while a plastic scintillator material layered between the absorber tiles samples the energy of hadrons. The tracker, ECAL, and HCAL systems are all contained in the bore of the 3.8 T solenoid from the CMS namesake. This device bends the trajectory of charged particles as they traverse the detector, and the curvature of this bend is used to obtain information on the charge and momentum of the measured particle. The muon system sits outside of the solenoid structure, and uses three types of detection systems: drift tubes (DTs), resistive strip chambers (RPCs) and cathode strip chambers (CSCs), which provide excellent timing and position resolution. The return yoke structure of the magnet also provides the mechanical support for the muon chambers. Figure 4.2 shows a slice of the CMS experiment showing how various particles interact and traverse the different sub-detector regions, as described above.

At center-of-mass energy of  $\sqrt{s} = 14 \text{ TeV}$ , the expected event rate is approximately  $10^9$  events/second. This is too much information to store and analyze, and is mainly dominated by Standard Model QCD multi-jet production, a background for searches for new particles or physics. An online event selection, or trigger, must be used to reduce this rate to a manageable 100 events/second. This is achieved through a combination of hardware, firmware, and software that provides a rough reconstruction of events in near real-time, and makes a decision about whether it meets a minimum set of criteria to be used in an analysis.

## 4.1 The Tracker

The innermost sub-detector is an all silicon pixel and strip tracker designed to provide precise and efficient measurement of the trajectories of charged particles and reconstruction secondary vertices necessary for identification of  $b$ -jets and  $\tau$  leptons.

At peak LHC design luminosity of  $10^{34} \text{ cm}^{-2} \text{ s}^{-1}$ , and bunch spacing of 25 ns, there will be  $\sim 1000$  particles from 20 overlapping  $pp$  collisions for each bunch crossing. This corresponds to a hit rate density of  $1 \text{ MHz/mm}^2$  at a radius of 4 cm,  $60 \text{ kHz/mm}^2$  at 22 cm, and  $3 \text{ kHz/mm}^2$  at 115 cm from the beam line. This large particle flux will also cause intense radiation damage to detector components. These conditions necessitate the use of radiation-hard silicon, with a high-

925 granularity to create a low occupancy for each detector element, which are read out by fast  
 926 electronics. Additional mitigation of the effects of radiation damage is taken by cooling and  
 927 operating the entire detector to  $-10^{\circ}$  C in order to maintain a signal to noise ratio of 10:1 for  
 928 the sensors. After 10 years of running, it is anticipated that this will need to decrease to  $-27^{\circ}$  in  
 929 order to compensate for the accumulated damage.

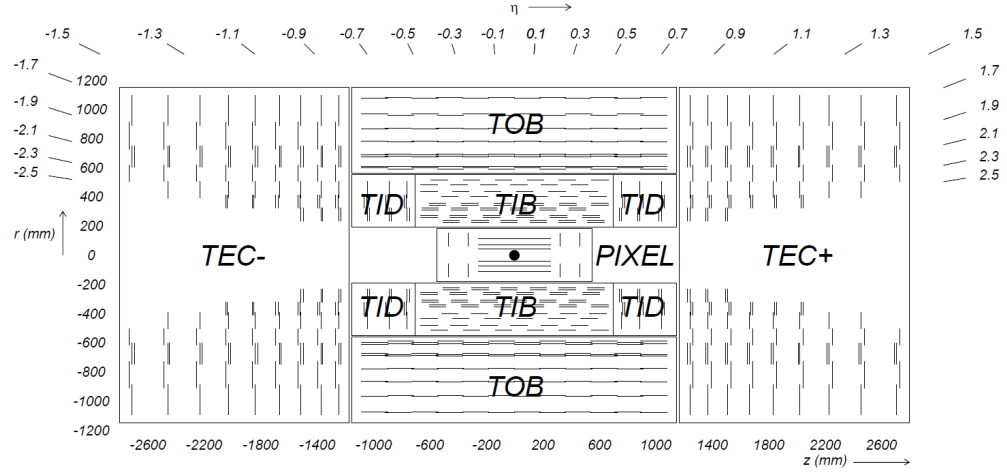


Figure 4.3: A side view of the tracker. The pixel detector is the innermost sub-system, with three concentric rings of detectors in the barrel, and two in the endcap. The tracker inner barrel (TIB) is a silicon strip detector, with four concentric rings. The tracker inner disks (TID) are three layers deep. The tracker outer barrel (TOB) is six concentric rings and the tracker end caps (TEC) are nine layers deep.

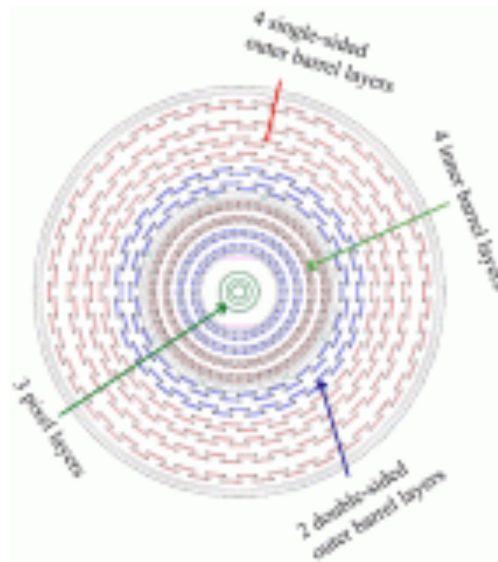


Figure 4.4: A head-on view of the beamline and barrel components of the tracker.

930 The tracker has a cylindrical shape that surrounds the interaction region, with a length of  
 931 5.8 m and a diameter of 2.5 m. The large particle flux close to the beamline requires the use  
 932 of a pixel detector sub-system in the innermost region, from radius 4.4 cm to 10.2 cm from  
 933 the beamline. The particle flux drops off sufficiently at larger radii to use silicon strip detectors,

arranged into four different sub-systems: the tracker inner barrel (TIB), tracker inner disks (TID), tracker outer barrel (TOB) and tracker end caps (TEC), which extend to a radius of 1.2 m from the beamline. Figure 4.3 shows a side view of the tracker layout and figure 4.4 shows a view down the beamline of the barrel sections. The tracker has a total acceptance of  $|\eta| < 2.5$ .

There are competing factors for the radial length of the tracker. More layers allow for more samples of a particle's trajectory, giving a higher spatial precision, but more material means photons and hadrons are more likely to decay, and create a shower of particles that would better measured through the absorption of energy via calorimeters. The depth of the tracker varies from 0.4 to 1.8 radiation lengths, resulting in small degradation of the ECAL performance, since approximately half the photons will be converted to  $e^+e^-$  pairs.

#### 4.1.1 The Silicon Pixel Detector

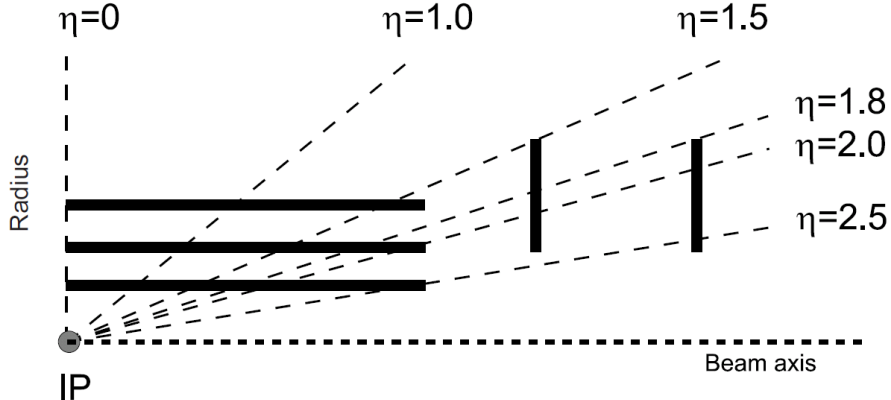


Figure 4.5: The three barrel and two disk layers of the silicon pixel tracker provide coverage of  $|\eta| < 2.5$

The pixel detector consists of 66 million  $100 \times 150 \mu\text{m}$  pixels, arranged in three concentric cylindrical layers of radius of 4.4, 7.3, and 10.2 cm from the beam line and two disc layers on either side of the barrel detectors. Figure 4.5 shows the eta coverage of the detector out to  $|\eta| < 2.5$ .

The sensor technology uses a  $n$ -on- $n$  concept, where a high-dose  $n$ -implant is introduced onto a  $n$ -substrate with large resistance. A  $p - n$  junction is made by the placement of a  $p$ -type semiconductor on the back side of the substrate. When a charged particle passes through the face of the substrate, between the  $p - n$  junction, it liberates electrons from the silicon atoms, creating electron-hole pairs. The  $p$ -side has a voltage bias of 150 V in the barrel, and 300 V in the disks, that sweeps the pair apart, creating a current. Pixels are isolated from one another using a moderated  $p$ -spray in the barrel region, and open  $p$ -stops in the disks in order to create an additional  $p - n$  structure that acts like a diode to limit current flow between pixels. The 3.7 T

957 magnetic field of the CMS solenoid also induces a Lorentz drift of the current in the  $\hat{\phi}$  direction.  
 958 This results in the current produced in one pixel being shared among multiple neighboring pixels.  
 959 The charge collected by each of the multiple pixels are read-out, using an interpolation between  
 960 pixels, resulting in a  $15\text{-}20 \mu\text{m}$  spatial resolution on the trajectory of the charged particle - much  
 961 smaller than the size of an individual pixel. In order to induce this effect in the disks (where the  
 962 pixels are orientated perpendicular to the barrel), the pixels are angled  $20^\circ$  in the  $\hat{y}$  direction.

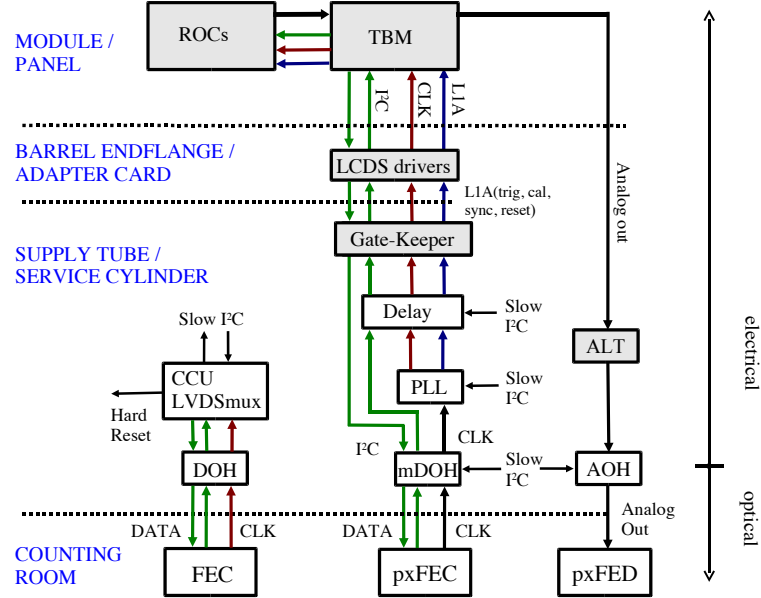


Figure 4.6: The readout electronics chain for the pixel detector

963 The current created by the charged particle is collected by a readout chip (ROC) that is  
 964 soldered with a bump bond type connection to the pixel. The ROC is a custom ASIC chip,  
 965 that processes the signals for a grid of  $52\times 80$  pixels. It provides amplification, buffering, and  
 966 zero suppression (threshold) of the charge from each pixel. Depending on the layer, 8-16 ROCs  
 967 in the barrel, and 21-24 ROCs in the disks are connected and read-out by a single token bit  
 968 manager (TBM) chip. This chip communicates information from the sensors to the trigger  
 969 system, which is used to determine whether a given event is stored as data for analysis later.  
 970 The pixel front end controller (pxFEC) interfaces with the ROC and TBM and provides central  
 971 clocking and communicates to the CMS data acquisition system. The pixel front end digitizer  
 972 (pxFED) converts the analog signals from the ROC and TBMs. A total of 40 pxFED (32 in the  
 973 barrel and 8 in the disks) modules are used to read-out the entire pixel detector, and figure 4.6  
 974 shows a schematic of the pixel read-out chain.

975 The resolution of the pixel detector was measured in 2012 with  $\sqrt{s} = 8 \text{ TeV}$   $pp$  collision. The  
 976 residual distance between the hit position recorded by a pixel, and an interpolated track that

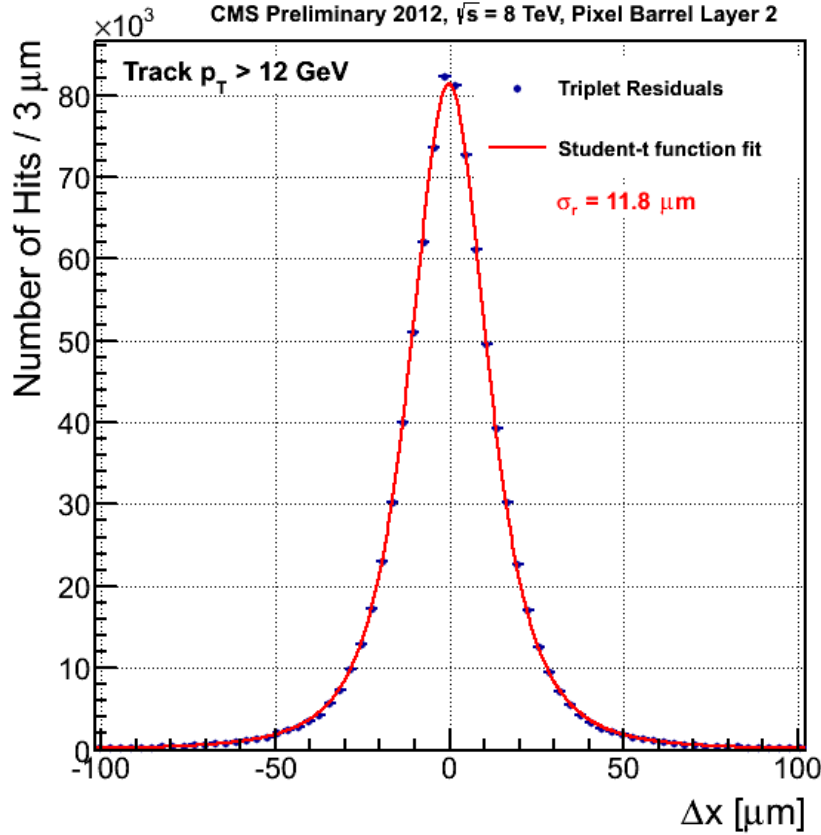


Figure 4.7: In 2012  $pp$  collisions at  $\sqrt{s} = 8$  TeV, the pixel detector performed with a resolution of  $11.8 \mu\text{m}$ . The above is a plot of the residual difference between a pixel and the results of a fit to a particle track.

977 uses that hit is plotted and fit with a student-t function in figure 4.7. For tracks with  $p_T > 12$   
 978 GeV, the pixel detector was found to have a spatial resolution of  $11.8 \mu\text{m}$ .

### 979 4.1.2 The Silicon Strip Detector

980 As shown in figure 4.3, the silicon strip tracking system has four components: the tracker inner  
 981 barrel (TIB), tracker inner disks (TID), tracker outer barrel (TOB) and tracker end caps (TEC).  
 982 A total of 15,148 detector modules are distributed among these systems, each with either one  
 983  $320 \mu\text{m}$  thick sensor, or two  $500 \mu\text{m}$  thick sensors, making 24,244 sensors with an active area of  
 984  $198 \text{ m}^2$  of silicon. A model with two sensors is shown in figure 4.8. Each sensor has either 512  
 985 or 768 strips since they are read out by two multiplexed 128-channel front end chips, making it  
 986 possible to only read out sensors in groups of 256. Each strip has a pitch that varies between 80  
 987 and  $200 \mu\text{m}$  and lengths that vary between 10 and 25 cm. All in all, 9.3 million strips are used  
 988 in the silicon tracker.

989 The TIB and TID provide radial coverage from 20 to 55 cm. The TIB has four barrel layers,  
 990 with  $80 \mu\text{m}$  pitch strips on the first two layers, and  $120 \mu\text{m}$  strips on the outer two, giving a single

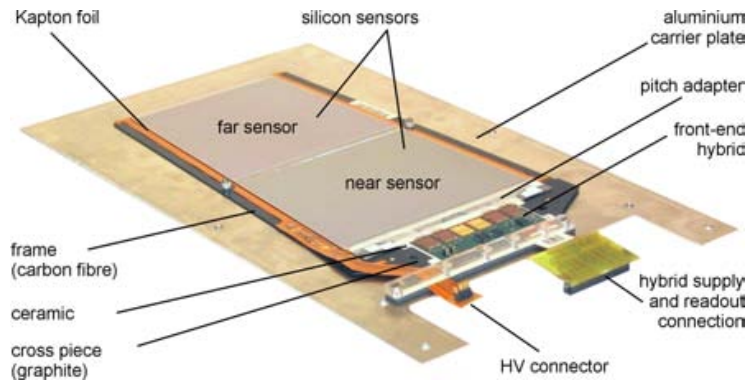


Figure 4.8: A silicon strip module, with two  $500 \mu\text{m}$  thick sensors.

point resolution of 23 and  $35 \mu\text{m}$  respectively. The strip pitch varies between 100 and  $141 \mu\text{m}$  in the three discs of the TID. The TOB surrounds the TIB/TID and is composed of six barrel layers that extend the tracker radius to 116 cm. It is composed of  $500 \mu\text{m}$  thick strip sensors, with pitches of  $183 \mu\text{m}$  in the first four layers and  $122 \mu\text{m}$  in the outer two layers. It provides 6 measurement points of the particle trajectory with a single point resolution of 53 (35)  $\mu\text{m}$  in the first four (last two) layers. Each TEC is made of 9 discs, each with 7 rings of strip detectors. The inner four rings of each disk use the single,  $320 \mu\text{m}$  thick strip modules, while the outer three rings use the double,  $520 \mu\text{m}$  thick strip modules. The average pitch varies between 97 to  $184 \mu\text{m}$  in each of the rings. In the first two layers of the TIB, the first two rings of the TID, the first two layers of the TOB, and rings 1, 2, and 5 in each disk of the TEC contain modules mounted back-to-back, with an angle of 100 mrad between them to provide a two-dimensional measurement of a particle's trajectory.

Each of the strips is a single sided  $p$ -on- $n$  type silicon sensor manufactured on 6 inch wafers, with a base material of  $n$  doped silicon. The front side of the wafer is implanted with a  $p^+$  type semiconductor. A uniform  $n^+$  implantation on the back forms the ohmic contact to 500 V. This forms a  $pn$  junction and when a charged particle passes through the face of the wafer, atoms in the junction are ionized and the 500 V potential difference creates a current out of the resulting electron/hole pairs. This current is collected and processed through the read-out system.

A custom integrated circuit, the APV25, is used to amplify, shape, and buffer the signals produced from the silicon strips. It has 128 read-out channels, and samples the detector signals at the 40 MHz, suitable for the 25 ns collisions. It is able to store data for up to 4  $\mu\text{s}$  to account for trigger latency. Two APV25 chips are linked with fiber optics to the Front End Driver

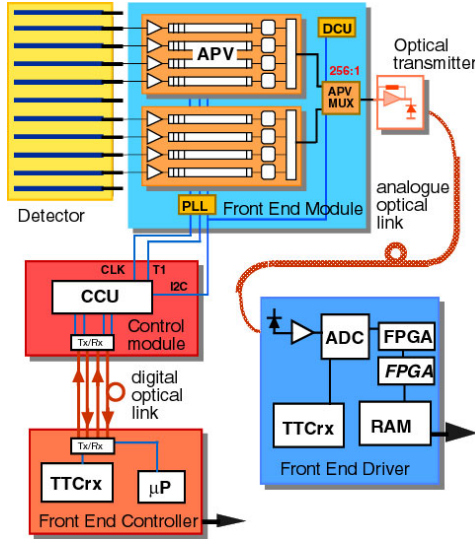


Figure 4.9: Schematic of the readout sequence of the silicon strip detector.

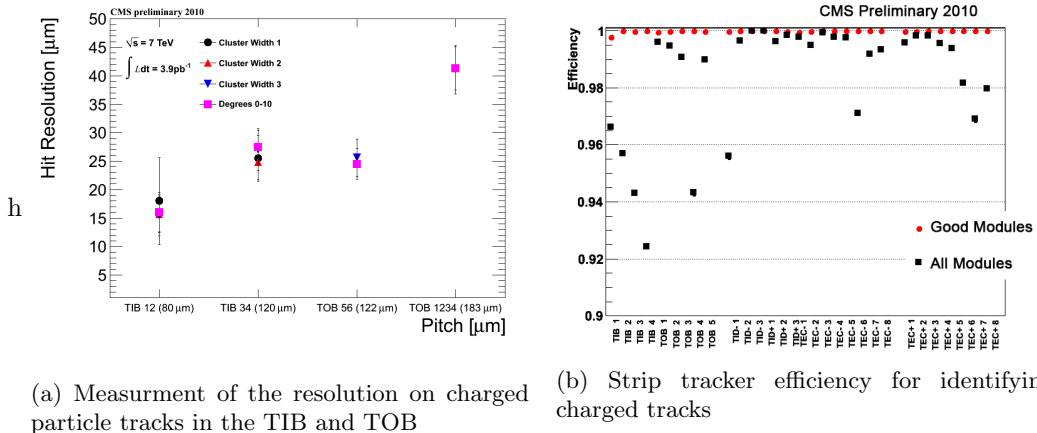


Figure 4.10: Measurements of the performance of the silicon strip track using  $pp$  collisions from 2011 at  $\sqrt{s} = 7 \text{ TeV}$

1013 (FED) system. Each FED receives data from 94 optical fibers, and digitizes them in parallel.

1014 The Front End Controller (FEC) transmits clock, trigger, and control data to the APV25s. The  
1015 entire readout chain is shown in figure 4.9.

1016 In 2011, the strip efficiency and resolution were measured from data in center-of-mass energy,  
1017  $\sqrt{s} = 7 \text{ TeV}$   $pp$  collisions. Figure 4.10(a) shows the resolution varying between 15-40  $\mu\text{m}$  for the  
1018 TIB and TOB detectors. Figure 4.10(b) shows the efficiency for reconstructing tracks with the  
1019 strip tracker, which is well above 99% when only considering operational modules.

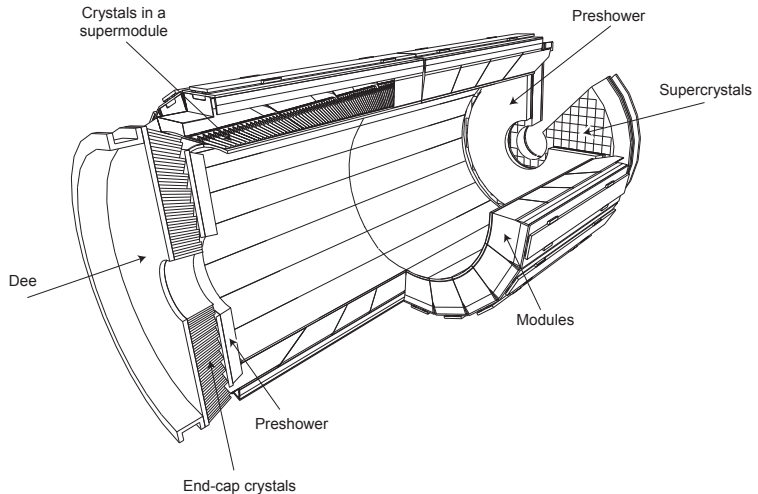


Figure 4.11: Layout of the ECAL sub-detector

## 1020 4.2 The Electromagnetic Calorimeter

1021 The Electromagnetic Calorimeter (ECAL) surrounds the inner tracker with 61,200 high density  
 1022 lead tungstate ( $\text{PbWO}_4$ ) crystals in the central barrel section, and 7,324 crystals in each of  
 1023 the two endcaps. The crystals have a fast response, provide fine granularity, and are radiation  
 1024 resistant, making them ideal for the LHC environment and the physics goal of observing the  
 1025 Standard Model Higgs boson decay to two high energy photons. The primary background for  
 1026 this process comes from neutral pions decaying to two photons, which is especially difficult when  
 1027 the photons are close together and can potentially be reconstructed as a single high-energy  
 1028 photon. This occurs most frequently in the endcaps, so an additional detector, the preshower,  
 1029 provides additional spatial resolution with silicon microstrip detectors, similar to those in the  
 1030 tracker. Figure 4.11 shows the layout of the ECAL.

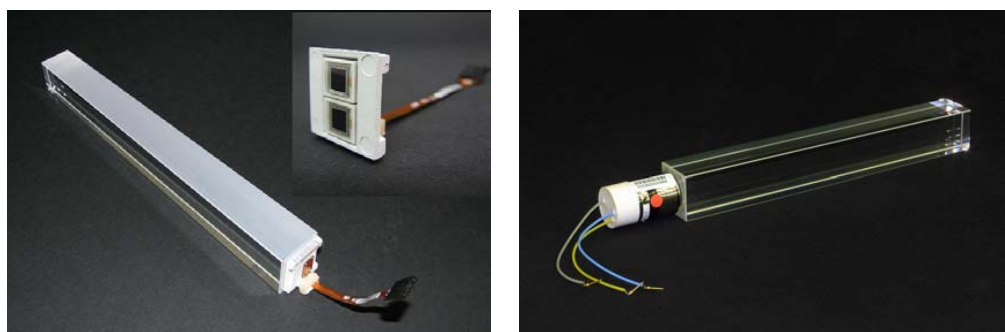


Figure 4.12: Typical Lead Tungstate crystal, with APD attached to the rear face in the left frame, and a VPT attached in the right frame.

1031 Lead tungstate is an ideal material for electromagnetic calorimetry. Figure 4.12 shows a  
 1032 typical crystal, with photomultipliers attached to the rear faces, which will be discussed later.

1033 The material has a high density,  $8.28 \text{ g/cm}^3$ , giving it a large electromagnetic cross-section,  
 1034 making it much more likely for a particle traversing the crystal to interact with one of the atoms  
 1035 in its structure. When a particle interacts with the crystal, it does so by depositing energy into  
 1036 its atoms, which excite the electrons that are bound to it. The atoms then relax by emitting  
 1037 photons, in a process known as scintillation and the  $\text{PbWO}_4$  crystals release 80% of their light  
 1038 in the 25 ns LHC bunch crossing time. This light is collected by photomultipliers attached to  
 1039 the rear face of the crystal and converted into an electrical signal. Read-out electronics amplify,  
 1040 digitize, and buffer the signal until it can be stored as data or discarded.

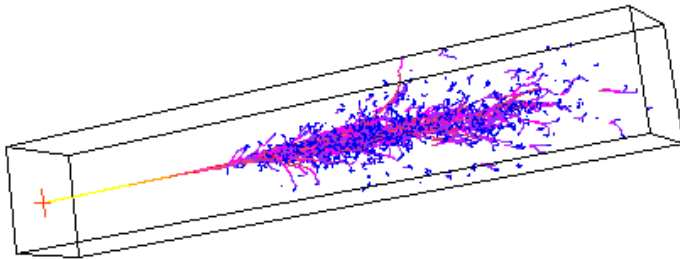


Figure 4.13: A simulation of the evolution of a electromagnetic shower being initiated by an electron entering the center of the front face.

1041 As a charged particle or photon begins to deposit energy, it begins a decay chain into many  
 1042 lower energy photons and electrons, known as an electromagnetic shower. Electrons, being  
 1043 bent by the CMS magnetic field, and multiple scattering off of the  $\text{PbWO}_4$  crystals, create  
 1044 bremsstrahlung photon radiation. Since the intensity of bremsstrahlung is inversely proportional  
 1045 to the mass of the particle squared, particles heavier than electrons such as muons and hadrons  
 1046 do not leave a large signature in the ECAL. Photons convert to  $e^+e^-$  pairs, which in turn create  
 1047 additional bremsstrahlung. The crystals have a short radiation length,  $X_0=0.89\text{cm}$ , which is the  
 1048 distance it takes an electron to deposit  $1/e$  of its energy through bremsstrahlung, and  $7/9$  of  
 1049 the mean free path of a high energy photon before it converts to an  $e^+e^-$  pair. A corollary  
 1050 of the crystal's short radiation length is its small Moliere radius,  $2.2\text{cm}$ , which is the radius of  
 1051 a cylinder that encloses 90% of the electromagnetic shower's energy deposition. A typical  
 1052 crystal has a front face that is  $22\times 22 \text{ mm}^2$ , a rear face of  $26\times 26 \text{ mm}^2$ , and a length of  $230 \text{ mm}$ ,  
 1053 or  $25.8 X_0$  radiation lengths. This means that a relatively small grid of crystals can be used to  
 1054 fully collect the energy deposited by a high energy electron or photon. As previously mentioned,  
 1055 heavier charged particles will not bremsstrahlung as much as electrons, and will travel through  
 1056 the entire ECAL, depositing only a moderate fraction of their energy in the crystals. Figure 4.13  
 1057 shows a simulation of an electromagnetic shower produced by an electron entering the front face  
 1058 of a crystal.



Figure 4.14: A module of 500 crystals (25 crystals wide by 20 crystal tall).

1059     The barrel of ECAL (EB) covers a pseudorapidity range of  $|\eta| < 1.479$  with 61,200 crystals  
 1060    at a radius 1.29 m from the beam-line. The crystals are positioned in a quasi-projective geometry,  
 1061    such that their axes make a  $3^\circ$  angle with respect to the vector pointing to the nominal interaction  
 1062    point. This ensures that particles will not pass through the cracks and spaces between crystals,  
 1063    and are forced to interact with a portion of the ECAL. Crystals are assembled in groups of  
 1064    400 or 500 into modules, as shown in figure 4.14 . Four of these modules are assembled into a  
 1065    supermodule contain 1700 crystals, and 36 supermodules make up the barrel region.

1066     The crystals in the EB are read out by Avalanche Photo-Diode (APD) photomultipliers,  
 1067    shown in the left frame of figure 4.12. The APDs were manufactured by Hamamatsu and are a  
 1068    bulk *n*-type silicon material, with a *p*-type implanted on its surface to form a *pn*-junction. The  
 1069    operation principle is similar to that of tracker. When scintillation light from the lead tungstate  
 1070    crystals enters the face of the APD, it creates electron-hole pairs in the intrinsic region between  
 1071    the *p* implantation and the *n* bulk material. The APD is biased with 45 V, which creates a  
 1072    current from the electron-hole pairs and is the signal that a particle has created scintillation in  
 1073    the crystal. The APD provides a gain of 50 and has a quantum efficiency of 75%. Both the  
 1074    APDs and the PbWO<sub>4</sub> exhibit a strong temperature dependence, so the entire system is kept at  
 1075    18° C with a water-based cooling system distributed throughout the barrel and end-caps.

1076     The ECAL readout electronics are designed to read-out a  $5 \times 5$  array of crystals, known as a  
 1077    trigger tower, in the EB, and a single supercrystal in the EE. Each trigger or tower or supercrystal  
 1078    consists of 5 Very Front End (VFE) boards, each connected to 5 APDs (VPTs), one Front End  
 1079    (FE) board, two (EB) or six (EE) Gigabit Optical Hybrids (GOHs), one Low Voltage Regulator  
 1080    (LVR) and a motherboard. Once triggered, the APD (or VPT in the EE) is sampled 10 times, at

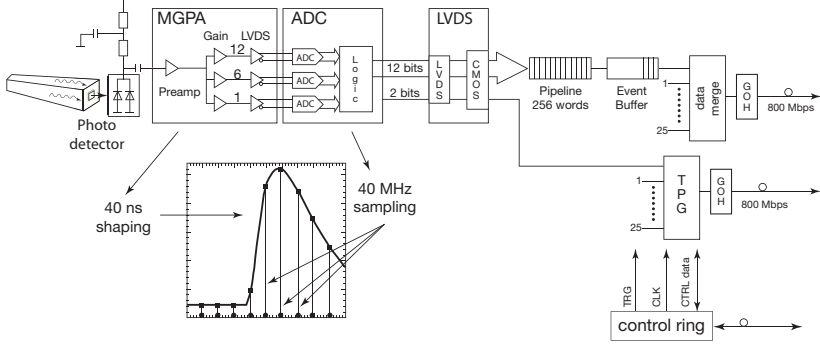


Figure 4.15: Schematic of the On-Detector Readout for the ECAL

1081 a 40 MHz sampling rate, and amplified by a multi-gain amplifier (MGPA), with nominal gains  
 1082 of 1, 6, and 12 contained on the VFE. These digitized samples are sent to the FE, where they  
 1083 are buffered until receiving a Level-1 trigger, where they are sent to the off-detector elcectronics  
 1084 Data Concentrator Card (DCC) via the GOHs. Figure 4.15 shows a schematic of the on-detector  
 1085 read-out.

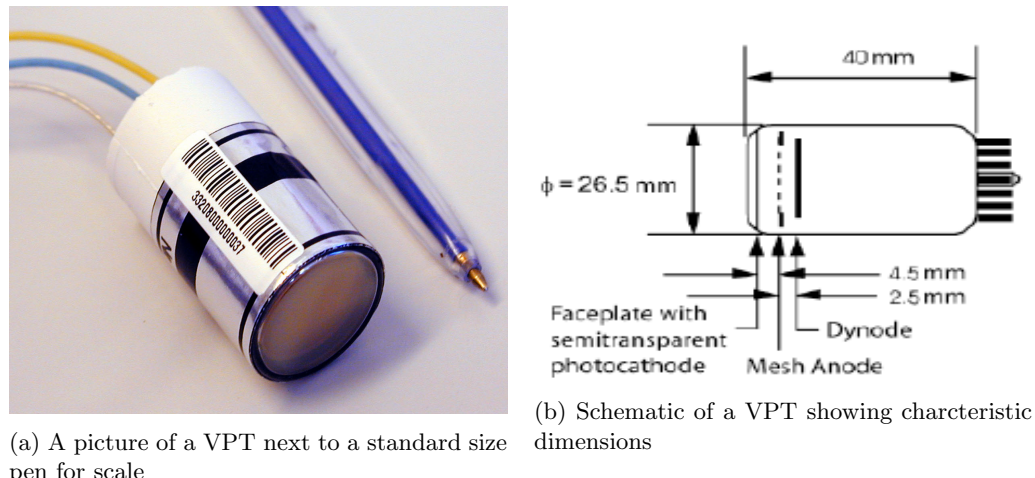
1086 In the barrel, the  $5 \times 5$  trigger towers are divided in the 5 strips in the  $\hat{\phi}$  direction. The energy  
 1087 deposits in these strips is summed by the FE cards and define the transvere energy of the tower.  
 1088 In the endcaps, supercrystals are divided into groups of five contiguous crystals of variable shape,  
 1089 known as psuedo-strips. The energy of these strips is performed by the FE, and the off-detector  
 1090 electronics use these to compute the transvere energy deposition.

1091 The preshower detector sits in front of the ECAL end-caps and provides coverage from  
 1092  $1.653 < |\eta| < 2.6$ . It is a two-layer sampling calorimeter. Lead radiators initiate electromagnetic  
 1093 showers from electrons and photons, and silicon strips are placed behind them to measure trajec-  
 1094 tories and deposited energy of passing particles. The total thickness is 20cm, which corresponds  
 1095 to a 2 raidation lengths in the first layer, and another radiation length in the second layer. 95%  
 1096 of photons are converted to  $e^+e^-$  pairs after the first layer. Each silicon sensor is composed of  
 1097 31 strips, with thickness of  $320 \mu\text{m}$  and are 1.9 mm in pitch. A front-end ASIC performs pre-  
 1098 amplification, shaping, voltage sampling, and communicates informaiton to the trigger system  
 1099 to determine if data is stored or discarded. The structure is formed into Dees, and two Dees  
 1100 form a disk with a hole for the beam-line to pass through.

1101 Behind the preshower is the ECAL end-cap (EE). It covers the psuedorapidity range of  
 1102  $1.479 < |\eta| < 3.0$ , and sits a longitudinal distance of 315.4 cm from the nominal interaction point.  
 1103 Crystals are grouped into  $5 \times 5$  modules known as supercrystals (SCs). Like the preshower, each  
 1104 endcap is divided into two sections, Dees, which form a disk with an inner bore for the beam  
 1105 line to pass through, as shown in figure 4.16. Each Dee holds 3,662 crystals, which are divided



Figure 4.16: A section of the ECAL end-cap, a Dee. Two Dees form a disk with an inner bore for the beam-line to pass through. 5x5 modules, or supercrystals, are mounted in preparation for installation at CMS



(a) A picture of a VPT next to a standard size pen for scale

(b) Schematic of a VPT showing characteristic dimensions

Figure 4.17: Vacuum Photo-Triode devices used in the ECAL end-caps (EE)

<sub>1106</sub> into 138 supercrysals, and 18 special partial-supercrystals for the inner and outer sections of the  
<sub>1107</sub> Dee.

#### <sub>1108</sub> 4.2.1 Vacuum Photo-Triodes

<sub>1109</sub> The photomultier used to readout the lead tungstate crystals in the EE is the Vaccum Photo-  
<sub>1110</sub> Triode (VPT), shown in the right frame of figure 4.17(a). Each device is 26.5mm in diameter  
<sub>1111</sub> and 40mm in lenth as shown in figure 4.17(b). It is a gain stage device. Photons from the  
<sub>1112</sub> lead tungstate scintilation light enter the front face of the VPT and liberate electrons from the  
<sub>1113</sub> grounded bialkali photocathode (SbKCs) via the photoelectron effect. The cathode material  
<sub>1114</sub> has a quantum efficiency of  $\sim 20 - 25\%$ . The photo-electrons are accelerated towards the mesh

1115 anode grid, which is held at 800 V. Approximately half the photo-electrons pass through the  
 1116 mesh and encounter a dynode plate held at 600 V. Electrons either collide with the dynode,  
 1117 liberating secondary electrons from the collision, or are turned around by the 200 V differenc  
 1118 between anode and dynode. Electrons are thus constantly accelerated towards the anode, and  
 1119 create secondary electrons as they collide with the anode. The process repeats with the secondary  
 1120 electrons, creating an avalanche of charge near the anode. As these charges eventually recombine  
 1121 with the anode over the course of a few nanoseconds, the voltage of anode drops, signaling the  
 1122 device has detected a photon from the PbWO<sub>4</sub> crystals.

1123 The performance of the VPT is degraded over time by two effects associated with exposure  
 1124 to the scintillation light from the crystals. The first is loss of the vacuum inside the tube.  
 1125 Molecules from the air become ionized by the large voltages and the positive ions are accelerated  
 1126 towards the photo-cathode, which is damaged through the resulting collision. The second effect  
 1127 is the gradual depletion of photo-electrons from the bialkali cathode material. The result is a  
 1128 decrease in the current, and thus signal, produced by the anode. Both of these effects can be  
 1129 effectively modeled as the sum of two falling exponential functions. The University of Virginia  
 1130 has studied the performance of VPTs with respect to their light exposure rates over the course  
 1131 of several years in order to characterize the device's response and long-term behavior.

#### 1132 4.2.2 Test Rig at UVa

1133 The University of Virginia (UVa) has continuously monitored four production VPTs operated  
 1134 at 800 V anode and 600 V dynode, in a 3.8 T field, at 15° to the tube axis, with photocath-  
 1135 ode currents of approximately 10 nA. This was done to simulate light exposure from the lead  
 1136 tungstate crystals in the forward regions of the ECAL end-caps, as well as provide an accelerated  
 1137 simulation of photocurrents that would be experienced in the larger eta regions. As described  
 1138 above, the light exposure is theorized to be the most significant cause of the loss of response  
 1139 in the VPT, known as burn-in. The amount of light that the device has been exposed to is  
 1140 measured in terms of the total number amount of charge liberated from the cathode, measured  
 1141 from the cathode current draw, and is known as the integrated charge. By operating at such  
 1142 high photocurrents, UVa is able to probe this burn-in effect in an attempt to understand the  
 1143 long term behaviour of the VPT response to light.

1144 The University of Virginia is well suited to test these devices, since it operates a 3.8 T  
 1145 solenoid magnet, with a sufficiently large inner bore to accommodate a rig containing five (5)  
 1146 VPTs, LEDs, LED driving hardware, and amplifying equipment. The magnet itself was built  
 1147 by Oxford instruments and has an inner bore diameter of 0.4 m and an outer bore diameter of  
 1148 1.5 m. The inner bore is 0.13 m in height from the ground, and the magnet has a length of 1.5m

1149 along its z-axis, which is perpendicular to the normal of the floor.

1150 The VPTs were supplied with high voltage (800 V anode, 600 V cathode) from a CAEN  
1151 High Voltage supply. This manufacturer also provides high voltage supplies for the VPTs used  
1152 in CMS. They are preferable due to their stability, programmable user interface, and capacity  
1153 to drive multiple VPTs simultaneously. A voltage separation between anode and cathode much  
1154 larger than this is not recommended due to its potential do damage the device.

1155 The VPTs were pulsed with blue and orange LEDs at rates of 10 kHz, and 20 kHz, to capture  
1156 the same features (frequency and rate) that light from the lead tungstate crystals would produce  
1157 while collisions were occurring in the detector. The driving circuits are the same as those used in  
1158 the LED system in the end-caps at point 5 (the location of CMS at CERN), with the exception  
1159 that the current limiting resistors are larger. They are Dallas Semiconductor DS1040Z-D70  
1160 Programmable One-Shot Pulse Generators. The TTL signals from the FPGA serve as a trigger  
1161 for a Dallas Semiconductor pulse generator chip on the board that generates a 30 nSec pulse, so  
1162 there is no overlap in pulses generated by the VPT. The pulsing was also run in an on/off cycle  
1163 of 16 hrs on, 8 hrs off to be consistent with the LHC beam fill cycle.

1164 The LED pulsing and data acquisition was automated via a PXI unit manufactured by Na-  
1165 tional Instruments, which contains a FPGA card, a digital oscilloscope, and computer running  
1166 Windows XP. The FPGA card was programmed with LabVIEW software which controlled LED  
1167 pulse rate, low voltage power, and measurements of VPT signals. The data acquisition was  
1168 triggered by means of a PIN diode placed next to the VPT. This served the dual purpose of in-  
1169 dependent data triggering and also provided the means to correct fluctuations in the illumination  
1170 provided by the LEDs.

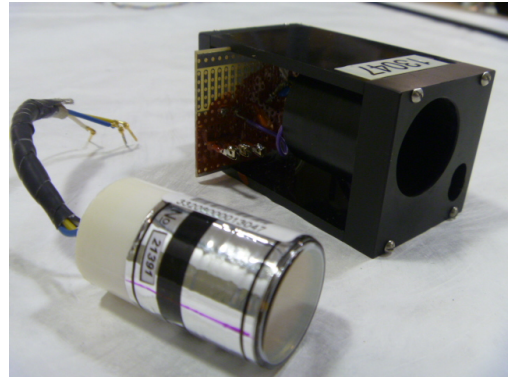
1171 The current from the VPTs anode and cathode are ultimately routed to the PXI Crates  
1172 switches, and then on to the crates DMM or oscilloscope via a preliminary amplification stage.  
1173 The VPTs anode is connected directly to a Stephenson amplifier, which connects to a high-  
1174 frequency switch. The PIN diode signal passes unmodified to that same high-frequency switch.  
1175 The cathode signal cables connect to a distribution box near the PXI Crate. The distribution  
1176 box then routes their signals to the terminal block on a low-frequency switch. All of these signals  
1177 leave the rig over BNC cables before terminating at or adjacent to the PXI Crate. Figure 4.18  
1178 highlights different components of the test stand at UVa.

### 1179 4.2.3 Results of UVa Tests

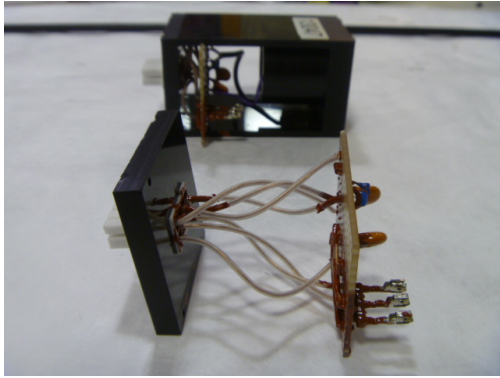
1180 The University of Virginia rig ran three sets of 5 VPTs for approximately 30 wks each in a  
1181 3.8 T magnetic field under high light conditions from blue and orange frequencies to simulate  
1182 a large light yield found in large eta regions of the end-cap. The large photocurrents allowed



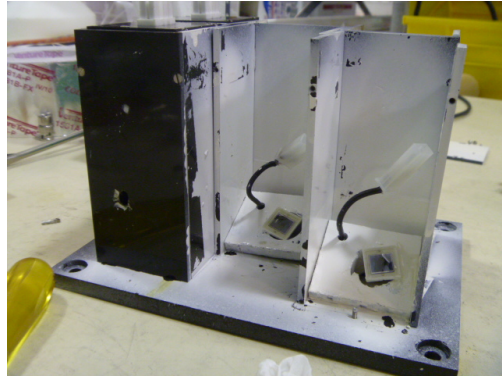
(a) The 3.8 T superconducting solenoid magnet used at UVa to study VPT performance



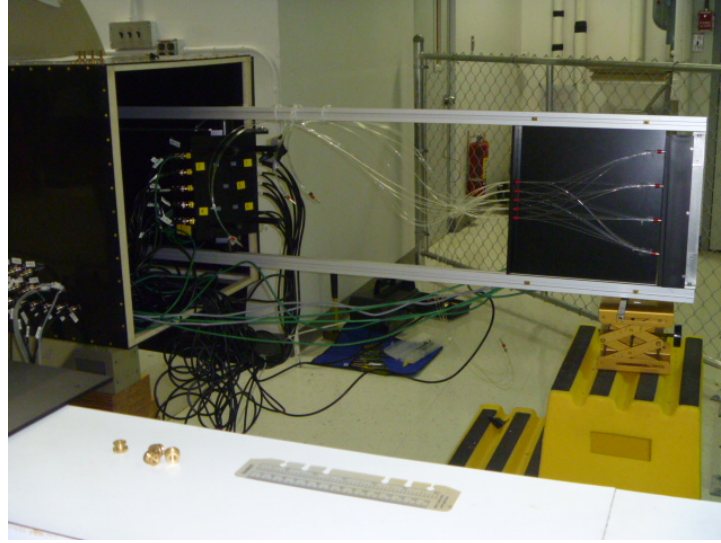
(b) A VPT before being installed in the rig and the housing that provides mechanical support and high voltage connections



(c) The housing for the VPT also provides simple HV filtering to provide stable power to the device



(d) The structure which holds 5 vpts in their housing. A PIN diode is used to measure the LED light and make corrections for fluctuations in brightness



(e) The VPT rig in maintenance position outside of the bore of magnet (during operation the rail is inserted into the bore such that the vpt housing is at the center). Fiber optics feed from the left into the VPT and amplifier housing.

Figure 4.18: Features of the UVa VPT test stand

the collection of an integrated charge of  $\sim 48$  mC for the largest gain VPT, and  $\sim 16$  mC for the other three. All VPTs were characterized by an initial steep decline followed by a plateau region, which was fit with a double exponential function of the form

$$f(x) = A + B \exp(Cx) + D \exp(Ex) \quad (4.2)$$

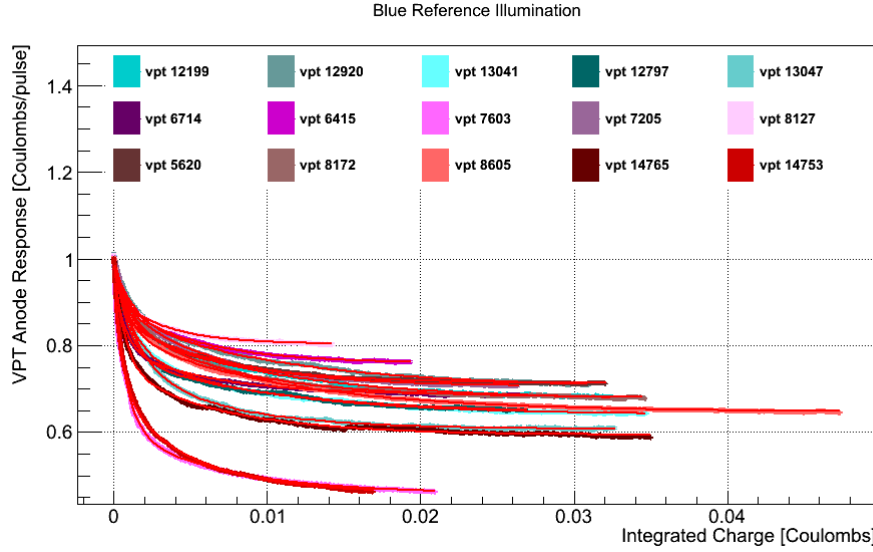


Figure 4.19: 3 runs of 5 VPTs, exposed to blue LED light, and fit to a sum of two exponentials.

Table 4.1: Fit Results for VPT Conditioning Studies at U.Va. and Brunel, Blue Reference LED

RIE Number	% Drop	$\chi^2/NDF$	Pedestal	Fast exp Amplitude	Fast exp $\tau$	Slow exp Amplitude	Slow exp $\tau$
12199	30.1	1.20e+00	1.51e-09	3.42e-10	-8.84e-04	3.85e-10	-1.00e-02
12920	27.0	7.27e-01	1.72e-09	3.16e-10	-1.16e-03	4.03e-10	-1.05e-02
13041	33.5	8.46e-01	1.09e-09	3.43e-10	-1.20e-03	2.46e-10	-9.31e-03
12797	33.6	1.07e+00	6.39e-10	2.18e-10	-9.72e-04	1.31e-10	-9.87e-03
13047	38.1	1.06e+00	5.48e-10	1.98e-10	-1.40e-03	1.49e-10	-6.19e-03
6714	29.3	8.37e-01	1.55e-09	4.10e-10	-6.66e-04	2.48e-10	-6.11e-03
6415	23.6	1.28e-01	1.19e-09	1.54e-10	-6.55e-04	2.20e-10	-5.16e-03
7603	50.3	3.25e+00	1.44e-09	1.02e-09	-8.22e-04	4.87e-10	-6.72e-03
7205	29.4	4.53e-01	1.41e-09	2.14e-10	-5.68e-04	3.94e-10	-5.96e-03
8127	19.6	1.97e-01	1.71e-09	1.82e-10	-3.12e-04	2.35e-10	-3.30e-03
5620	27.4	4.57e+00	1.68e-09	2.85e-10	-5.20e-04	3.68e-10	-6.19e-03
8172	30.3	8.75e+00	8.32e-10	1.52e-10	-1.06e-03	2.27e-10	-6.87e-03
8605	32.1	6.94e+00	1.36e-09	3.33e-10	-8.97e-04	3.94e-10	-1.03e-02
14765	38.9	2.78e+01	3.47e-10	1.37e-10	-7.46e-04	9.24e-11	-6.77e-03
14753	52.9	2.53e+01	1.19e-09	7.45e-10	-5.86e-04	6.10e-10	-4.77e-03
Average	31.0	4.62e+00	1.17e-09	2.94e-10	-1.09e-03	1.66e-10	-3.07e-01

where A is a pedestal parameter, B is the amplitude of the fastest dropping exponential, C is the time constant of the fast dropping exponential, D is the amplitude of the slow dropping exponential, and E is the time constant of the fast exponential. The summary of the fit parameters for blue LED light is shown in table 4.1 and the summary of fit parameters for the orange LED light is shown in table 4.2. Plots of the VPT anode response versus integrated charge, and

the associated fit for each of the devices is shown in figure 4.19 for blue LED exposure and in figure 4.20 for orange LED exposure. Based on these findings, it can be concluded that the VPT "burn-in" eventually reaches a plateau at about  $\sim 70\%$  for blue LED exposure and  $\sim 50\%$  for orange LED exposure.

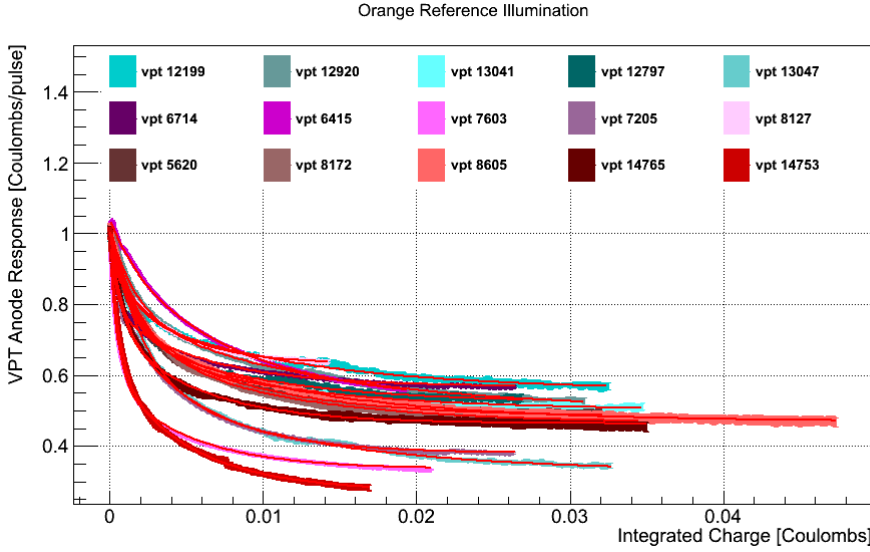


Figure 4.20: 3 runs of 5 VPTs, exposed to orange LED light, and fit to a sum of two exponentials.

Table 4.2: Fit Results for VPT Conditioning Studies at U.Va., Orange LED

RIE Number	% Drop	$\chi^2/NDF$	Pedestal	Fast exp Amplitude	Fast exp $\tau$	Slow exp Amplitude	Slow exp $\tau$
12199	41.9	6.23e-01	4.23e-10	1.79e-10	-1.10e-03	1.76e-10	-1.10e-02
12920	45.3	1.84e-01	6.73e-10	3.24e-10	-1.67e-03	3.72e-10	-1.26e-02
13041	48.3	7.42e-01	2.75e-10	1.81e-10	-1.63e-03	1.04e-10	-1.02e-02
12797	46.4	5.05e-01	2.05e-10	1.14e-10	-1.23e-03	7.87e-11	-8.77e-03
13047	63.0	1.09e+00	1.34e-10	1.73e-10	-2.18e-03	1.07e-10	-1.16e-02
6714	43.4	1.43e+01	7.73e-10	3.29e-10	-4.49e-04	2.84e-10	-6.11e-03
6415	46.5	2.34e+01	4.41e-10	8.75e-11	-1.80e-03	3.47e-10	-7.95e-03
7603	64.8	3.20e+01	3.01e-10	3.42e-10	-5.42e-04	2.24e-10	-5.04e-03
7205	63.2	6.52e+01	1.94e-10	1.29e-10	-4.49e-04	2.16e-10	-5.13e-03
8127	39.4	2.24e+01	7.09e-10	1.54e-10	-2.08e-04	3.10e-10	-3.75e-03
5620	50.3	2.30e-01	4.07e-10	2.13e-10	-1.16e-03	2.37e-10	-7.79e-03
8172	51.7	1.56e-01	4.01e-10	2.73e-10	-1.91e-03	2.08e-10	-9.48e-03
8605	49.6	1.83e-01	2.39e-10	1.46e-10	-1.45e-03	1.33e-10	-1.12e-02
14765	53.3	3.08e-01	2.07e-10	1.27e-10	-8.55e-04	1.17e-10	-5.66e-03
14753	72.2	2.22e-01	1.94e-10	2.76e-10	-6.01e-04	2.47e-10	-5.06e-03
Average	52.0	1.08e+01	3.72e-10	2.03e-10	-1.15e-03	2.11e-10	-8.10e-03

### 4.3 The Hadronic Calorimeter

The Hadronic Calorimeter (HCAL) is divided into four sub-systems: the barrel (HB), the endcap (HE), the outer calorimeter (HO), and the forward calorimeter (HF). It is especially important for measuring hadronic jets and neutrinos by measuring an imbalance in energy trans-

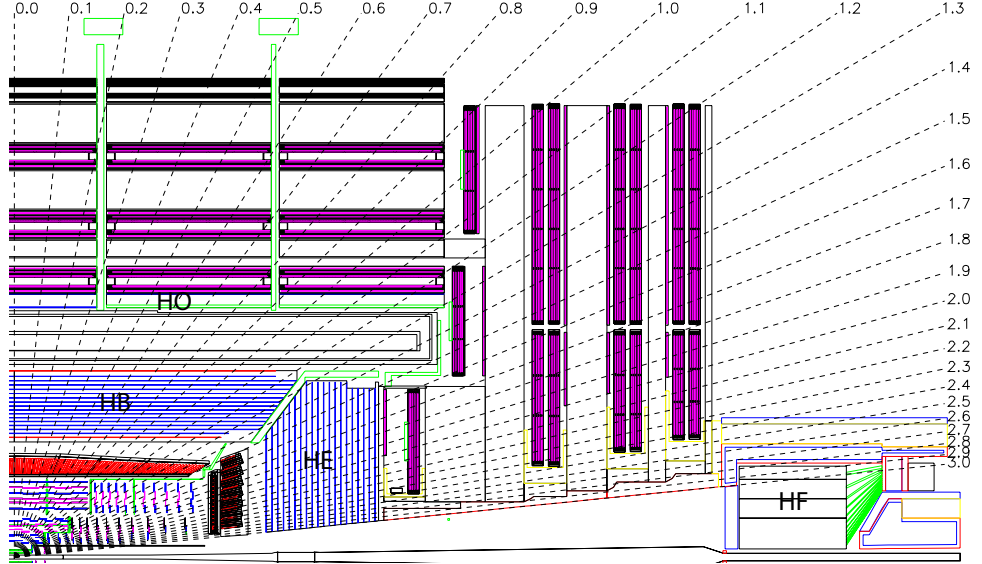


Figure 4.21: Longitudinal cross-section of the HCAL with the four sub-systems labeled

verse to the beamline. It provides coverage from  $|\eta| < 3$  from the HB, HE, and HO, and the HF extends the coverage out to  $|\eta| < 5.2$ . A diagram of the longitudinal cross section is shown in figure 4.21.

The barrel section of the HCAL, the HB, is divided into two sections longitudinally, each with 18 identical azimuthal wedges wrapped around the beamline. Each wedge has four azimuthal sections, with the center two sections aligned and each edge piece angled and staggered in a configuration that creates no projective dead material for the full radial extent of the HCAL. Figure 4.22 shows a closeup photograph of four wedges, where optical fibers are layed out accross the seam that joins the staggered edge layers to the two aligned center layers, and blue lines highlight the four azimuthal divisions for a single wedge.

The HB is a sampling calorimeter, with each azimuthal section composed of 14 alternating layers of brass absorber plates, and layers plastic scintillator tiles, with steel plates on the top and bottom layers for structural support. Each quarter-barrel section of scintillator has 16  $\eta$  divisions, giving a segmentation of  $(\Delta\eta, \Delta\phi) = (0.087, 0.087)$ . The brass absorber plates are C26000/Cartridge Brass. The material was chosen since the absorber material could not be distorted or bend under the stress of its own weight for at least 15 years of experimental running. Much of the material was purchased, but over a million Russian WW2 brass shell casings, designed to withstand the stresses of travel aboard 1940s Navy vessels, were melted down and processed into absorber tiles. Figure 4.24 shows members of the Russian Navy posing with some of the shells.

When a hadron passes through a wedge, the brass and steel plates absorb energy and ini-



Figure 4.22: Closeup of the HCAL barrel section. The center section of each of the 18 wedges are labeled, optical cables lay accross the joint of the center and staggered edge sections of each wedge. The blue lines show the apporximate azimuthal division of the wedge.

tiates the decay of the hadron into a number of lighter particles. These particles pass through the scintillator layer, which absorb energy from the interactions or collisions with the passing particles. The electrons of the scintillator become excited and relax by emitting a number of photons in the blue-violet range of the visible spectrum proportional to the amount of energy absorbed by the scintillator. These photons are abosrbed by wavelength shifting fibers (WSFs), which re-emit the light in the green part of the visible spectrum. The WSFs are spliced into four clear fiber optical cables. These fibers transport the light from each of the layers to an optical de-coding unit (ODU), which arranges the fibers into readout towers. A hydrid photodiode (HPD) converts this light into electric signals and is digitized by an ADC contained on the front-end elctronics. The HPD is a photo-cathode, which converts light to electrons via the photoelectric effect, that sits above a silicon diode that amplifies the signal of the cathode. The HPD provides a gain of 2000 to the light signals received from the scintialator trays. The on-detector electronics communicate to the HCAL trigger/readout (HTR) boards, which communicate with the trigger system to decide whether the store the event as data or discard it.

The brass absorbing material has a nuclear interaction length, or the length necesary to reduce the number of charged particles in a hadron shower by  $1/e$ , of 16.42 cm, and a radiation length of 1.49 cm. This means that te HB will be able to contain a large part of most hadron showers produced at LHC energies, but a portion will still pass through the entire radial distance. The outer barrel layer, HO is designed to measure the remnants of the hadron shower. It sits



Figure 4.23: Over 1 million Russian shells of military artillery were re-processed in the construction of the HCAL

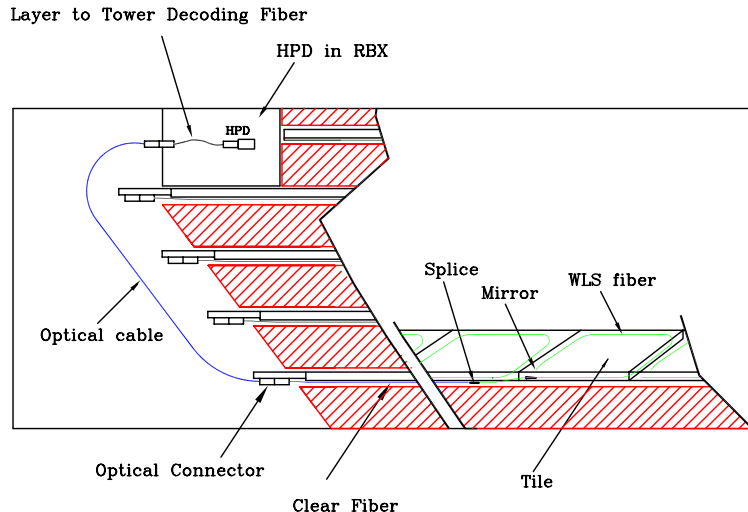


Figure 4.24: Optical readout chain of the HCAL scintilllator tiles

1239 outside of the solenoid magnet, using it as an absorber layer  $1.4/\sin \theta$  interaction lengths. It  
 1240 consists of 5 sections along the z-axis, which form rings around the beamline. Each ring is a layer  
 1241 of scintillator tiles at radial distance of 4.07m, except for the center ring. Since it corresponds  
 1242 to the  $\eta = 0$  ring, there is a minimum amount of absorber material in front of it. The central  
 1243 ring is thus two layers of scintillator at radial distances 3.82 and 4.07 m, which sit on either  
 1244 side of a 19.5cm thick piece of iron absorber.

1245 The endcap system, the HE, provide a substantial portion of the total  $\eta$  coverage, from  
 1246  $1.3 < |\eta| < 3.0$ , and contains  $\sim 1/3$  of the final state particles in a collision. Like the HB, it is  
 1247 a sampling calorimeter with alternating layers of brass and plastic. The demand for radiation  
 1248 hardness, and the need for a non-magnetic material, lead to the same choice of C26000 cartridge

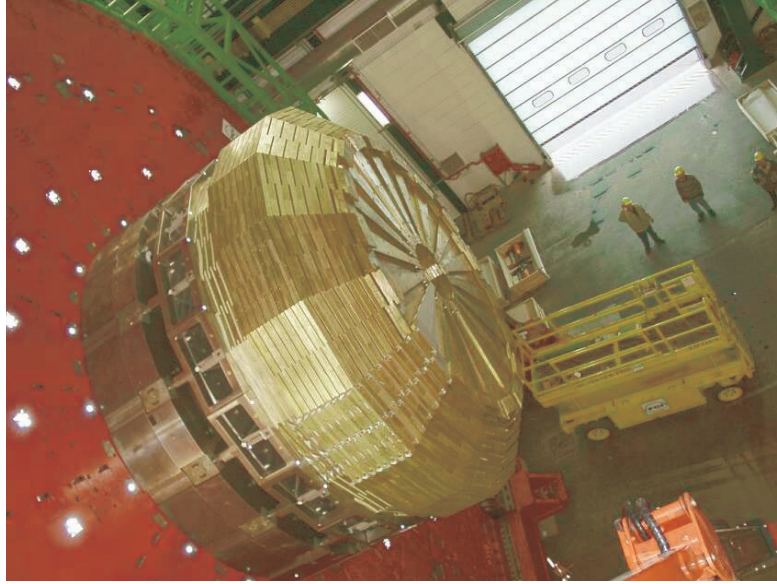


Figure 4.25: HCAL endcap, 18 azimuthal divisions of alternating layers of brass and plastic scintillator.

1249 brass found in the HB. It is also divided into 18 azimuthal wedges, and 16  $\eta$  divisions, giving  
1250 it the same  $(\Delta\eta, \Delta\phi) = (0.087, 0.087)$  segmentation. Figure 4.25 shows an image of a partially  
1251 assembled endcap before being installed.

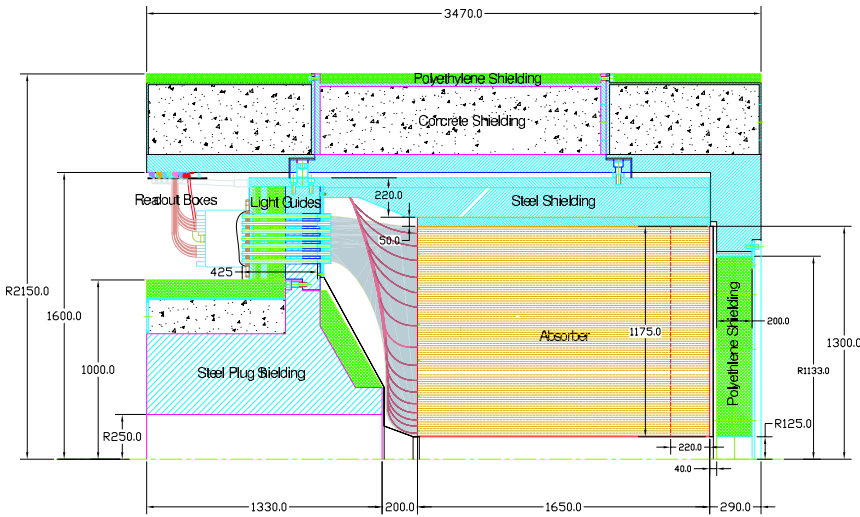


Figure 4.26: Longitudinal cross-section of the HCAL forward calorimetry, the HF

1252 The forward calorimetry, HF, extends the HCAL coverage from  $3.0 < |\eta| < 5.0$ , and neces-  
1253 sarily must sit in the region of the detector with the largest particle fluxes and thus radiation  
1254 exposure. The HF is a cylindrical steel structure with an inner bore 12.5 cm from the beam line,  
1255 and a outer radius of 130.0 cm. It sits 11.2 m away from the nominal interaction point in the

1256  $\hat{z}$  direction. Like the HE, it has 18 azimuthal divisions on either side of the interaction point.  
1257 Relativistic particles that move through the steel generate Cherenkov light, which is collected  
1258 by radiation hard quartz fibers, which transport the light to HPDs which are readout in the  
1259 manner as described above. Since the detection mechanism is Cherenkov light, this sub-system  
1260 is primarily sensitive to the electromagnetic component of the hadronic shower. Figure 4.26 shows  
1261 a cross-sectional view of the HF detector.

## 1262 4.4 Muon Chambers

1263 In  $pp$  collisions, muons are only created through electroweak or exotic physics processes, making  
1264 the detection of this particle an invaluable tool for reducing the large hadronic backgrounds  
1265 produced at the LHC. The muon chambers, positioned furthest from the beamline, sit behind  
1266 the ECAL and HCAL detectors, which absorb almost all of the hadronic activity from a collision.  
1267 They operate in a relatively low flux environment, allowing for robust measurement of their  
1268 kinematics, making it an excellent trigger system. One of the most important discovery channels  
1269 for the Higgs boson, involved the decay of the Higgs into two  $Z$  bosons, which decay to two pairs  
1270 of muons. Only 25 events were needed for a statistically significant observation in that channel,  
1271 since the backgrounds had been reduced to only 5 expected events and the muons had provided  
1272 high resolution on the invariant mass of the Higgs.

1273 The muon chambers are composed of three types of gaseous detector technology: drift tubes  
1274 (DTs), cathode strip chambers (CSCs), and resistive plate chambers (RPCs). In the muon barrel  
1275 system (MB), where the magnetic field is uniform DTs provide  $\eta$  coverage, for  $|\eta| < 1.4$ , and  
1276 are supplemented by a system of RPCs that provide an independent trigger source and faster  
1277 timing resolution. In the muon endcap system (ME), where the magnetic field would degrade  
1278 the performance of DTs, a system of CSCs and RPCs provide  $\eta$  coverage from  $1.4 < |\eta| < 2.4$ .

1279 The DTs are located in the MB system, which is divided into 5 longitudinal, cylindrical  
1280 sections around the beamline, known as wheels. In each wheel there are 4 concentric layers of  
1281 drift tube stations, one on either side of the magnet return yoke, and two interspersed inside of  
1282 it. Each wheel is divided into two 12 azimuthal sectors, making 48 stations in the barrel, as shown  
1283 in figure 4.27. Each station on the first three (fourth) layers contain 3(2) superlayers, where  
1284 each superlayer is made of a stack of 4 layers of rectangular drift cells, which are staggered  
1285 by half a cell each. Two of the superlayers are oriented such that they are parallel to the  
1286 beam, measuring the muon in the  $r - \phi$  plane. The first three layers contain a third superlayer,  
1287 orientated perpendicular to the beam, measuring a  $z$  component of the muon trajectory. Each  
1288 drift cell is a hollow  $13 \times 42$  mm tube, with a relatively thick 1.5mm wall to provide isolation

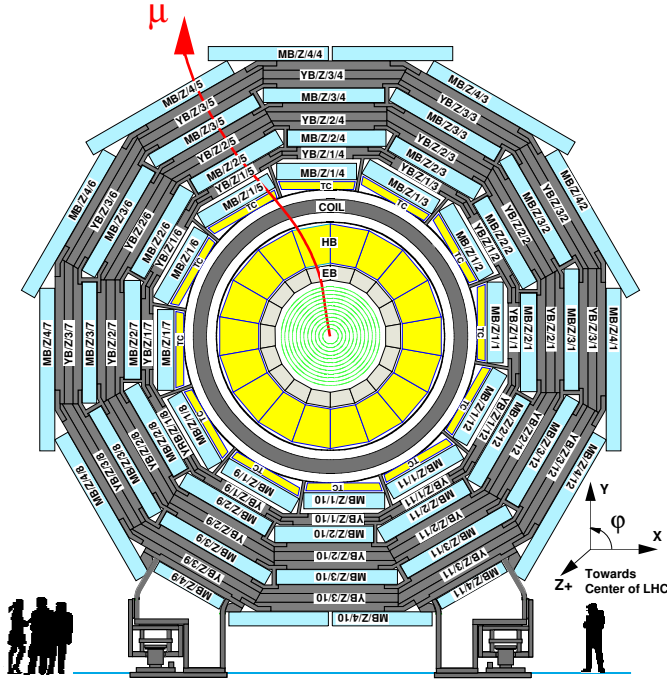


Figure 4.27: Longitudinal cross-section of one of the 5 wheels of the muon system. Drift tubes are placed in 4 concentric layers, with 2 being placed inside the return yoke of the magnet, and 12 azimuthal divisions.

1289 between adjacent cells. Each cell is filled with a mixture of 85% argon + 15% CO<sub>2</sub> gas mixture,  
 1290 and contains an anode wire that is held at 3600 V that runs down the axis of the cell. The walls  
 1291 of the cell are held at 1800 V or -1200 V depending on the wall. When a muon passes through the  
 1292 chamber, it's charge ionizes molecules of the CO<sub>2</sub> gas, causing the electrons to drift towards the  
 1293 anode wire, and the CO<sub>2</sub> ions drift towards the wall. As the electrons approach the anode, they  
 1294 are accelerated and liberate secondary elctrons from other CO<sub>2</sub> molecules, creating an avalanche  
 1295 of electrons near the wire, resulting in a drop in voltage as they are collected. The voltage drop  
 1296 is read out by front end electronics as a signal that a muon has passed through the chamber.  
 1297 The Argon gas quenches the avalanche reaction, and the maximum drift time for electrons in  
 1298 the gas is 380 ns. This long time scale necessitates the use of an addtional, fast-timing system,  
 1299 the RPCs. Figure 4.28 shows a cross-section view of a drift cell, including electric field lines  
 1300 produced by the potential difference between the anode wire and the walls of the drift cell.

1301 The reisistive place chambers (RPCs) are the fast timing system chosen to supplement the  
 1302 DTs in the barrel, and the CSCs in the endcaps. In the barrel, they are adhered to the top and  
 1303 bottom of the first two layers of drift stations. In the outer two layers, they are only adhered  
 1304 to the bottom of each station. Figure 4.29(a) shows the layout of the barrel RPC system. The  
 1305 muon endcap system is composed of three disks on either side of the intreraction point, and is  
 1306 shown in figure 4.29(b). RPCs are mounted on the back of the CSC stations of the innermost

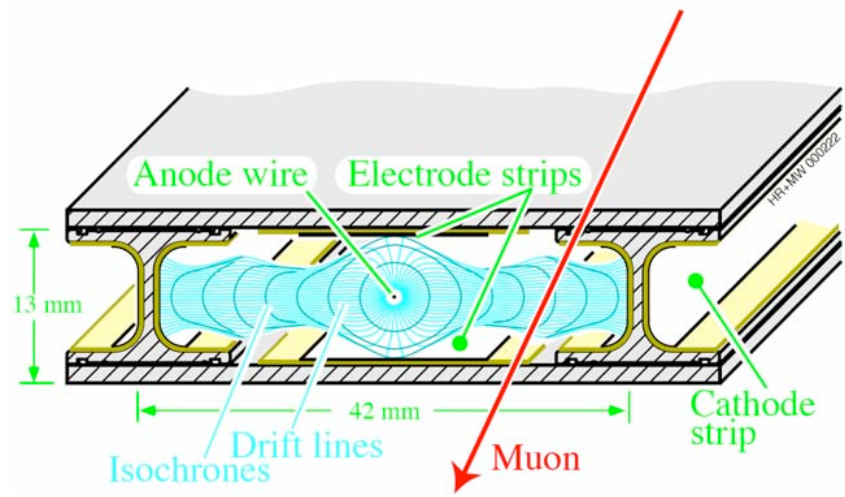
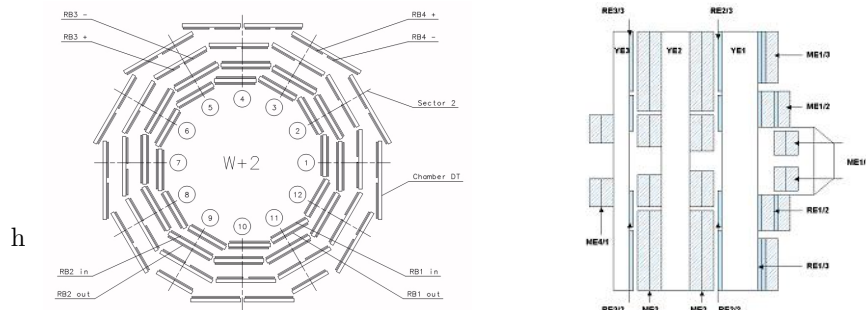


Figure 4.28: A cross-section view of a drift cell. The anode wire is held at 3600 V, creating a potential difference with the walls. Electric field lines are shown in blue.

and outermost disks, and on the front of the CSC for the middle disk. Each RPC consists of two plates of high resistance material, one held at a positive voltage, the anode, and the other held at a negative voltage, the cathode. The volume between the plates is filled with a gas similar to the drift tubes. When a muon passes between the plates, it ionizes the gas molecules, and the electrons are accelerated towards the positive plate, creating an avalanche of secondary electrons that combine with the positive plate creating a voltage drop that is read out as a signal. The timing resolution achieved from the RPCs is less than the 25 ns LHC bunch crossing, supplementing the spatial resolution provided by the DTs in the barrel, and the CSCs



(a) A longitudinal cross-section of the muon barrel RPC system. RPCs are attached to the top and bottom of the first two layers of drift stations, and to the bottom of the outer two layers

(b) Cross-section of muon endcap system. It is composed of three disks, with RPCs mounted on the back of CSCs on the first and last disks, and on the front of the CSC in the middle disk

Figure 4.29: RPC layout for the barrel and endcaps

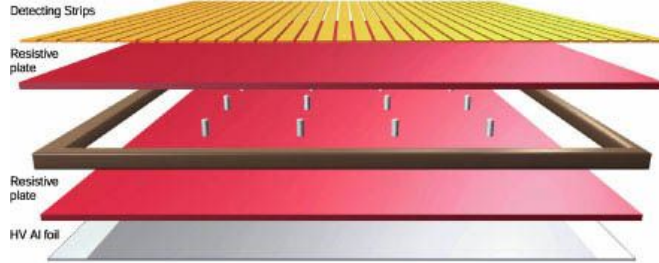


Figure 4.30: Exploded diagram of an RPC

1315 in the endcap.

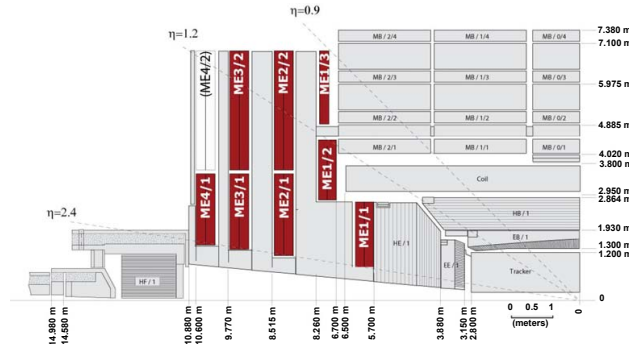


Figure 4.31: Cross-section of one quarter of the muon endcap system, with the 4 disks of CSC systems shown in red

1316 In addition to RPCs, the muon endcap (ME) system, uses cathode strip chambers (CSCs)  
1317 to provide additional spatial resolution on muons. Each endcap has 4 layers of CSCs, with a  
1318 trapezoidal shape, with 468 cathode strip chambers distributed on each. Three groups of 72  
1319 are located on the inner disk, a group of 36 and a group of 72 in the second and third disk, and  
1320 a group of 36 in the outer disk. Figure 4.32 shows the layout of a quarter section of the CSC  
1321 system in the ME. A CSC station consists of 6 layers of gas chambers, where each chamber is  
1322 an array of anode wires, held at a positive voltage, arranged perpendicular to cathode strips,  
1323 held at negative voltage. The volume of the chamber is filled with a gas that is 40% Argon,  
1324 50% CO<sub>2</sub>, and 10% CF<sub>4</sub>. When a muon passes through the volume, the gas is ionized, and now,  
1325 since the anode and cathode strips are perpendicular, when the electrons and gas ions combine  
1326 with the anode and cathode respectively, a 2-D measurement of the muon's position is recorded.  
1327 Figure 4.32 shows a diagram of a CSC chamber with 7 layers to create the 6 gas chambers.

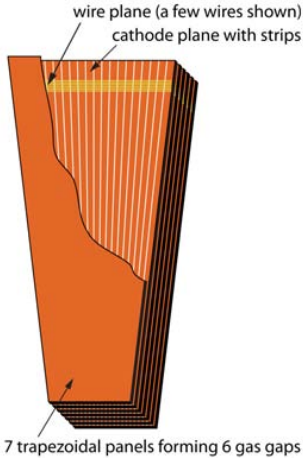


Figure 4.32: A CSC station with 7 layers, making 6 gas chambers. Cathode strips are shown in yellow, perpendicular to the vertical anode wires in orange.

## 1328 4.5 Data Collection Overview

1329 The LHC is designed to deliver protons at 40 MHz, corresponding to a bunch crossing every 25 ns.  
1330 The majority of the interactions will be glancing, low-energy collisions, which do little to reveal  
1331 new phenomenon, and would be impossible to store for analysis. A trigger system is designed to  
1332 select interesting events with a large potential of revealing new physics. The rate is reduced in  
1333 two steps through the Level-1 (L1) trigger, and the High-Level Trigger (HLT). The L1 trigger is  
1334 composed of programmable electronics and hardware that buffers the data and perform simple  
1335 calculations on tracks and calorimeter energy deposits to determine whether an event should be  
1336 kept for analysis. This reduces the event rate from 40 MHz to 10 kHz. The HLT is a computer  
1337 farm of  $\sim$ 1000 computer processors, that perform a more sophisticated reconstruction of the  
1338 tracks and energy deposits, as well as more complicated calculations between reconstructed  
1339 objects. This stage reduces the rate to a much more manageable 100 Hz.

1340 The L1 trigger is composed of local, regional, and global components. The process of deter-  
1341 mining whether to accept or reject the event begins by calculating Trigger Primitive Generators  
1342 (TPGs) based on calorimeter energy deposits, and tracks in the muon chambers. The entire  
1343 process has a latency time of  $3.2 \mu\text{s}$ , which corresponds to the length of the LHC abort gap.  
1344 Sufficiently large data buffers allow the storage of all the events processed during a bunch train,  
1345 meaning that CMS is capable of running with zero dead time due to detector readout latency.

1346 In the ECAL a trigger tower consists of a  $5 \times 5$  array of crystals. Front-end electronics on the  
1347 crystals receive ADC counts on the amplitudes of the photomultipliers, and uses information  
1348 encoded in the electronics to convert this sum to the transverse energy,  $E_T$  deposited in the  
1349 crystals. The EB TPG also encodes information about the distribution of energy, and thus the

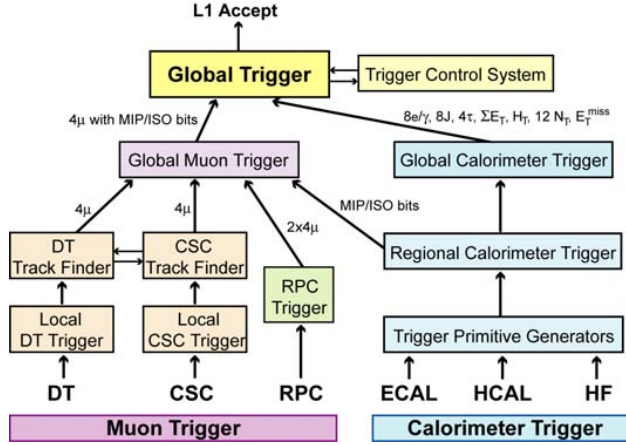
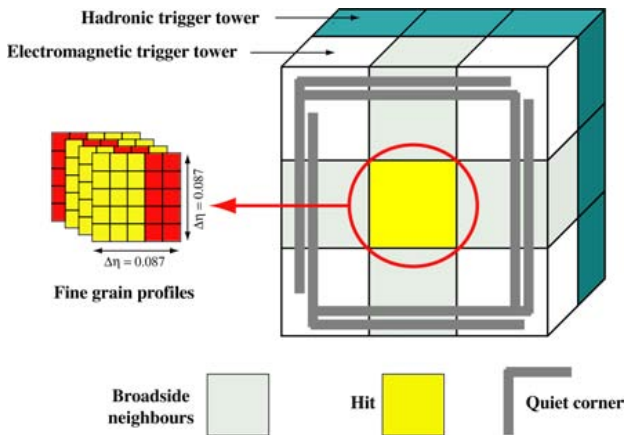


Figure 4.33: A block diagram of the L1 trigger

shower shape in the  $5 \times 5$  array, which is used to veto anomalous signals. In the HCAL, a trigger tower consists of one of the 16 azimuthal wedges, with segmentation  $(\Delta\eta, \Delta\phi) = (0.087, 0.087)$ , in the barrel and endcap. Similarly to the ECAL, front-end electronics digitize the signal from the HCAL HPDs, and convert the ADC counts into sums of transverse energy. These calorimeter TPGs are sent to a Regional Calorimeter Trigger (RCT) that is composed of a  $4 \times 4$  array of trigger towers, with the exception of the HF, which is formed by a single trigger tower.

Figure 4.34: A schematic of the  $e/\gamma$  trigger algorithm

The RCT determines electron and photon candidates from the calorimeter sums. The  $e/\gamma$  trigger searches for the highest energy trigger tower in the ECAL. Within that trigger tower, it checks that the EM shower is contained in a  $2 \times 5$  array of crystals and that the ratio of ECAL to HCAL energies is less than 5%. It is considered an isolated electron if all eight of its nearest neighbors pass these requirements, and a corner of five neighbors has energy below a threshold requirement. It is considered a non-isolated electron if only the second highest  $E_T$

1362 broadside neighbor trigger tower passes these criteria. Up to four isolated, and four non-isolated  
 1363  $e/\gamma$  candidates per RCT are passed to the Global Calorimeter Trigger (GCT).

1364 The GCT determines jets, total transverse energy, missing transverse energy, jet counts, and  
 1365  $H_T$  (scalar sum of transverse momentum), in addition to the highest rank isolated and non-  
 1366 isolated *egamma* candidates. Jets are found in a clustering algorithm that looks for large energy  
 1367 deposits in  $2 \times 12$  cells of  $\phi$  or  $\eta$  that span  $40^\circ$  and half the detector in each of coordinates. Up  
 1368 to four jets, and four tau jets from the HCAL and four jets from the HF are forwarded to the  
 1369 Global Trigger (GT).

1370 The non-calorimeter based triggers are based on measurements of the DTs, CSCs, and RPCs  
 1371 in the muon drift chambers. The barrel DTs look for hit patterns among neighboring tubes  
 1372 in successive layers, and fits a track segments in the  $\eta$  and  $\phi$  coordinates. The endcap CSCs  
 1373 provide 3-dimensional track segments and are combined with the DTs to form tracks that are  
 1374 passed to the Global Muon Trigger (GMT). The RPCs provide an independent set of tracks and  
 1375 timing hits to the GMT. Each bunch crossing the GMTs receive up to four muon candidates  
 1376 in the barrel RPCs, four from the barrel DTs, four from the endcap RPCs, and four from the  
 1377 endcap CSCs. The GMT records the candidate's  $p_T$ , charge,  $\eta$ , and  $\phi$  position, as well as a  
 1378 quality code related to the fit of the track to the hit positions of the detector. The GMT sends  
 1379 then sends these muon candidates to the GT.

1380 The Global Trigger can execute up to 128 trigger algorithms in parallel to analyze the  $p_T$ ,  
 1381 charge,  $\eta$ , and  $\phi$  position, and associated quality codes for muons, electrons, photons, jets, and  
 1382 missing transverse energy. Most algorithms compare single object characteristics to thresholds  
 1383 to determine if they pass minimally interesting criteria. If any of the algorithms return a passing  
 1384 decision, the L1 trigger issues an accept statement that allows the data stored in buffers to be  
 1385 readout by the CMS Data Acquisition (DAQ) system.

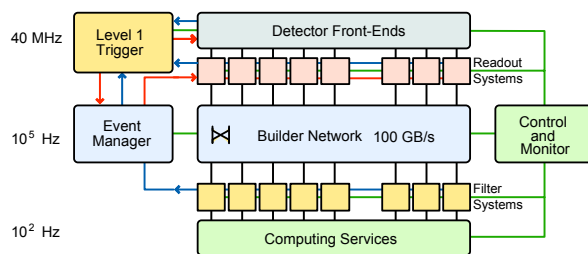


Figure 4.35: Layout of the CMS DAQ

The CMS DAQ collects information from 626 subdetector Front End Drivers (FEDs), which extract the buffered information from the various front-end systems, upon the arrival of a L1 trigger accept. An event builder algorithm assembles the fragments from the various sub-systems into a single coherent event, and transmits the information to the HLT computing farms. Figure 4.35 shows a schematic of the DAQ system.

The HLT computer farm performs the final reduction of data rate, from 100kHz from the L1 to 100Hz. The computer farm performs basic consistency checks to ensure the quality of the data, then performs calculations based on topology of the HLT path. Typically, a more sophisticated reconstruction of an object takes place, and kinematic cuts are applied to the object or in relationship to other objects in the event. Each HLT path forms its own data set, thus creating single muon, single electron, electron+jets, etc. type datasets. The unpacked detector information read by the DAQ is composed of ADC counts for each readout channel, TPGs, and the L1 decision. This is known as the RAW dataset. Reconstructed physics objects are stored RECO data tier, and finally an analysis object data (AOD) tier is created containing only information about the reconstructed objects without having to store detector information. This last format requires the least amount of data per event for storage, and contains the reconstructed physics objects, such as electrons, muons, jets, etc. which are used to search for new physics phenomena.

1404 **Chapter 5**

1405 **Particle Reconstruction at CMS**

1406 Data is reconstructed at CMS using the *ParticleFlow<sup>TM</sup>* algorithm

1407 **5.1 Muon Reconstruction**

1408 Muons rely heavily on the inner tracker and muons chambers for efficient identification and  
1409 reconstruction

1410 **5.2 Electron Reconstruction**

1411 Electrons leave charged tracks in the inner tracker, and create a wide shower of particles and  
1412 thus energy deposits in the ECAL. High energy electrons sometimes traverse the entire distance  
1413 of the ECAL and leave energy in the HCAL, however the ratio of these two energies is dispro-  
1414 portionate for the ECAL, and thus this ratio is often used to discriminate electrons from highly  
1415 electromagnetic hadronic jets.

1416 **5.3 Photon Reconstruction**

1417 Like electrons, but with no tracks, and narrower shower shape.

1418 **5.4 Jet Reconstruction**

1419 Jets are formed by matching tracks from the inner tracker to energy deposits in the ECAL  
1420 and HCAL. Energy clusters are identified from the ECAL and HCAL, and everything is then  
1421 clustered in a cone.

## 1422 5.5 Tau Reconstruction

1423 So heavy that they decay to leptons or hadrons before traversing the detector, they still leave  
1424 an oddly-numbered pronged decay hadronically due to charge conservation requiring that one of  
1425 the hadrons produced be equal charge to the tau. This results in one charged, and any number  
1426 of neutral pions, or three charged, and any number of neutral pions.

## 1427 5.6 Missing Transverse Energy Reconstruction

1428 since the detector is hermetic, and the tracker so granular, we can ensure that no particles flew  
1429 out of the detector due to lack of coverage. Only long-lived neutral particles can escape, such  
1430 as neutrinos in the standard model. Many BSM theories, such as SUSY, are characterized by  
1431 stable, neutral particles.

1432 MET is the vector sum of all of the tracks associated with a particular primary vertex (?) or  
1433 all vertices in event). Thus if there was a neutral particle that escaped detection, there would be a  
1434 momentum imbalance along the trajectory of that particle. This is how neutrinos are identified.

# <sup>1435</sup> Bibliography

- <sup>1436</sup> [1] “LHC Aerial View”.
- <sup>1437</sup> URL <http://www.coepp.org.au/files/coepp/images/cern-aerial2.jpg>.
- <sup>1438</sup> [2] CMS Collaboration, “Observation of a new boson at a mass of 125 GeV with the CMS  
<sup>1439</sup> experiment at the LHC”, *Phys.Lett.B* (2012) [arXiv:1207.7235](#).
- <sup>1440</sup> [3] ATLAS Collaboration, “Observation of a new particle in the search for the Standard  
<sup>1441</sup> Model Higgs boson with the ATLAS detector at the LHC”, *Phys.Lett.B* (2012)  
<sup>1442</sup> [arXiv:1207.7214](#).
- <sup>1443</sup> [4] M. E. Peskin and D. V. Schroeder, “An Introduction to Quantum Field Theory”.  
<sup>1444</sup> Westview Press, URL <http://www.westviewpress.com>, 1995.
- <sup>1445</sup> [5] K. G. Wilson, “Renormalization Group and Critical Phenomena. I. Renormalization  
<sup>1446</sup> Group and the Kadanoff Scaling Picture”, *Phys. Rev. B* **4** (Nov, 1971) 3174–3183,  
<sup>1447</sup> doi:[10.1103/PhysRevB.4.3174](https://doi.org/10.1103/PhysRevB.4.3174).
- <sup>1448</sup> [6] K. G. Wilson, “Renormalization Group and Critical Phenomena. II. Phase-Space Cell  
<sup>1449</sup> Analysis of Critical Behavior”, *Phys. Rev. B* **4** (Nov, 1971) 3184–3205,  
<sup>1450</sup> doi:[10.1103/PhysRevB.4.3184](https://doi.org/10.1103/PhysRevB.4.3184).
- <sup>1451</sup> [7] S. Bethke, “The 2009 World Average of alpha(s)”, *Eur.Phys.J.* **C64** (2009) 689–703,  
<sup>1452</sup> doi:[10.1140/epjc/s10052-009-1173-1](https://doi.org/10.1140/epjc/s10052-009-1173-1), [arXiv:0908.1135](#).
- <sup>1453</sup> [8] H. Weyl, “The theory of groups and quantum mechanics”. Dover Press,  
<sup>1454</sup> URL <https://ia700807.us.archive.org/20/items/ost-chemistry-quantumtheoryofa029235mbp/quantumtheoryofa029235mbp.pdf>, 1930.
- <sup>1456</sup> [9] C. N. Yang and R. L. Mills, “Conservation of Isotopic Spin and Isotopic Gauge  
<sup>1457</sup> Invariance”, *Phys. Rev.* **96** (Oct, 1954) 191–195, doi:[10.1103/PhysRev.96.191](https://doi.org/10.1103/PhysRev.96.191).
- <sup>1458</sup> [10] M. Gell-Mann, “A Schematic Model of Baryons and Mesons”, *Phys.Lett.* **8** (1964)  
<sup>1459</sup> 214–215, doi:[10.1016/S0031-9163\(64\)92001-3](https://doi.org/10.1016/S0031-9163(64)92001-3).

- <sup>1460</sup> [11] G. Zweig, “An SU<sub>3</sub> model for strong interaction symmetry and its breaking; Version 1”,  
<sup>1461</sup> Technical Report CERN-TH-401, CERN, Geneva, Jan, 1964.
- <sup>1462</sup> [12] G. Zweig, “An SU<sub>3</sub> model for strong interaction symmetry and its breaking; Version 2”,.
- <sup>1463</sup> [13] O. W. Greenberg, “Spin and Unitary-Spin Independence in a Paraquark Model of Baryons  
<sup>1464</sup> and Mesons”, *Phys. Rev. Lett.* **13** (Nov, 1964) 598–602,  
<sup>1465</sup> doi:10.1103/PhysRevLett.13.598.
- <sup>1466</sup> [14] P. Higgs, “Broken symmetries, massless particles and gauge fields”, *Physics Letters* **12**  
<sup>1467</sup> (1964), no. 2, 132 – 133, doi:[http://dx.doi.org/10.1016/0031-9163\(64\)91136-9](http://dx.doi.org/10.1016/0031-9163(64)91136-9).
- <sup>1468</sup> [15] S. Weinberg, “A Model of Leptons”, *Phys. Rev. Lett.* **19** (Nov, 1967) 1264–1266,  
<sup>1469</sup> doi:10.1103/PhysRevLett.19.1264.
- <sup>1470</sup> [16] S. L. Glashow, “Partial-symmetries of weak interactions”, *Nuclear Physics* **22** (1961),  
<sup>1471</sup> no. 4, 579 – 588, doi:[http://dx.doi.org/10.1016/0029-5582\(61\)90469-2](http://dx.doi.org/10.1016/0029-5582(61)90469-2).
- <sup>1472</sup> [17] A. Salam and J. Ward, “Electromagnetic and weak interactions”, *Physics Letters* **13**  
<sup>1473</sup> (1964), no. 2, 168 – 171, doi:[http://dx.doi.org/10.1016/0031-9163\(64\)90711-5](http://dx.doi.org/10.1016/0031-9163(64)90711-5).
- <sup>1474</sup> [18] Nobelprize.org, “The Nobel Prize in Physics 1957”.  
<sup>1475</sup> URL [http://www.nobelprize.org/nobel\\_prizes/physics/laureates/1957/](http://www.nobelprize.org/nobel_prizes/physics/laureates/1957/).
- <sup>1476</sup> [19] N. Cabibbo, “Unitary Symmetry and Leptonic Decays”, *Phys. Rev. Lett.* **10** (Jun, 1963)  
<sup>1477</sup> 531–533, doi:10.1103/PhysRevLett.10.531.
- <sup>1478</sup> [20] M. Kobayashi and T. Maskawa, “CP Violation in the Renormalizable Theory of Weak  
<sup>1479</sup> Interaction”, *Prog.Theor.Phys.* **49** (1973) 652–657, doi:10.1143/PTP.49.652.
- <sup>1480</sup> [21] G. Arnison et al., “Experimental observation of isolated large transverse energy electrons  
<sup>1481</sup> with associated missing energy at s=540 GeV”, *Physics Letters B* **122** (1983), no. 1, 103  
<sup>1482</sup> – 116, doi:[http://dx.doi.org/10.1016/0370-2693\(83\)91177-2](http://dx.doi.org/10.1016/0370-2693(83)91177-2).
- <sup>1483</sup> [22] G. Arnison et al., “Experimental observation of lepton pairs of invariant mass around 95  
<sup>1484</sup> GeV/c<sup>2</sup> at the {CERN} {SPS} collider”, *Physics Letters B* **126** (1983), no. 5, 398 – 410,  
<sup>1485</sup> doi:[http://dx.doi.org/10.1016/0370-2693\(83\)90188-0](http://dx.doi.org/10.1016/0370-2693(83)90188-0).
- <sup>1486</sup> [23] M. Banner et al., “Observation of single isolated electrons of high transverse momentum  
<sup>1487</sup> in events with missing transverse energy at the {CERN} pp collider”, *Physics Letters B*  
<sup>1488</sup> **122** (1983), no. 56, 476 – 485,  
<sup>1489</sup> doi:[http://dx.doi.org/10.1016/0370-2693\(83\)91605-2](http://dx.doi.org/10.1016/0370-2693(83)91605-2).

- 1490 [24] P. Bagnaia et al., “Evidence for Z $0e+e$  at the {CERN} pp collider”, *Physics Letters B*  
 1491 **129** (1983), no. 12, 130 – 140,  
 1492 doi:[http://dx.doi.org/10.1016/0370-2693\(83\)90744-X](http://dx.doi.org/10.1016/0370-2693(83)90744-X).
- 1493 [25] The ALEPH, DELPHI, L3, OPAL, SLD Collaborations, the LEP Electroweak Working  
 1494 Group, the SLD Electroweak and Heavy Flavour Groups, “Precision Electroweak  
 1495 Measurements on the Z Resonance”, *Phys. Rept.* **427** (2006) 257,  
 1496 arXiv:[hep-ex/0509008](https://arxiv.org/abs/hep-ex/0509008).
- 1497 [26] The ALEPH, DELPHI, L3, OPAL Collaborations, the LEP Electroweak Working Group,  
 1498 “Electroweak Measurements in Electron-Positron Collisions at W-Boson-Pair Energies at  
 1499 LEP”, *Phys. Rept.* **532** (2013) 119, arXiv:[1302.3415](https://arxiv.org/abs/1302.3415).
- 1500 [27] F. Abe et al., “Observation of Top Quark Production in  $\bar{p}p$  Collisions with the Collider  
 1501 Detector at Fermilab”, *Phys. Rev. Lett.* **74** (Apr, 1995) 2626–2631,  
 1502 doi:[10.1103/PhysRevLett.74.2626](https://doi.org/10.1103/PhysRevLett.74.2626).
- 1503 [28] S. Abachi et al., “Search for High Mass Top Quark Production in  $p\bar{p}$  Collisions at  $\sqrt{s} =$   
 1504 1.8 TeV”, *Phys. Rev. Lett.* **74** (Mar, 1995) 2422–2426,  
 1505 doi:[10.1103/PhysRevLett.74.2422](https://doi.org/10.1103/PhysRevLett.74.2422).
- 1506 [29] LHC Higgs Cross Section Working Group Collaboration, “Handbook of LHC Higgs Cross  
 1507 Sections: 3. Higgs Properties”, doi:[10.5170/CERN-2013-004](https://doi.org/10.5170/CERN-2013-004), arXiv:[1307.1347](https://arxiv.org/abs/1307.1347).
- 1508 [30] W. Beenakker et al., “Higgs radiation off top quarks at the Tevatron and the LHC”,  
 1509 *Phys.Rev.Lett.* **87** (2001) 201805, doi:[10.1103/PhysRevLett.87.201805](https://doi.org/10.1103/PhysRevLett.87.201805),  
 1510 arXiv:[hep-ph/0107081](https://arxiv.org/abs/hep-ph/0107081).
- 1511 [31] W. Beenakker et al., “NLO QCD corrections to t anti-t H production in hadron  
 1512 collisions”, *Nucl.Phys.* **B653** (2003) 151–203, doi:[10.1016/S0550-3213\(03\)00044-0](https://doi.org/10.1016/S0550-3213(03)00044-0),  
 1513 arXiv:[hep-ph/0211352](https://arxiv.org/abs/hep-ph/0211352).
- 1514 [32] R. Frederix et al., “Scalar and pseudoscalar Higgs production in association with a  
 1515 top-antitop pair”, *Phys.Lett.* **B701** (2011) 427–433,  
 1516 doi:[10.1016/j.physletb.2011.06.012](https://doi.org/10.1016/j.physletb.2011.06.012), arXiv:[1104.5613](https://arxiv.org/abs/1104.5613).
- 1517 [33] M. Garzelli, A. Kardos, C. Papadopoulos, and Z. Trocsanyi, “Standard Model Higgs boson  
 1518 production in association with a top anti-top pair at NLO with parton showering”,  
 1519 *Europhys.Lett.* **96** (2011) 11001, doi:[10.1209/0295-5075/96/11001](https://doi.org/10.1209/0295-5075/96/11001), arXiv:[1108.0387](https://arxiv.org/abs/1108.0387).

- [34] S. Dawson, L. Orr, L. Reina, and D. Wackerlo, “Associated top quark Higgs boson production at the LHC”, *Phys.Rev.* **D67** (2003) 071503,  
`doi:10.1103/PhysRevD.67.071503`, [arXiv:hep-ph/0211438](https://arxiv.org/abs/hep-ph/0211438).
- [35] T. Gleisberg et al., “Event generation with SHERPA 1.1”, *JHEP* **0902** (2009) 007,  
`doi:10.1088/1126-6708/2009/02/007`, [arXiv:0811.4622](https://arxiv.org/abs/0811.4622).
- [36] P. Artoisenet, R. Frederix, O. Mattelaer, and R. Rietkerk, “Automatic spin-entangled decays of heavy resonances in Monte Carlo simulations”, *JHEP* **1303** (2013) 015,  
`doi:10.1007/JHEP03(2013)015`, [arXiv:1212.3460](https://arxiv.org/abs/1212.3460).
- [37] F. Cascioli, P. Maierhofer, and S. Pozzorini, “Scattering Amplitudes with Open Loops”, *Phys.Rev.Lett.* **108** (2012) 111601, `doi:10.1103/PhysRevLett.108.111601`,  
[arXiv:1111.5206](https://arxiv.org/abs/1111.5206).
- [38] F. Krauss, R. Kuhn, and G. Soff, “AMEGIC++ 1.0: A Matrix element generator in C++”, *JHEP* **0202** (2002) 044, `doi:10.1088/1126-6708/2002/02/044`,  
[arXiv:hep-ph/0109036](https://arxiv.org/abs/hep-ph/0109036).
- [39] T. Gleisberg and F. Krauss, “Automating dipole subtraction for QCD NLO calculations”, *Eur.Phys.J.* **C53** (2008) 501–523, `doi:10.1140/epjc/s10052-007-0495-0`,  
[arXiv:0709.2881](https://arxiv.org/abs/0709.2881).
- [40] Planck Collaboration, “Planck 2013 results. I. Overview of products and scientific results”, *Astron.Astrophys.* **571** (2014) A1, `doi:10.1051/0004-6361/201321529`,  
[arXiv:1303.5062](https://arxiv.org/abs/1303.5062).
- [41] V. Rubin, N. Thonnard, and J. Ford, W.K., “Rotational properties of 21 SC galaxies with a large range of luminosities and radii, from NGC 4605 /R = 4kpc/ to UGC 2885 /R = 122 kpc/”, *Astrophys.J.* **238** (1980) 471, `doi:10.1086/158003`.
- [42] Super-Kamiokande Collaboration Collaboration, “Measurements of the solar neutrino flux from Super-Kamiokande’s first 300 days”, *Phys.Rev.Lett.* **81** (1998) 1158–1162,  
`doi:10.1103/PhysRevLett.81.1158`, [arXiv:hep-ex/9805021](https://arxiv.org/abs/hep-ex/9805021).
- [43] KamLAND Collaboration Collaboration, “Measurement of neutrino oscillation with KamLAND: Evidence of spectral distortion”, *Phys.Rev.Lett.* **94** (2005) 081801,  
`doi:10.1103/PhysRevLett.94.081801`, [arXiv:hep-ex/0406035](https://arxiv.org/abs/hep-ex/0406035).
- [44] MINOS Collaboration Collaboration, “Observation of muon neutrino disappearance with the MINOS detectors and the NuMI neutrino beam”, *Phys.Rev.Lett.* **97** (2006) 191801,  
`doi:10.1103/PhysRevLett.97.191801`, [arXiv:hep-ex/0607088](https://arxiv.org/abs/hep-ex/0607088).

- 1552 [45] S. P. Martin, “A Supersymmetry primer”, *Adv.Ser.Direct.High Energy Phys.* **21** (2010)  
 1553 1–153, doi:10.1142/9789814307505\_0001, arXiv:hep-ph/9709356.
- 1554 [46] J. Aguilar-Saavedra, R. Benbrik, S. Heinemeyer, and M. Prez-Victoria, “Handbook of  
 1555 vectorlike quarks: Mixing and single production”, *Phys.Rev.* **D88** (2013), no. 9, 094010,  
 1556 doi:10.1103/PhysRevD.88.094010, arXiv:1306.0572.
- 1557 [47] G. Burdman, M. Perelstein, and A. Pierce, “Large Hadron Collider tests of a little Higgs  
 1558 model”, *Phys.Rev.Lett.* **90** (2003) 241802, doi:10.1103/PhysRevLett.90.241802,  
 1559 arXiv:hep-ph/0212228.
- 1560 [48] M. Perelstein, M. E. Peskin, and A. Pierce, “Top quarks and electroweak symmetry  
 1561 breaking in little Higgs models”, *Phys.Rev.* **D69** (2004) 075002,  
 1562 doi:10.1103/PhysRevD.69.075002, arXiv:hep-ph/0310039.
- 1563 [49] H.-C. Cheng, I. Low, and L.-T. Wang, “Top partners in little Higgs theories with  $T$   
 1564 parity”, *Phys. Rev. D* **74** (Sep, 2006) 055001, doi:10.1103/PhysRevD.74.055001.
- 1565 [50] H.-C. Cheng, B. A. Dobrescu, and C. T. Hill, “Electroweak symmetry breaking and extra  
 1566 dimensions”, *Nucl.Phys.* **B589** (2000) 249–268, doi:10.1016/S0550-3213(00)00401-6,  
 1567 arXiv:hep-ph/9912343.
- 1568 [51] M. S. Carena, E. Ponton, J. Santiago, and C. E. Wagner, “Light Kaluza Klein States in  
 1569 Randall-Sundrum Models with Custodial SU(2)”, *Nucl.Phys.* **B759** (2006) 202–227,  
 1570 doi:10.1016/j.nuclphysb.2006.10.012, arXiv:hep-ph/0607106.
- 1571 [52] C. T. Hill, “Topcolor: Top quark condensation in a gauge extension of the standard  
 1572 model”, *Phys.Lett.* **B266** (1991) 419–424, doi:10.1016/0370-2693(91)91061-Y.
- 1573 [53] R. Contino, L. Da Rold, and A. Pomarol, “Light custodians in natural composite Higgs  
 1574 models”, *Phys.Rev.* **D75** (2007) 055014, doi:10.1103/PhysRevD.75.055014,  
 1575 arXiv:hep-ph/0612048.
- 1576 [54] L. Evans and P. Bryant, “LHC Machine”, *JINST* **3** (2008) S08001,  
 1577 doi:10.1088/1748-0221/3/08/S08001.
- 1578 [55] M. Benedikt et al., “LHC Design Report Vol3 - The Injection Chain”. CERN, Geneva,  
 1579 2004.
- 1580 [56] C. Hill et al., “Tests of the CERN proton linac performance for LHC - type beams”,  
 1581 *eConf* **C000821** (2000) TUD17, arXiv:physics/0008102.
- 1582 [57] K. S. Klaus Hanke, and Michel Chanel.

- 1583 [58] “Image, CERN PSbooster Layout”.  
 1584 URL <http://psb-machine.web.cern.ch/psb-machine/>.
- 1585 [59] S. Baird, “Accelerators for pedestrians; rev. version”, Technical Report AB-Note-2007-014.  
 1586 CERN-AB-Note-2007-014. PS-OP-Note-95-17-Rev-2. CERN-PS-OP-Note-95-17-Rev-2,  
 1587 CERN, Geneva, Feb, 2007.
- 1588 [60] “CERN Website, Super Proton Synchrotron”.  
 1589 URL <http://home.web.cern.ch/about/accelerators/super-proton-synchrotron>.
- 1590 [61] G. Dme, “The SPS acceleration system travelling wave drift-tube structure for the CERN  
 1591 SPS”, .
- 1592 [62] O. S. Brning et al., “LHC Design Report Vol1 - The Main Ring”. CERN, Geneva, 2004.
- 1593 [63] “CERN, List of All LHC Magnets”. URL [http://lhc-machine-outreach.web.cern.ch/lhc-machine-outreach/components/magnets/types\\_of\\_magnets.htm](http://lhc-machine-outreach.web.cern.ch/lhc-machine-outreach/components/magnets/types_of_magnets.htm).  
 1594
- 1595 [64] M. Barnes, J. Borburgh, B. Goddard, and M. Hourican, “Injection and extraction  
 1596 magnets: septa”, [arXiv:1103.1062](https://arxiv.org/abs/1103.1062).
- 1597 [65] M. Barnes et al., “Injection and extraction magnets: Kicker magnets”, [arXiv:1103.1583](https://arxiv.org/abs/1103.1583).
- 1598 [66] “Outreach, CERN LHC, Cryogenic System”. URL <http://home.web.cern.ch/about/engineering/cryogenics-low-temperatures-high-performance>.  
 1599
- 1600 [67] “The challenge of keeping cool”, .
- 1601 [68] P. Lebrun, “Large Cryogenic Helium Refrigeration System for the LHC”, Technical  
 1602 Report LHC-Project-Report-629. CERN-LHC-Project-Report-629, CERN, Geneva, Feb,  
 1603 2003. revised version number 1 submitted on 2003-02-19 11:44:11.
- 1604 [69] “Outreach, CERN LHC, Vacuum System”. URL <http://home.web.cern.ch/about/engineering/vacuum-empty-interplanetary-space>.  
 1605

# <sup>1606</sup> List of Acronyms

<sup>1607</sup> **ATLAS** A Toroidal LHC Apparatus

<sup>1608</sup> **BSM** Beyond the Standard Model

<sup>1609</sup> **CERN** European Center for Nuclear Research

<sup>1610</sup> **CMS** Compact Muon Solenoid

<sup>1611</sup> **ECAL** Electromagnetic Calorimeter

<sup>1612</sup> **FSR** Final State Radiation

<sup>1613</sup> **HCAL** Hadronic Calorimeter

<sup>1614</sup> **ISR** Initial State Radiation

<sup>1615</sup> **JHEP** Journal of High Energy Physics

<sup>1616</sup> **LHC** Large Hadron Collider

<sup>1617</sup> **LO** Leading Order

<sup>1618</sup> **MVA** Multi-Variate Analysis

<sup>1619</sup> **NLO** Next to Leading Order

<sup>1620</sup> **QCD** Quantum Chromodynamics

<sup>1621</sup> **QED** Quantum Electrodynamics

<sup>1622</sup> **QFT** Quantum Field Theory

<sup>1623</sup> **SM** Standard Model